POLITECNICO
MILANO 1863

SCUOLA DI INGEGNERIA INDUSTRIALE
E DELL'INFORMAZIONE

Admissible Region Approach to Correlate Measurements Tracks to Satellite Fragmentation Events

Tesi di Laurea Magistrale in
Space Engineering - Ingegneria Spaziale

Author: **Alessandro Mignocchi**

Student ID: 990960
Advisor: Prof. Marco Felice Montaruli
Co-advisors: Prof. Pierluigi Di Lizia
Academic Year: 2022-23

Abstract

Recent years have seen a fast increase in space traffic: the growing in-orbit population of satellites has led to an impressive increasing threat of potential collisions. Breakup events are not so uncommon: they include explosions, crashes, or anomalous events resulting in fragmentation, and represent the dominant source of objects in the Near-Earth environment. In this context, it is extremely important to detect new fragmentation or assign newfound fragments to the corresponding parent, to mitigate the collision risk and increase the safety of newly designed space missions [1]. However, algorithms designed for these operations struggle when the observations of fragments are insufficient to determine their orbit accurately.

The present paper illustrates two newly developed algorithms, TITA and OPIA, dedicated to the correlation of fragments to breakup events. Their innovative aspect lies in the use of the admissible region tool, which allows to carry out this operation without requiring any result of initial orbit determination of the fragment.

TITA, through the sampling and propagation of the admissible region, bases its correlation procedure on the proximity between samples and parent in the Cartesian and measurements spaces. OPIA, on the other hand, associates the observations of fragments with the breakup event on the statistical distance between the distribution of the admissible region samples and the parent object in the (i, Ω)-plane.

The basic performance of the two codes is verified through simulations of breakup events, whose fragments are specimens to define the associative capabilities of TITA and OPIA. Then, their robustness to errors, noises, and other disturbances is also analyzed to assess the processes efficiency and effectiveness when meeting real-world challenges.

Results demonstrate that TITA can operate in both LEO and GEO, offering satisfactory accuracy, even if not excellent. However, this algorithm shows sensitivity to various fac-

tors, with complex performance metrics to interpret. OPIA instead provides unparalleled precision, robustness, and computational efficiency in LEO, while in GEO it completely loses its functionality due to the closeness in inclination i and RAAN Ω of the objects populating this region.
For this reason, the two algorithms presented reveal to be complementary rather than competitive, and their joint use can cover with good accuracy a wide range of orbital regions.

Keywords: Space debris · Fragmentation events · Admissible region · Correlation of observations · Optical attributable

Sommario

Negli ultimi anni si è osservato un rapido aumento del traffico spaziale: la crescente popolazione di satelliti ha portato a un incremento della minaccia di potenziali collisioni. Gli eventi di breakup non sono così rari: essi includono esplosioni, collisioni, o eventi anomali con conseguente frammentazione, e rappresentano la fonte predominante di oggetti nelle vicnanze della Terra. In questo contesto, è estremamente importante rilevare nuove frammentazioni o associare nuovi frammenti all'oggetto genitore corrispondente, per mitigare il rischio di collisione e aumentare la sicurezza delle nuove missioni spaziali progettate [1]. Tuttavia, gli algoritmi sviluppati per queste operazioni faticano quando le osservazioni dei frammenti sono insufficienti per determinare con precisione la loro orbita.

Il presente articolo illustra due algoritmi di recente sviluppo, TITA e OPIA, dedicati alla correlazione di frammenti agli eventi di breakup corrispondenti. Il loro aspetto innovativo risiede nell'uso dello strumento della regione ammissibile, che permette di effettuare questa operazione senza richiedere alcun risultato di determinazione iniziale dell'orbita del frammento.

TITA, attraverso il campionamento e la propagazione della regione ammissibile, basa la sua procedura di correlazione sulla vicinanza tra campioni e genitore nello spazio cartesiano e in quello delle misure. OPIA, d'altra parte, associa le osservazioni dei frammenti con l'evento di rottura sulla distanza statistica tra la distribuzione dei campioni della regione ammissibile e l'oggetto genitore nel piano dei parametri orbitali (i, Ω).

Le prestazioni di base dei due codici sono verificate attraverso simulazioni di eventi di breakup, i cui frammenti sono campioni finalizzati a definire le capacità associative di TITA e OPIA. Di seguito, anche la loro robustezza a errori, rumori e altri disturbi viene analizzata per valutare l'efficienza e l'efficacia dei processi quando si affrontano le sfide del mondo reale.

I risultati dimostrano che TITA può operare sia in LEO che in GEO, offrendo una precisione soddisfacente, anche se non eccellente. Tuttavia, questo algoritmo mostra sensibilità a vari fattori, con metriche di prestazioni complesse da interpretare. OPIA invece fornisce incomparabile precisione, robustezza ed efficienza computazionale in LEO, mentre in GEO perde completamente la sua funzionalità a causa della vicinanza in inclinazione i e RAAN Ω degli oggetti che popolano questa regione.
Per questo motivo, i due algoritmi presentati si rivelano complementari piuttosto che concorrenti, e il loro uso congiunto può coprire con buona precisione una vasta gamma di regioni orbitali.

Parole chiave: Rifiuti spaziali · Eventi di frammentazione · Regione ammissibile · Correlazione di osservazioni · Attribuibile ottico

List of Figures

List of Tables

List of Acronyms

AO : Adaptive Optics

AR : Admissible Region

ASAT : Anti-Satellite Test

CA : Collision Avoidance

CPU : Central Processing Unit

ECI : Earth-Centered Inertial

ESA : European Space Agency

FG : Fragmentation Analysis

FoV : Field of View

FRED : FRagmentation Epoch Detector

GEO : Geostationary Earth Orbit

HEO : Highly Eccentric Earth Orbit

HVA : High Value Asset

IADC : Inter-Agency Space Debris Coordination Committee

IOD : Initial Orbit Determination

ITA : Intersection Theory Anaysis

LEO : Low Earth Orbit

MATLAB : MATrix LABoratory

MD : Mahalanobis Distance

MEO : Medium Earth Orbit

MOID : Minimum Orbit Intersection Distance

NASA : National Aeronautics and Space Administration

NEO : Near Earth Object

OC : Operational Center

OD : Orbit Determination

OPIA : Orbital Parameters Intersection Analysis

PDF : Probability Density Function

RA : Right Ascension

RAAN : Right Ascension of Ascending Node

RE : Re-Entry Analysis

RTN : Radial Transversal Normal

RSO : Resident Space Object

SGP4 : Simplified General Perturbations Model #4

SPICE : Spacecraft Planet Instrument C-Matrix Events

SSA : Space Situational Awareness

SSN : Space Surveillance Network

SST : Space Surveillance & Tracking

TDM : Tracking Data Message

TITA : Topocentric Intersection Theory Analysis

TLE : Two-Line Element

TSA : Too-Short Arc

UTC : Coordinated Universal Time

VD : Virtual Debris

VF : Virtual Fragment

List of Symbols

Variable	Description	SI unit
α	Right Ascension	rad
$\dot{\alpha}$	Right Ascension rate	rad/s
$\mathcal{A}_{opt}$	Optical attributable	rad, rad/s
$\mathcal{A}_{rad}$	Radar attributable	rad, km, km/s
$\mathbf{a}$, $\ddot{\mathbf{r}}$	Acceleration vector	km/s^2
a	Semi-major axis	km
δ	Declination	rad
$\dot{\delta}$	Declination rate	rad/s
Δv	Velocity change	km/s
D	Mahalanobis distance	-
$\mathcal{E}$	Energy per unit of mass	J/kg
ε_i	Filtering threshold values	km, rad
e	Eccentricity	-
$\mathbf{\Gamma}_x$	Covariance state matrix	km, km/s
G	Newton's gravitational constant	m^3/(kg·s)
$\mathbf{h}$	Angular momentum vector	km^2/s^2
i	Inclination	rad
$\boldsymbol{\mu}_x$	Mean state vector	km, km/s
μ_E	Earth's gravitational constant	km^3/s^2
λ	Geographical longitude	rad

Variable	Description	SI unit
M, m	Mass of the body	kg
N_{grid}	Number of elements per each side of the sampling grid	-
$\mathbf{p}$, $\mathbf{r}$	Position vector	km
$\mathbf{q}$	Observer geocentric position	km
$\dot{\mathbf{q}}$	Observer geocentric velocity	km/s
$\hat{\boldsymbol{\rho}}$	Direction of the observation	-
$\hat{\boldsymbol{\rho}}_\alpha$	Derivative of $\hat{\boldsymbol{\rho}}$ with respect to Right Ascension	-
$\hat{\boldsymbol{\rho}}_\delta$	Derivative of $\hat{\boldsymbol{\rho}}$ with respect to Declination	-
ρ	Range	km
$\dot{\rho}$	Range rate	km/s
R	Correlation index	-
R_E	Earth's radius	km
r_a	Apogee radius	km
r_p	Perigee radius	km
θ	True anomaly	rad
t	Time	s
t_{blast}	Fragmentation time or epoch	s
t_{eph}	Ephemeris time or epoch	s
t_{obs}	Observation time or epoch	s
$\mathbf{v}$, $\dot{\mathbf{r}}$	Velocity vector	km/s
Φ	Geographical latitude	rad
X	Set of orbital parameters	km, rad
χ^2	Critical value	-
$\mathbf{x}$	State vector	km, km/s
Ω	Right Ascension of the Ascending Node	rad
ω	Argument of perigee	rad

Contents

1 | Introduction

The population of Resident Space Objects (RSOs) has dramatically increased in recent years, fostering many Space Surveillance and Tracking (SST) initiatives, with several fragmentation events occurring every year. According to the European Space Agency (ESA), there are about 4,300 satellites in space with less than a third still operational. Estimates predict 29,000 objects over 10 cm in characteristic length, but this number skyrockets to about 167,000,000 when acknowledging those between ranges 10 cm and 1 mm [2, 3]. During the last three decades, the number of objects tracked around the Earth has grown by a factor of 4.5 [4], with Low Earth Obit (LEO) being the most affected region due to the increment of constellations. The number of accidental collisions observed so far in LEO is in extremely good agreement with the model prediction [4], which also provides an increment in the collision rate in LEO in the next quarter of a century, mainly due to past and current end-of-life disposal practices of spacecraft and upper stages.

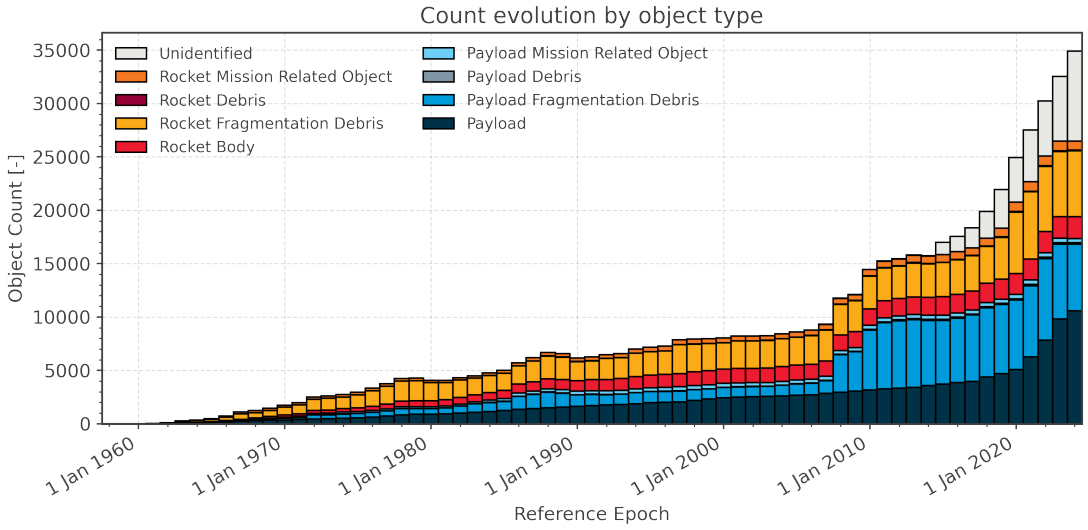

Figure 1.1: Time evolution of man-made objects in geocentric orbit. Credits [5]

This burgeoning population of satellites, while a testament to human innovation, brings with it a latent threat. However, the dangerousness of this phenomenon had already been intuited in the first years of the proliferation of space activities, with the theorizations of Kessler's Syndrome. Coined by Donald J. Kessler in 1978, this ominous scenario envisions a cascade of collisions between dismissed satellites and other space debris, culminating in a self-perpetuating chain reaction of fragmentation [6].

The risk of a perilous and potentially inaccessible LEO region started to trigger a global concern about the issue and multi-lateral meetings started under the initiative of the National Aeronautics and Space Administration (NASA), resulting in 1993 in the creation of the Inter-Agency Space Debris Coordination Committee (IADC) [7], gathering numerous space agencies from all over the world, such as ESA (Europe), NASA (USA), RSA (now Roscosmos, Russian Federation), and NASDA (now JAXA, Japan). IADC is still dedicated to the coordination of activity related to the issue of space debris, favoring the information exchange and developing guidelines and recommendations for safe and sustainable space operations.

Nowadays, the global dependence on satellite services is growing, and so is the concurrent exponential rise in space traffic, as can be appreciated in Fig. 1.1. The threat of an inhospitable Near-Earth environment is becoming crucial for future space activities and, for this reason, debris monitoring and handling are becoming fundamental fields of research well outside the borders of the orbital debris community.

The intentional and accidental collisions involving artificial satellites in recent years have captured worldwide attention, raising a growing interest in sustainable space activities, mitigation measures, and active debris removal operations.

1.1. The Near-Earth environment

In the context of space exploration and satellite operations, the Near-Earth environment refers to the region of space where artificial satellites orbit, and it is characterized by significant interest and concerning due to the high concentration of human-made objects. In this environment, objects can be categorised in two broad categories: *Identified* (trace-

able to a launch event) and *Unidentified* (untraceable, UI). In [8], the former is further categorised in:

- *Payload* (PL): space object designed to perform a specific function in space excluding launch functionality. This includes operational satellites as well as calibration objects.
- *Payload mission related objects* (PM): space objects released as space debris which served a purpose for the functioning of a payload. Common examples include covers for optical instruments or astronaut tools.
- *Payload fragmentation debris* (PF): space objects fragmented or unintentionally released from a payload as space debris for which their genesis can be traced back to a unique event. This class includes objects created when a payload explodes or when it collides with another object.
- *Payload debris* (PD): space objects fragmented or unintentionally released from a payload as space debris for which the genesis is unclear but orbital or physical properties enable a correlation with a source.
- *Rocket body* (RB): space object designed to perform launch related functionality; This includes the various orbital stages of launch vehicles, but not payloads which release smaller payloads themselves.
- *Rocket mission related objects* (RM): space objects intentionally released as space debris which served a purpose for the function of a rocket body. Common examples include shrouds and engines.
- *Rocket fragmentation debris* (RF): space objects fragmented or unintentionally released from a rocket body as space debris for which their genesis can be traced back to a unique event. This class includes objects created when a launch vehicle explodes.
- *Rocket debris* (RD): space objects fragmented or unintentionally released from a rocket body as space debris for which the genesis is unclear but orbital or physical properties enable a correlation with a source.

The taxonomy of objects in the space environment can be based on type as defined previously, but also on different characteristics and parameters of a space object, and one of the most relevant distinctions is based on cataloguing activities. An object can fall into one of three categories: catalogued, uncatalogued, or asserted, without mutual exclusion. A catalogued object has its orbital parameters tracked and recorded over extended periods by a space surveillance system, while those objects not included in a catalogue are called uncatalogued. An object is considered asserted when it hasn't been officially reported by a space surveillance system but is known to exist due to its intentional design, such as a rocket body that executes a re-entry burn after deploying a payload into orbit, before being repeatedly detected by a space surveillance system.
Another classification of paramount importance is the one founded on the orbital elements for a given epoch of catalogued or asserted objects. Orbital regimes can be identified on the base of semi-major axis a, eccentricity e, inclination i, perigee height h_p and apogee height h_a, and different categories are highlighted in Tab. 1.1.

Orbit	Description	Definition		
GEO	Geostationary Orbit	$i \epsilon [0, 25]$	$h_p \epsilon [35586, 35986]$	$h_a \epsilon [35586, 35986]$
IGO	Inclined Geosynchronous Orbit	$a \epsilon [37948, 46380]$	$e \epsilon [0.00, 0.25]$	$i \epsilon [25, 180]$
EGO	Extended Geostationary Orbit	$a \epsilon [37948, 46380]$	$e \epsilon [0.00, 0.25]$	$i \epsilon [0, 25]$
NSO	Navigation Satellites Orbit	$i \epsilon [50, 70]$	$h_p \epsilon [18100, 24300]$	$h_a \epsilon [18100, 24300]$
GTO	GEO Transfer Orbit	$i \epsilon [0, 90]$	$h_p \epsilon [0, 2000]$	$h_a \epsilon [31570, 40002]$
MEO	Medium Earth Orbit	$h_p \epsilon [2000, 31570]$	$h_a \epsilon [2000, 31570]$	
GHO	GEO-superGEO Crossing Orbits	$h_p \epsilon [31570, 40002]$	$h_a > 40002$	
LEO	Low Earth Orbit	$h_p \epsilon [0, 2000]$	$h_a \epsilon [0, 2000]$	
HAO	High Altitude Earth Orbit	$h_p > 40002$	$h_a > 40002$	
MGO	MEO-GEO Crossing Orbits	$h_p \epsilon [2000, 31570]$	$h_a \epsilon [31570, 40002]$	
HEO	Highly Eccentric Earth Orbit	$h_p \epsilon [0, 31570]$	$h_a > 40002$	
LMO	LEO-MEO Crossing Orbits	h_p $[0, 2000]$	h_p $[2000, 31570]$	
UFO	Undefined Orbit			
ESO	Escape Orbits			

Table 1.1: Ranges defining each orbital class. The units are km and degree. Credits [8]

In particular, the IADC has identified two specific regions that are considered protected due to their strategic importance and higher density of operational satellites. The first one is the LEO_{IADC} region with limitation on the altitude h between 0 and 2,000 km, while the second is the GEO_{IADC} with altitude h between 35,586 and 35,986 km and declination

δ between -15 and 15 degrees.

1.2. Kessler Syndrome

As pointed out in the introduction, Kessler Syndrome is a potential cataclysm that threatens the very foundation of ventures into space. The phenomenon was born from the mind of the space scientist Donald J. Kessler, who first conceived this dire scenario in the late 1970s and, as a distinguished NASA scientist, Kessler spent decades delving into the intricacies of space debris and its ramifications.

The essence of this event lies in the fragility of the orbital environment. As humanity's ventures beyond Earth's atmosphere proliferated, so too did man-made objects in Earth's space environment, as can be appreciated from Fig. 1.2. Satellites, space stations, and fragments of past missions now share orbits, setting fertile conditions for a possible disaster.

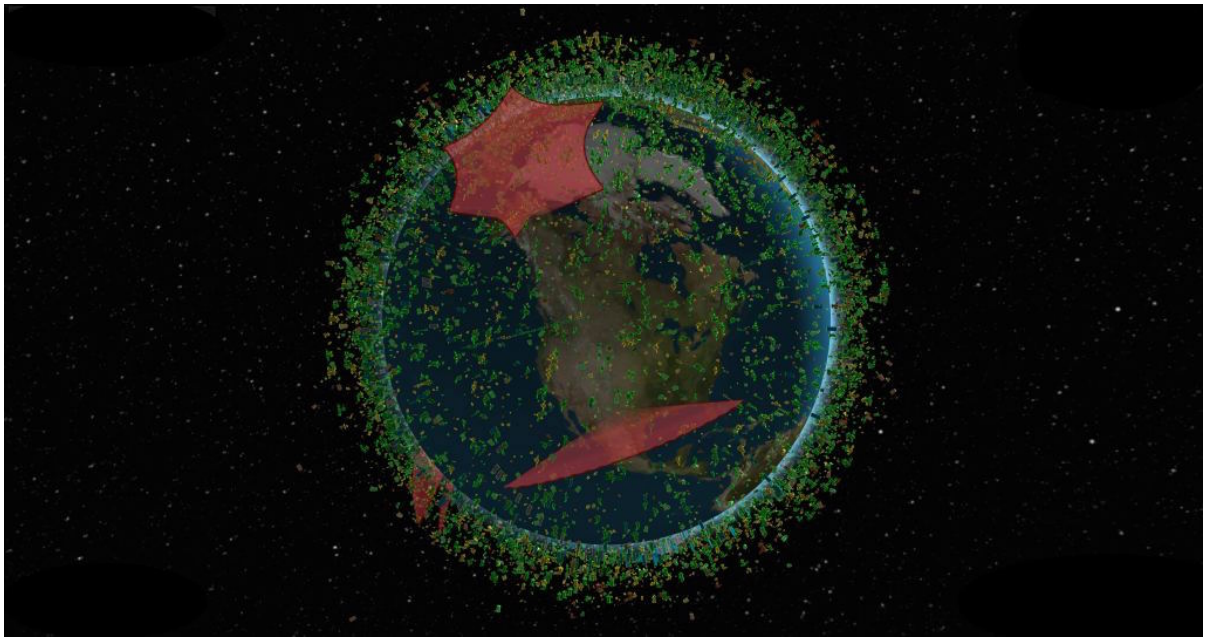

Figure 1.2: LEO objects tracked by LEOLabs. Credits [9]

This hypothetical scenario begins with an initial impact, that spawns a shower of fragments, each a potential projectile hurtling through space. These shards pose a grave threat to operational satellites and crewed missions, possibly beginning a chain reaction that shatters the delicate equilibrium of the orbital environment.

The implications of the Kessler Syndrome extend far beyond the theoretical astrophysics, considering the global absolute dependence on satellites services. For this reason, the syndrome serves as a clarion call, urging to adopt responsible practices, to engineer spacecraft with end-of-mission disposal plans, and to coordinate international efforts in space traffic management.

Donald J. Kessler's legacy resonates in the warning of his event. His contributions to space science, from his early days at NASA to his tenure as the senior scientist for orbital debris at the Johnson Space Center, have left an indelible mark on the understanding of space debris and its potential consequences.

1.3. Space Surveillance & Tracking systems

The safety and security of the economies, societies, and citizens in Europe rely on space-based applications such as communication, navigation, and observation [10]. Given the exponential growth of orbital environment complexity, monitoring and surveilling the Near-Earth environment is critical and is one of the crucial points of which Space Situational Awareness (SSA) is in charge.

The SSA initiative provides Europe and its citizens with complete and accurate information on objects orbiting Earth, on the space environment, and on threats coming from space, and many SSA programs already exist. Although the U.S. military's Space Surveillance Network (SSN) is currently the single best source of SSA in the world, also Europe has developed its own SSA initiative, in which ESA plays a pivotal role.

In particular, ESA specifically lists three segments of knowledge in SSA [11]:

- Space Surveillance and Tracking (SST): watching for active and inactive satellites, discarded launch stages and fragmentation debris that orbit the Earth.
- Space weather (SWE): monitoring the conditions of the Sun and solar wind, the Earth's magnetosphere, the ionosphere and the thermosphere, that can affect space-borne and ground-based infrastructure or endanger human life or health.
- Near-Earth objects (NEO): detecting natural objects that can potentially impact Earth and cause damage.

In particular, Space Surveillance and Tracking comprises technologies, sensors, and networks to detect and catalogue objects orbiting the Earth. At the European level, two major SST capabilities exist: the European Space Agency Space Debris Office and the European Space Surveillance and Tracking (EUSST) Consortium.
This last one is set up by the European Union first as a support framework and now as a central part of the Space Situational Awareness component of the European Union Space Programme, serving as a multilateral capability that fuses existing sensor capabilities otherwise operated separately in Europe [12]. Operations run by the SST Consortium are structured around three main functions: the sensor function, consisting of a network of ground-based sensors to survey and track space objects; a processing function, processing and analyzing SST data at national level to produce SST information and SST services; and a service function providing SST services to the EU user community, as displayed in Fig. 1.3.

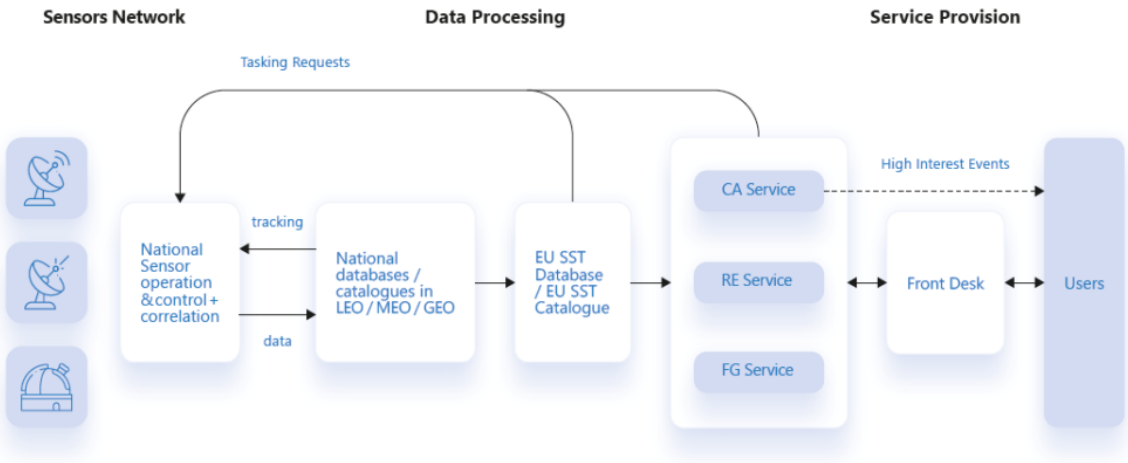

Figure 1.3: EUSST service provision model. Credits [13]

EUSST services are provided upon request to all EU Member States, EU institutions, spacecraft owners and operators, and other public and private entities, and consist of [14]:

- Collision Avoidance (CA) service: provides risk assessment of collision between spacecrafts or between spacecrafts and space debris, and generates collision avoidance alerts. Moreover, it analyses all the available information in order to detect

close approaches with different levels of risk. This service is provided by the French and Spanish Operational Centres (OCs).

- Re-entry Analysis (RE) service: provides risk assessment of uncontrolled re-entry of man-made space objects into the Earth's atmosphere and generates related information. Furthermore, it analyses all the available information regarding the uncontrolled re-entries within 30 days. The RE service is provided by the Italian OC [15].
- Fragmentation Analysis (FG) service: provides detection and characterisation of in-orbit fragmentation, breakups or collisions, and analyses all the available information (at short, medium and long term) regarding the object(s) involved in the event. Also the FG service is provided by the Italian OC.

EUSST overarching rationale is to support the safeguarding and protection of European space assets and infrastructure, attaining a higher level of independence for Europe in the area of SSA, and thus contributing to global burden-sharing with key partners [13].

1.4. Optical telescopes for LEO and GEO surveys

To provide the services illustrated in Sec. 1.3, the process chain exploits observations data derived from optical, radar, and laser sensor. In particular, optical telescopes are pivotal tools in space engineering, enabling detailed observations of celestial objects, satellites and space debris. These sensors capture and magnify light from distant objects, allowing to detect celestial bodies and aiding both astronomical research and space engineering endeavors [16].

Optical telescopes can be used to monitor objects orbiting at any altitude, as they do not need a transmitted power, but they are limited by weather and illumination conditions. They provide just angular tracks, a batch of angular observations, but not slant range and Doppler shift. This forces to carry out an association task to link measurements obtained through different acquisitions, in order to pursue high-level Orbit Determination (OD) quality.

Furthermore, telescopes, such as radar, can be subdivided into tracking and survey sen-

sors: the former observe the object by tracking it, whereas the latter detect objects while they cross the sensor Field of View (FoV).
The performance of an optical telescope is assessed using several key figures of merit. The typical ones are:

- Aperture Diameter (D): this is the diameter of the primary lens or mirror of the telescope. It determines the amount of light the telescope can collect. Larger apertures allow for better resolution and fainter objects to be observed.
- Focal Length (f): the focal length is the distance from the primary lens or mirror to the point where light converges to form an image. It affects the magnification of the telescope.
- Focal Ratio (f/D): this is the ratio of the focal length to the aperture diameter. It influences the brightness and depth of field of the image.
- Resolution: resolution refers to the ability of the telescope to distinguish between closely spaced objects. It is determined by the aperture size and the wavelength of light being observed.
- Light Gathering Power: this is directly proportional to the area of the telescope primary mirror or lens. It indicates the amount of light the telescope can collect, affecting the brightness and detail of observed objects.
- Field of View : FoV is the angular size of the portion of the sky visible through the telescope. It is crucial for observing large objects or regions of the sky.
- Image Quality and Aberrations: this includes factors like chromatic aberration, spherical aberration, and coma. A high-quality telescope minimizes these distortions for clear and sharp images.
- Sensitivity: sensitivity refers to a telescope ability to detect faint objects or low levels of light. This is crucial for observing distant or faint celestial objects.
- Tracking Accuracy: for telescopes used in astronomy, especially for astrophotography, accurate tracking is crucial to keep celestial objects in the field of view for long exposure photography.

One of the most remarkable ground-based optical telescopes in the world is the Large Binocular Telescope (LBT), located on Mount Graham, in the Pinaleno Mountains of

southeastern Arizona, United States. This a unique telescope featuring two co-mounted optical trains with 8.4 m primary mirrors. The telescope Adaptive Optics (AO) system uses two innovative key components, namely an adaptive secondary mirror with 672 actuators and a high-order pyramid wave-front sensor [17]. During the on-sky commissioning, such a system reached performances never achieved before on large ground-based optical telescopes.

The Gran Telescopio Canarias (GranTeCan or GTC) was developed by the University of Florida in collaboration with the National Autonomous University of Mexico, and the Instituto de Astrofísica de Canarias (IAC). It is a single-aperture reflecting telescope located at the Roque de los Muchachos Observatory on the island of La Palma, in the Canary Islands, Spain, characterized by a 10.4 m diameter and 169.9 m of focal length [18]. Its primary mirror consists of 36 individual hexagonal segments that together act as a single mirror. The GTC has also a secondary mirror and a tertiary mirror that together with the primary mirror produce the telescope focal plane in the focal station of choice. Thanks to its huge collecting area and advanced engineering, the GTC figures among the best-performing telescopes for astronomical research.

The Subaru Telescope is a world-class optical-infrared telescope located near the summit of Mauna Kea in Hawaii, at 4,139 m above sea level. It is operated by the National Astronomical Observatory of Japan (NAOJ) and it is characterized by an 8.3 m aperture diameter, with a 53 m^2 collecting area. Active optics for a thin primary mirror was the design backbone of the telescope to deliver a high-imaging performance. AO with a laser facility, generating an artificial guide-star, improved the telescope vision to its diffraction limit by canceling any atmospheric turbulence effect in real-time [20]. These telescopes represent some of the most important optical observatories in the world, contributing with a significant impact to a wide range of astronomical research. Their cutting-edge technologies and strategic research programs continue to be vital for the surveillance of space objects.

Figure 1.4: Gran Telescopio Canarias, at 2,267 m altitude. Credits [19]

1.5. Radar and optical IOD and correlation problem

The detection and identification of resident space objects begin with surveillance surveys, where large areas of the sky are scanned by Space Surveillance and Tracking sensors to gather large amounts of information. The efficient and automated use of these data involves data association and estimation techniques and the procedure used to match optical or radar tracks is called track-to-track correlation process. Observations can be generated by different sensors or tracking systems and the process aims at establishing a more accurate and reliable trajectory estimate of the object by merging data from multiple sources [21].

Track-to-track correlation is crucial for various engineering applications, such as satellite tracking and cataloguing, space debris monitoring, and collision avoidance maneuver. However, there are multiple ways to perform this process, depending on the quantity and nature of data available.

Some of the track-to-track association methods rely on Initial Orbit Determination (IOD)

techniques, which aims at obtaining the first guess of the orbit without a-priori information. A broad set of IOD methods are available for different types of observations, mainly optical and radar, but one of the most promising is the Double-r iteration Lambert method [22], which formulates the angles-only IOD problem as a boundary value problem. The method doesn't require initialization, accounts for measurements noise, and provides a full estimation from an arbitrary number of optical observations. Furthermore, this procedure has been shown to be more robust and less computationally intensive than classical IOD methods [22] and could be employed both with optical and radar observations.
Another interesting methodology tested on a simulated survey radar scenario with excellent results is the one that exploits a multi-target multi-sensor algorithm approach to associate data from surveillance sensors [23]. Hypotheses of track correlations are scored in the measurements space by evaluating a figure of merit based on residuals of the observations, allowing to filter out most of the false hypotheses. The suitability of the proposed track-to-track association has been assessed with a simulated scenario representative of a real operational environment, corresponding to 2 weeks of radar survey data obtained by a single survey radar. The success rate has shown to be higher than 98% and the false positives rate is lower than 0.03% [23], with the possibility of applying this methodology also to optical observation cases, or even to fragmentation detection problems.
The same authors of [23] offer a wider horizon of their work in [24], where an entire cataloguing chain, represented in Fig. 1.5, is based on track-to-track and track-to-orbit association methods. First, the input observation track is correlated against the objects in the catalogue, for which an orbit is already defined, and, in case of successful correlation, the track is used to perform orbit determination (track-to-orbit for *Catalogue Maintenance*). Otherwise, the observation goes through the multi-target multi-sensor algorithm described before. To resolve the ambiguity, particularly shorter after the event, hypotheses are generated, scored, pruned, and promoted, only when there is enough confidence, leading to the initialization of new objects in the catalogue (tracking for *Catalogue Build-up*).

Focusing on optical observations, a procedure to match two uncorrelated tracks is proposed in [25]. Compressing the track with a least-squares optimization, a 4-dimensional

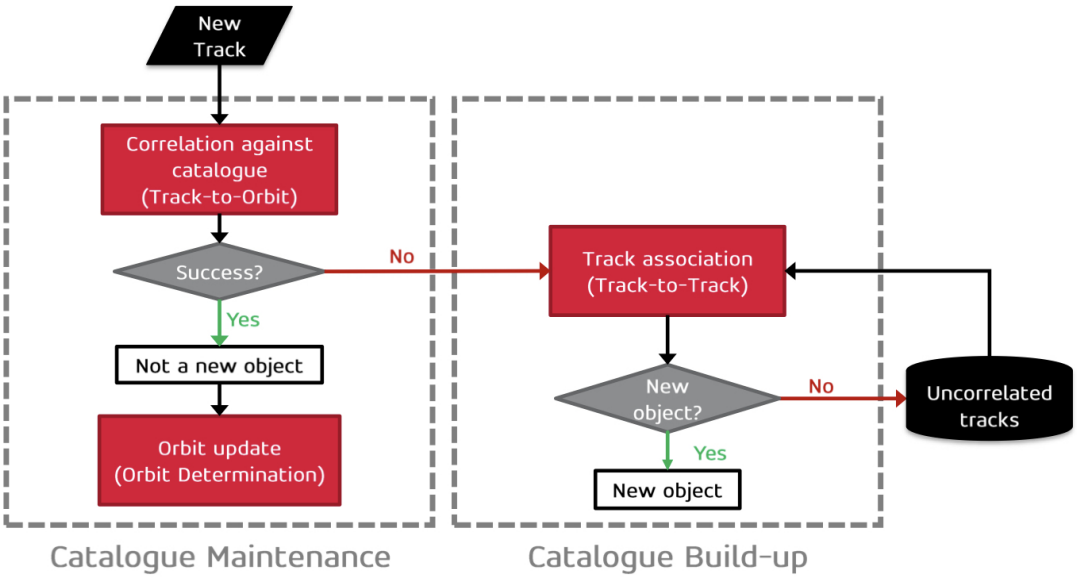

Figure 1.5: Cataloguing chain. Credits [24]

vector called optical attributable is obtained. Then, the algorithm exploits the Admissible Region (AR) tool to restrict the object state to lie within a two-dimensional submanifold of the measurements space. Such a region can be mapped into orbital elements space and propagated in time, in order to perform an intersection in the same space with the admissible region associated with another optical track. This approach simplifies the orbit correlation and determination process to geometrical intersections of hyper-surfaces and it is called Intersection Theory Analysis (ITA) [25], performing correlation without needing IOD. This simple approach has great potential also in the fragmentation correlation (track-to-fragmentation) problem, where the task is even more crucial if compared with the linkage (track-to-track) problem.

Finally, different linkage methodologies built on the AR concept are proposed and compared by Pirovano et al. [26], to find the most efficient one in determining whether two or more observations pertain to the same objects. Here, Differential Algebra (DA) is employed together with the Automatic Domain Splitting (ADS) technique to control the truncation error introduced with the truncated power series. Algorithms are tested on a hypothetical scenario with synthetic observations, to then analyze their outcomes on survey data retrieved by the ZimSMART telescope.

1.6. Fragmentation analysis problem

One of the most fundamental services provided by a SST system is the Fragmentation Analysis, which consists in the detection and characterization of in-orbit breakups. In particular, the FG service aims at identifying, track, and characterize debris generated in these events, to assess potential hazards they may pose to other active satellites. This service is of paramount importance, supporting satellite operators and space agencies in making informed decisions regarding collision avoidance maneuvers. However, to operate properly, a versatile algorithm to estimate the fragmentation epoch is required.
In fact, identifying the origin of the breakup and developing an initial understanding of the event is fundamental to provide an idea of which space object(s) were involved, what type of fragmentation it was, and the potential size of fragmentation. This information could be beneficial in different ways: model the event, provide early warnings to High Values Assets (HVAs) on possible debris intercept paths [27], and, most importantly, it can aid the rapid characterization and tracking of fragments. If the accuracy of the estimated blast point is poor then so will be the model of the fragmentation and, for this reason, different algorithms exist to deal with different typologies and quantities of information available. The most relevant ones are illustrated in the following sections.

1.6.1. Minimum orbital distance method

An approach to correlate fragments with known orbits to parent objects, using the definition of a suitable orbital similarity function, is proposed in [28]. Dimare et al. focused on the identification of both the breakup time and the parent body (or bodies) of a fragmentation detected by the Space Surveillance Network, given that the orbits of some of the fragments are known.
The idea is that the fragmentation should have happened at the time corresponding to the minimum of the mutual orbital distances of the known fragments, which is the candidate breakup time. For this reason, different metrics are selected from literature:

- D-criteria: orbital distances expresses with dependency on 5 keplerian parameters $d = d(a, e, i, \Omega, \omega)$. Three definitions are investigated: the one proposed by South-

worth and Hawinks, the one proposed by Drummond and the one proposed by Jopek [28].

- Minimum Orbit Intersection Distance (MOID): absolute minimum of the Euclidean distance between a point on the first orbit and a point on the second one.
- Nodal distance: distance between osculating orbits, provided at the same epoch, along the line of the mutual nodes.

A fragmentation event is simulated and different correlation criteria are tested with a set of candidates for the identification of the parent of 3,659 orbits. Results highlights that the distance criterion by Southworth and Hawkins and the one developed by Jopek are the most suitable one for the final purpose, allowing to find both the right breakup time and the right parent body in all the tested cases. The method can be used both for short and long-term analysis, but these criteria require a lot of observations and an initial orbit determination process of the fragment observed, which is not always possible if only one track is available for the fragment.

1.6.2. PUZZLE

Another relevant technique for fragmentation detection is implemented in the PUZZLE software package, developed by Politecnico di Milano with two objectives: first, identifying which debris, inside a set of unidentified objects, originated via a collision or explosion; second, characterizing the event in terms of mass and energy [1]. The algorithm focuses on the evolution of the osculating orbital elements of a large set of objects to identify common aspects of their motion.

In the short-term analysis, PUZZLE performs a first pruning of the Two-Line Element Sets (TLEs) under analysis, to get rid of non-coherent data. In the second step, orbital intersections are searched to select those objects that might share a common orbit. Here, a triple-loop filter proposed by Hoots et al. [29] is adopted, as illustrated in Fig. 1.6, consisting of three filters working in series: two based on orbital geometry, and one time-based. The first filter compares the height of the perigee and apogee, while the second focuses on the MOID. Then, the last filter analyzes angular windows around the position of the MOID, to check if the two objects can be in that window at the same time. Objects

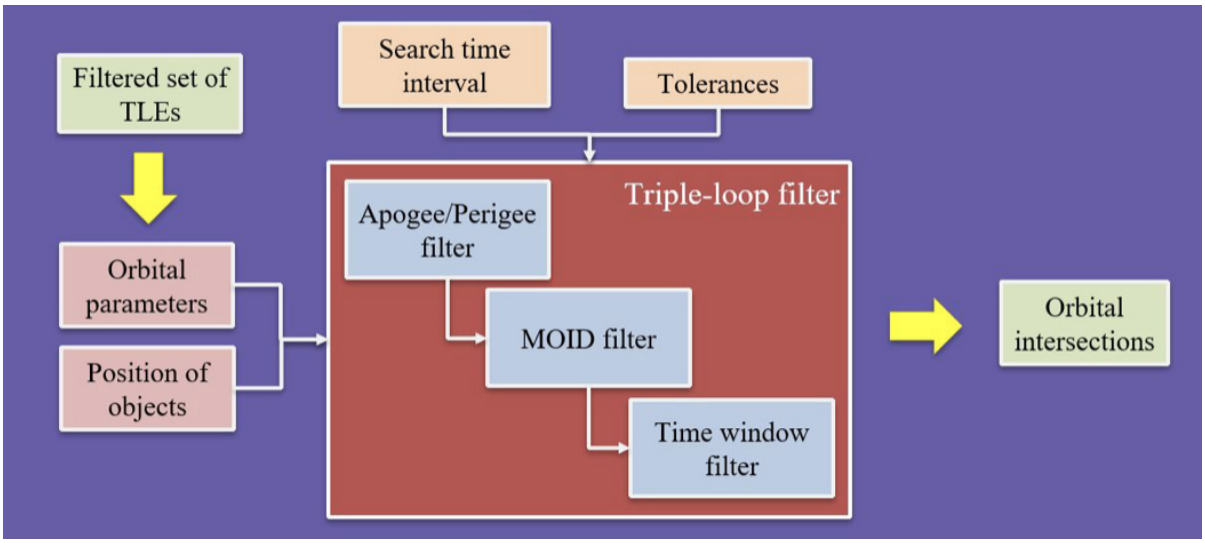

Figure 1.6: Routine module of the PUZZLE software package. Credits [1]

presenting close encounters are clustered with respect to their orbital parameters at the possible epoch of fragmentation. The objects presenting the lowest average distance are the ones selected to identify the possible parent objects.

The software toolkit has already demonstrated its potential when applied to real cases of Iridium 33 and Cosmos 2251 collision, NOAA-16 explosion, and Cosmos 1408 fragmentation, following an Anti-Satellite Missile test (ASAT) [30]. These events represent an excellent opportunity to test the software performance, showing that it can identify most of the fragments included in the catalogue with high accuracy in terms of epoch estimation. The model is also able to identify the correct parent(s) but, also in this case, the algorithm requires observations and TLEs of many fragments generated by the fragmentation event.

1.6.3. FRED

A promising method with huge potential is presented in [31], where a statistical approach is employed to identify the event epoch, even when just a single fragment orbital state is available. The algorithm is called FRagmentation Epoch Detector (FRED), and it is implemented in a software suite developed at Politecnico di Milano.

One of the most innovative aspects of this algorithm lies in the fact that it only needs a single fragment IOD result, expressed as mean state and covariance, and the parent

ephemeris to deal with the fragmentation detection problem, and this represents a crucial feature in the context of space debris and fragmentation analysis.
First of all, a Monte Carlo (MC) distribution of the fragment orbit determination result is found, generating Virtual Debris (VD). The time window under analysis is sampled and, at each instant t_i, it is computed the epoch of transit through the MOID between virtual debris and the parent object, to then evaluate the 3-dimensional relative distance at that epoch. These epochs are clustered according to a Density-Based Spatial Clustering of Applications with Noise (DBSCAN), grouping the quantities previously computed. Finally, the cluster featuring the minimum statistical distance between the MOID and the relative distance distributions is selected, and the fragmentation epoch is returned from the related distribution, in terms of mean and standard deviation.
FRED algorithm allows to have a prompt estimation of the blast point epoch, with no need to wait until several fragments detections have been made. The algorithm reliability decreases when the observed fragment orbit has either the period or the orbital plane similar to the parent object. FRED has exclusive features and characteristics that make it a valid option in operational scenario simulation, but it is worth to remark that an IOD process is required.

1.7. Thesis aim and structure

The core focus of this thesis work revolves around the development of an innovative algorithm designed to associate measurement tracks with fragmentation events, enhancing the ability to discern the intricate characteristics of each event. This includes parameters such as the size, shape, velocity, and dispersion pattern of the fragments.
The key challenge and the original aspect of the method lies in performing this task starting from a single measurement track, without performing any initial orbit determination process. To deal with these difficulties, the admissible region concept is adopted, to reconstruct the knowledge about the fragment in a deterministic way, modeling the fragment uncertainty employing the orbital constraints.
Two algorithms are developed, analyzed, and compared, involving both simulated and real data to test their performance on LEO and GEO fragmentation events.

The final objective of this research is to fill the existing gap in the track to fragmentation analysis, but, if displayed in a more comprehensive context, this algorithm can contribute to enhancing the virtuous circle established between the modeling of the fragmentation event and the monitoring of a cloud of fragments.

The thesis is structured as follows.
In Chapter 2, an overview of the necessary physical and mathematical tools is given. The theoretic set of knowledge for this work is provided: from the basic astrodynamics fundamentals to the in-depth analysis of the admissible region theory.
In Chapter 3, the developed correlation algorithms are presented. First, the Topocentric Intersection Theory Analysis (TITA) procedure is detailed, with all the main steps composing the pipeline, then the same is done for the Orbital Parameters Intersection Analysis (OPIA), immediately introducing the affinities and differences between the two codes.
Chapter 4 is dedicated to the presentation of the results. First of all, the simulated data sets used to test OPIA and TITA are illustrated, to then analyze their performance under unperturbed nominal conditions. Then, the robustness of the algorithms is tested, introducing noise and errors to emulate the real-world difficulties. The evolution of the outcomes will be reported to ensure an overall perspective of the performance of the two codes.
In Chapter 5, a conclusive summary of OPIA and TITA is offered, proposing a broad comparison of the characteristics and innovative aspects of the two codes. Finally, suggestions are presented for future development paths to undertake from the work implemented in the thesis.

2 | Fundamentals

This chapter serves as the bedrock upon which the methodology of this thesis is built. It provides a comprehensive elucidation of the essential mathematical and theoretical frameworks, with all the fundamental tools to provide a complete understanding of the thesis work.

In the first instance, the theoretical astrodynamic background is presented in Sec. 2.1, together with the main existing propagation models, fundamental for the following chapters, in order to understand the sensitivity of the algorithms to different perturbations. Then, a complete overview of the admissible region theory is illustrated in Sec. 2.2, to conclude with a brief introduction to the statistical framework in Sec. 2.3.

2.1. Astrodynamics and Propagation Models

Fundamental to astrodynamics is the understanding of orbital mechanics. This entails deciphering the complex interplay of gravitational forces, allowing to predict and control the motion of satellites, spacecraft, and other celestial objects. Concepts such as Kepler's laws, orbital elements, and perturbations are the keystones upon which astrodynamics is built. This discipline amalgamates principles from celestial mechanics, mathematics, and physics, and, for this reason, it is necessary to fix some fundamental concepts.

2.1.1. Two-Body problem and Orbital parameters

One of the simplest ways to model the relative motion of an orbiting body m_2 with respect to a main body m_1 is the Keplerian equation showed in Eq. 2.1, which is a non-linear second-order differential equation that governs the unperturbed two-body problem motion:

$$\ddot{\mathbf{r}} = -\frac{\mu}{r^3}\mathbf{r} \tag{2.1}$$

where $\mathbf{r}$ is the relative position vector originally defined in the inertial frame [32], and $\mu = Gm_1$ is the body gravitational constant, defined as $\mu_E = 398600.4418$ km^3/s^2 for the Earth, with $G = 6.6743 \cdot 10^{-11}$ m^3/(kg·s) being the Newton's constant.
The validity of the previous equation is guaranteed under the following assumptions:

- Both bodies can be described as point masses, where $m_1 \gg m_2$.
- The only force involved in the system is their mutual gravitational attraction.
- The motion is described with respect to an inertial frame.

In [32] it is shown that the path of the lower mass body m_2, usually a satellite, relative to the main body m_1 is a conic section (circle, ellipse, parabola, or hyperbola) whose shape is determined by the eccentricity. This conic is confined in a plane, defined by the angular momentum vector, that, in this case, is a constant integral of motion defined as:

$$\mathbf{h} = \mathbf{r} \times \dot{\mathbf{r}} = \text{constant} \tag{2.2}$$

The units of $\mathbf{h}$ are squared kilometers per second and this vector, at any point of the curvilinear trajectory, is orthogonal to the orbital plane, as illustrated in Fig. 2.1.
From Eq. 2.1 it is possible to derive the conservation of the total mechanical energy per unit of mass $\mathcal{E}$ of the body m_2 in the gravitational field of m_1:

$$\mathcal{E} = \frac{\dot{r}^2}{2} - \frac{\mu}{r} = \text{constant} \tag{2.3}$$

where the first term represents the specific kinetic energy, while the second is the specific potential energy.
To define the shape of the orbit two parameters are needed: the eccentricity e and the semi-major axis a. The first is retrieved from another integral of motion, represented by the Laplace vector $\mathbf{C}$, after the French mathematician Pierre-Simon Laplace (1974-1827):

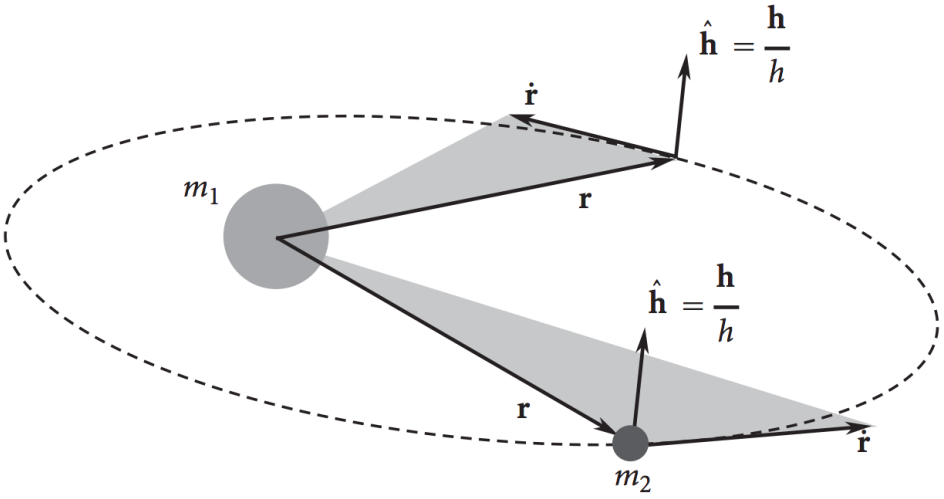

Figure 2.1: Planar path of m_2 around m_1 in the Two-Body problem. Credits [32]

$$\mathbf{C} = \dot{\mathbf{r}} \times \mathbf{h} - \mu \frac{\mathbf{r}}{r} \longrightarrow \mathbf{e} = \frac{\mathbf{C}}{\mu} \tag{2.4}$$

in which the eccentricity e is the magnitude of the vector $\mathbf{e}$, whose direction is always orthogonal to $\mathbf{h}$ and defines the apse line. The semi-major axis, instead, can be retrieved directly from one of the specific energy $\mathcal{E}$ formulations as:

$$\mathcal{E} = -\frac{\mu}{2a} \longrightarrow a = -\frac{\mu}{2\mathcal{E}} \tag{2.5}$$

However, in order to describe an orbit, four more scalar parameters are needed, because Eq. 2.1 is characterized by six constant of integration [33]. These parameters are angles, which define only the angular orientation of the orbit in the inertial space, as illustrated in Fig. 2.2.

Given the geocentric equatorial inertial reference system $[\hat{\mathbf{I}}, \hat{\mathbf{J}}, \hat{\mathbf{K}}]$, one last element is necessary to retrieve these angles: the node line $\mathbf{N}$, defined as the intersection between the orbital plane and the equatorial one:

$$\mathbf{N} = \hat{\mathbf{K}} \times \mathbf{h} \tag{2.6}$$

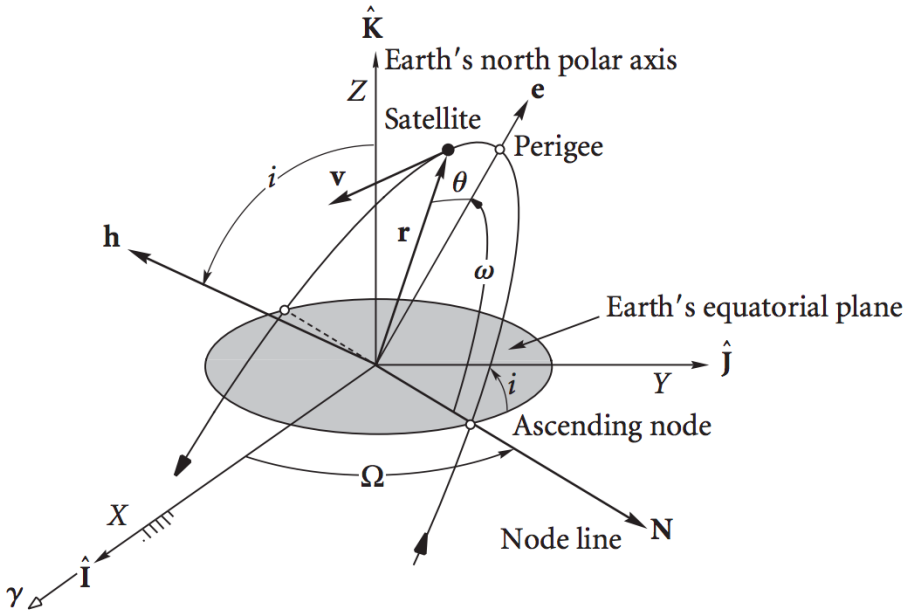

Figure 2.2: Geocentric equatorial inertial reference frame and the orbital elements. Credits [32]

Starting from the inclination i, this parameter is described as the dihedral angle between the orbital plane and the equatorial plane, measured counterclockwise around the node line vector from the equator to the orbit, such as it is always constrained between 0° and 180°.

The right ascension of the ascending node Ω (or RAAN) is defined as the angle between the positive $\hat{\mathbf{I}}$-axis and the intersection of the orbital path with the celestial equator, and is a positive number lying between 0° and 360°.

It remains to locate the perigee of the orbit and this is done through the angle between the node line vector $\mathbf{N}$ and the eccentricity vector (the apse line), called argument of perigee ω, which is always between 0° and 360°.

Finally, it is possible to define the true anomaly θ as the angle between the eccentricity vector and the position of the satellite on the orbit, measured on the orbital plane counterclockwise with respect to the direction of $\mathbf{h}$.

In this way, the full set of six orbital parameters is found, defining the orbit shape and orientation, and the position of the satellite along it.

2.1.2. Orbital perturbations and Propagation models

Keplerian orbits represent the closed-form solutions of the two-body equation of the relative motion illustrated in Sec. 2.1.1. The formulation is valid only if we consider the assumption that there are only two objects in space and that their spherically symmetric gravitational fields are the only sources of interaction between m_1 and m_2.
However, in actual motion, several elements are involved and any effect that causes the motion to deviate from the Keplerian trajectory is known as perturbation.
Common perturbations of the two-body motion include a non-spherical central body, atmospheric drag, propulsive thrust, solar radiation pressure, and gravitational interactions with celestial objects like the Moon and the Sun [32].
To model these perturbations in the two-body motion equation, it is possible to modify Eq. 2.1 as follows:

$$\ddot{\mathbf{r}} = -\frac{\mu}{r^3}\,\mathbf{r} + \mathbf{a_p} \tag{2.7}$$

where the term $\mathbf{a_p}$ includes all the perturbative acceleration contributions in addition to the spherically symmetric gravitational attraction between the two bodies. The magnitude of $\mathbf{a_p}$ is usually small compared to the primary gravitational acceleration, but the impact of some components can change with respect to the altitude, as illustrated in Fig. 2.3. The principal contributions are introduced below.

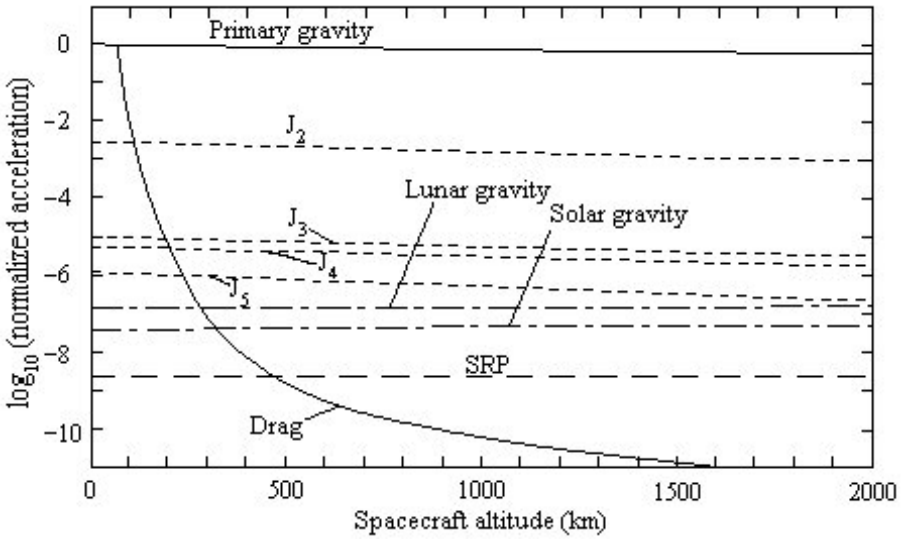

Figure 2.3: Orbital perturbations as a function of altitude. Credits [34]

- **Aerodynamic drag ($\mathbf{a_D}$)**: it is the acceleration contribution derived from the presence of the Earth's atmosphere, able to exert drag and cause aerodynamic heating on objects moving at orbital speeds. The drag effect is strictly related to the air density ρ, which becomes negligible above 1000 km, and causes orbital decaying, meaning that eccentricity e and semi-major axis a decrease, requiring frequent reboosts.

  Given the satellite drag coefficient C_d, its aerodynamic area to mass ratio, and its velocity $\mathbf{v}$, this contribution can be expressed as:

$$\mathbf{a_D} = -\frac{1}{2}\,\rho\,||\mathbf{v}||^2\,C_d\,\frac{A}{M}\,\frac{\mathbf{v}}{||\mathbf{v}||} \tag{2.8}$$

- **Gravitational anomalies ($\mathbf{a_{GH}}$)**: because of the equatorial bulges caused by centrifugal effects, the gravitational field is not symmetrically spherical but varies with the latitude as well as radius. Different J_k zonal harmonics exist, but in LEO the most effective perturbation derives from J_2. This contribution traduces in secular effects on Ω, with a rotation of the orbital plan called Nodal Regression, and on ω, with a motion known as Precession.

  Finally, it is also possible to account for Earth's triaxiality perturbation, with secular effects on GEO satellites inclination and longitude, and ocean tide effects.

- **Third-body perturbation ($\mathbf{a_{3rd}}$)**: it is the gravitational influence exerted by celestial bodies besides the main attractor (mainly Sun and Moon, considering the satellite orbiting around the Earth). This contribution can impact the satellite orbital elements, such as inclination, eccentricity, and argument of perigee. The influence is more important for high-altitude satellites, with significant effects in HEO and GEO.

  Defining the third-body gravitational constant μ_{3rd} and its inertial relative position with respect to the main attractor $\mathbf{r_{3rd}}$, this acceleration can be modeled as:

$$\mathbf{a_{3rd}} = \mu_{3rd}\left(\frac{\mathbf{r_{3rd}} - \mathbf{r}}{||\mathbf{r_{3rd}} - \mathbf{r}||^3} - \frac{\mathbf{r_{3rd}}}{||\mathbf{r_{3rd}}||^3}\right) \tag{2.9}$$

- **Solar Radiation Pressure ($\mathbf{a_{SRP}}$)**: it arises from the pressure exerted by the Sun's electromagnetic radiation on the satellite surface. The photons in sunlight carry momentum, of which a small part is transferred to the satellite, creating an acceleration opposite to the direction of the sunlight. This effect can cause an increase in the semi-major axis and eccentricity, especially for GEO satellites, while for LEO ones the influence is rather small.

  Given the solar energy reaching the satellite P_S, the speed of light c, the Sun inertial position with respect to the main attractor $\mathbf{r_S}$, the shadow function ν, and the satellite radiation coefficient C_r and radiative area A_r, this contribution can be expressed as:

$$\mathbf{a_{SRP}} = \frac{P_S}{c} C_r \frac{A_r}{M} \nu \frac{\mathbf{r} - \mathbf{r_S}}{||\mathbf{r} - \mathbf{r_S}||} \tag{2.10}$$

The effects of perturbations are not limited to impacting orbital parameters, but they also affect the integral of motions illustrated in Sec. 2.1.1. Energy, angular momentum vector, and Laplace vector are no longer conserved, changing along with the orbital parameters. Even if the simple Eq. 2.1 admits an analytical solution, the perturbed Eq. 2.7 cannot be integrated analytically without approximations. In order to retrieve the satellite position $\mathbf{p}$ and velocity $\mathbf{v}$ in a perturbed environment, it is necessary to perform numerical integration. Several numerical schemes exist, but only some of them can handle this type of problem, such as 5^{th}-4^{th} and 8^{th}-7^{th} order Dormand-Prince, 8^{th} order Gauss-Jackson, 12^{th}-10^{th} order Runga-Kutta-Nystrom, Variable-step Gauss Legendre Propagator and the Adaptive-Picard-Chebyshev methods [35]. Numerical methods are versatile and can handle a wide range of perturbations, but they can be computationally expensive, especially for long-term predictions.

However, different simplifications can be introduced to perform an analytical integration of Eq. 2.7, considering only some of the perturbing contributions. One example is the Simplified General Perturbations model #4 (SGP4) propagator [36], developed by North American Aerospace Defense Command (NORAD), designated to efficiently propagate the orbits of objects over short and medium timeframes. It accounts for periodic and long-term effects of gravitational perturbation from the Sun and Moon, Earth's oblateness, and atmospheric drag. SGP4 is particularly well-suited for applications like satellite

tracking, Space Situational Awareness, and mission planning and was used throughout this thesis work to perform orbital propagation.
Moreover, another class of propagators exists, which is the semi-analytical propagator, such as the Draper Semi-analytical Satellite Theory (DSST) [7, 37]. This method merges analytical integration along with numerical techniques, handling a broader range of perturbations compared to SGP4. DSST offers a balance between accuracy and computational efficiency, which makes it suitable for more accuracy-demanding applications.

2.2. Admissible Region

The admissible region is a mathematical formulation that replaces the conventional definition of confidence region as defined in the classical orbit determination problem. Before moving on to the detailed description of this concept, it is propaedeutic to introduce the theme of observations and attributable.

2.2.1. Observations and attributable

In Low Earth Orbits radars are primarily used for observations [38], whereas Medium Earth Orbits (MEOs) and Geostationary Earth Orbits (GEOs) are typically observed using optical sensors. In both cases, groups of observations linked to a specific object provide a data set that can be represented as an attributable, essentially a 4-dimensional vector in the measurements space. To compute a complete orbit, which requires six parameters, information on two additional quantities is needed [39].
Considering a topocentric spherical system centered in the observer it is possible to define $(\rho, \alpha, \delta) \in \mathbb{R}^+ \times [0, 2\pi) \times (-\pi/2, \pi/2)$ as the topocentric spherical coordinates of an Earth satellite, where the angular coordinates (α, δ) can be expressed with respect to an arbitrarily topocentric reference system. Throughout this thesis work, α will represent the right ascension and δ the declination, defined with respect to the J2000 reference, centered in the observer. The value of the range is indicated with ρ, expressing the linear distance between the observer and the orbiting satellite.
When an optical survey is carried out, it is common to retrieve an angular track, which

consists of a batch of angular observations, as illustrated in Fig. 2.4. This information is usually preliminary processed through a procedure called track compression, in-depth illustrated in Sec. 2.2.2.

Figure 2.4: Astro-H optical track observation image. Credits [40]

In this way, it is possible to define the *optical attributable* vector as in Eq. 2.11:

$$\mathcal{A}_{opt} = (\alpha, \delta, \dot{\alpha}, \dot{\delta}) \in [0, 2\pi) \times (-\pi/2, \pi/2) \times \mathbb{R}^2 \tag{2.11}$$

It is extremely valuable to remark that, in this thesis project, only data derived exclusively from optical sensors are analyzed and used. However, this does not imply that the algorithms developed are not suitable for the radar case, and future developments may enlarge their scientific horizons.

The detection of satellites or, more generally, of resident space objects can be performed employing radar sensors, usually organized in array configurations [38]. Their observations are limited by the power necessary for the signal to reach the objective and then return to the radar system, so measurements are limited to LEO objects.

During a tracking radar observation, the measured quantities include the range ρ, the range-rate $\dot{\rho}$ (strictly connected to the Doppler shift), and the receiver antenna (RX) pointing direction, which corresponds to the apparent position of the object on the celestial sphere, defined through two angular coordinates (α, δ). In survey observation, (α, δ) can be any point of the receiver FoV.

The *radar attributable* can be described as in Eq. 2.12:

$$\mathcal{A}_{rad} = (\alpha, \delta, \rho, \dot{\rho}) \in [-\pi, \pi) \times (-\pi/2, \pi/2) \times \mathbb{R}^+ \times \mathbb{R} \tag{2.12}$$

Joining the elements of the two attributable, it is possible to define the 6-dimensional set of measurements $\mathcal{A} = (\alpha, \delta, \dot{\alpha}, \dot{\delta}, \rho, \dot{\rho})$ in the measurements space, necessary to compute a full orbit.

For the following developments, it is also important to characterize the Cartesian position $\mathbf{r}$ and velocity $\dot{\mathbf{r}}$ of the observed object in a geocentric reference system, starting from the knowledge of the observer geocentric position $\mathbf{q}$ and the direction of observation $\hat{\boldsymbol{\rho}} = (\cos\alpha\cos\delta, \sin\alpha\cos\delta, \sin\delta)$ at the same time t:

$$\begin{gathered} \mathbf{r} = \mathbf{q} + \rho\,\hat{\boldsymbol{\rho}}, \quad \dot{\mathbf{r}} = \dot{\mathbf{q}} + \dot{\rho}\,\hat{\boldsymbol{\rho}} + \rho\,\frac{d\hat{\boldsymbol{\rho}}}{dt}, \quad \frac{d\hat{\boldsymbol{\rho}}}{dt} = \dot{\alpha}\,\hat{\boldsymbol{\rho}}_\alpha + \dot{\delta}\,\hat{\boldsymbol{\rho}}_\delta, \\ \hat{\boldsymbol{\rho}}_\alpha = (-\sin\alpha\cos\delta, \cos\alpha\cos\delta, 0), \quad \hat{\boldsymbol{\rho}}_\delta = (-\cos\alpha\sin\delta, -\sin\alpha\sin\delta, \cos\delta) \end{gathered} \tag{2.13}$$

Some of the quantities previously defined are depicted in Fig. 2.5. An important remark is that the measurements space can be only defined as a function of an observer, whose position $\mathbf{q}$ and velocity $\dot{\mathbf{q}}$ are required for the conversion from and to the Cartesian space.

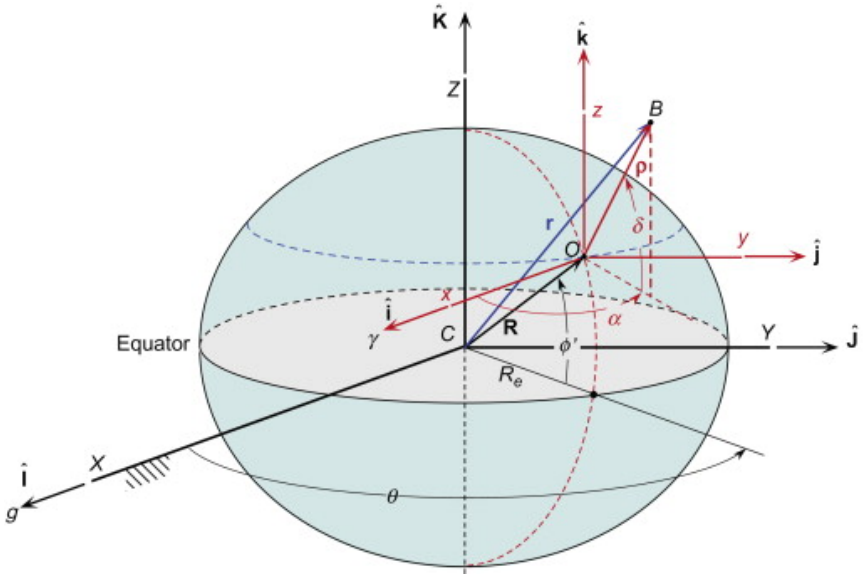

Figure 2.5: Geocentric and topocentric equatorial reference frames. Credits [32]

2.2.2. Observations compression

As introduced in Sec. 2.2.1, optical observations result in angular tracks, which consist of batches of angular observations that need to be processed to define the angular rates and complete the optical attributable $\mathcal{A}_{opt}$. This strategy is known as track compression, which is a basic pre-processing technique that consists in transforming a set of observations collected by a sensor (i.e., track) into a single one, at the middle epoch of the observation [23, 41, 42]. The benefits of this process are three:

1. Mitigation of measurement noise effect.
2. Reduction of the number of measurements.
3. Estimation of measurement rates ($\dot{\alpha}$ and $\dot{\delta}$).

This compression can be achieved by a least-squares low degree fit of the observation track, while the rate of change of a measurement is obtained by deriving the regression polynomial.

In this thesis, track compression is performed when the code is tested with real Tracking Data Messages (TDMs), containing couples of angles and their relative measurement epochs.

When a TDM arrives, angular information is extracted, and regression polynomials are generated up to the tenth order, to avoid badly conditioned behaviors. Then, the most suitable polynomial is found through a test on the R-squared (R^2) value, which is a statistical measure that indicates how much of the variation of a dependent variable is explained by an independent variable in a regression model. Multiple R^2 variants exist, but the one implemented in this thesis is illustrated in Eq. 2.14, where y_i represents the n observation measures, while f_i is the i-th polynomial evaluation at the same epoch.

$$\bar{y} = \frac{1}{n}\sum_i y_i \longrightarrow R^2 = 1 - \frac{\sum_i (y_i - f_i)^2}{\sum_i (y_i - \bar{y})^2} \tag{2.14}$$

Finally, the polynomial characterized by the minimum R^2 value is evaluated at the middle epoch of observation to save the single angular value from the track, while the angular

rate is obtained from the first-order derivative evaluated at the same time.

A practical example is illustrated in Fig. 2.6, where the observation compression is performed on an optical track recorded by a ground station.

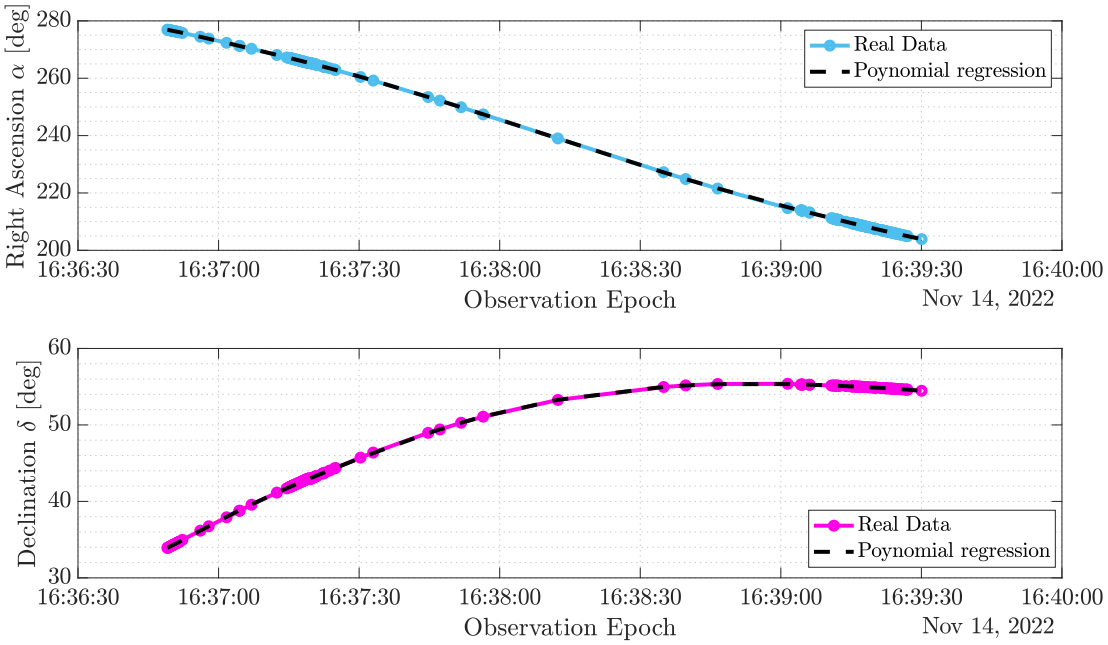

Figure 2.6: Optical observation tracks and regression polynomials.

2.2.3. Admissible region theory

As anticipated in the introduction of Sec. 2.2, the admissible region concept is a mathematical formulation describing a two-dimensional surface in the measurements space, such that the possible constraints on the orbital parameters of the observed object are satisfied. Imposing these conditions, the admissible region represents the locus of points of meaningful values in the measurements space. It was introduced to handle too-short arcs where classical methods for IOD failed, gathering all the information available to extract the maximum potential from ground-based observations [43].

The admissible region tool is founded on the knowledge of the attributable, which can be derived from an optical or radar observation. This distinction also generates a difference in the structure of the admissible region itself, as the two-dimensional surface will extend into the measurements space where the values have not been fixed by the corresponding

attributable, i.e. in the plane $(\rho, \dot{\rho})$ for the optical case, while in $(\dot{\alpha}, \dot{\delta})$ for the radar case. However, within this thesis, only the optical admissible region is employed.

Optical admissible region

Starting from the optical attributable $\mathcal{A}_{opt}$ of an Earth-orbiting RSO, as defined in Eq. 2.11, the idea is to derive deterministic conditions on the $(\rho, \dot{\rho})$-plane to bound the solution space, imposing the main orbital requirements on the orbiting objects. For this reason, the following physical constraints are derived:

i. **Geocentric specific energy**: the main requirement is that the geocentric energy of the object is negative so that the RSO is a satellite of the Earth. Thus, the constraint traduces in Eq. 2.15:

$$\mathcal{E}(\rho, \dot{\rho}) = \frac{1}{2} ||\dot{\mathbf{r}}(\rho, \dot{\rho})||^2 - \frac{\mu}{||\mathbf{r}(\rho)||} \leq 0 \tag{2.15}$$

where μ is the Earth's gravitational constant.
Substituting the definitions illustrated in Eq. 2.13 in the previous Sec. 2.2.1, it is possible to rewrite the Eq. 2.15 as:

$$\begin{aligned} 2\,\mathcal{E}(\rho, \dot{\rho}) = \dot{\rho}^2 + w_1\dot{\rho} + T(\rho) - \frac{2\mu}{\sqrt{S(\rho)}} \leq 0, \\ T(\rho) = w_2\rho^2 + w_3\rho + w_4, \quad S(\rho) = \rho^2 + w_5\rho + w_0 \end{aligned} \tag{2.16}$$

where the coefficients w_i are derived from the attributable [44]:

$$\begin{aligned} w_0 = ||\mathbf{q}||^2, \quad w_1 = 2\,\dot{\mathbf{q}} \cdot \hat{\boldsymbol{\rho}}, \quad w_2 = \dot{\alpha}^2 \cos\delta^2 + \dot{\delta}^2 = \eta^2, \\ w_3 = 2\,(\dot{\alpha}\,\dot{\mathbf{q}} \cdot \hat{\boldsymbol{\rho}}_\alpha + \dot{\delta}\,\dot{\mathbf{q}} \cdot \hat{\boldsymbol{\rho}}_\delta), \quad w_4 = ||\dot{\mathbf{q}}^2, \quad w_5 = 2\,\mathbf{q} \cdot \hat{\boldsymbol{\rho}} \end{aligned} \tag{2.17}$$

with η representing the object proper motion.
Another important condition, to obtain real solutions for $\dot{\rho}$ from Eq. 2.16, is the

non-negative discriminant of the second order polynomial expression:

$$\Delta = \frac{w_1^2}{4} - T(\rho) + \frac{2\mu}{\sqrt{S(\rho)}} \geq 0 \tag{2.18}$$

Resulting in the following condition on ρ:

$$\frac{2\mu}{\sqrt{S(\rho)}} \geq Q(\rho) = w_2 \,, \rho^2 + w_3\rho + \gamma, \quad \gamma = w_4 - \frac{w_1^2}{4} \tag{2.19}$$

To obtain a compact notation, it is possible to reformulate Eq. 2.19 as:

$$V(\rho) := Q^2(\rho)\, S(\rho) \leq 4\mu^2 \tag{2.20}$$

The admissible region on the $(\rho, \dot{\rho})$-plane is constrained by Eq. 2.16, while admissible values of ρ are additionally limited by Eq. 2.20. For this reason, it can admit more than one connected component, but it has at most two.

ii. **Range**: the admissible region needs to be compact enough to be sampled with a finite number of points. Thus, a simple condition to define an inner boundary is imposing constraints directly on the range ρ, allowing to focus on specific orbital regions such as LEO, MEO, and GEO:

$$\rho_{min} \leq \rho \leq \rho_{max} \tag{2.21}$$

iii. **Semi-major axis**: another possibility is imposing a condition on the semi-major axis, employing the formulation illustrated for the energy. Fixing a minimum value a_{min} and exploiting the Eq. 2.5, it is possible to constrain the semi-major axis a to be larger than a_{min} with:

$$a(\rho, \dot{\rho}) = -\frac{\mu}{2\mathcal{E}(\rho, \dot{\rho})} \geq a_{min} \longleftrightarrow \mathcal{E}(\rho, \dot{\rho}) \leq -\frac{\mu}{2a_{min}} = \mathcal{E}_{min} \tag{2.22}$$

defining another six-degree inequality as in Eq. 2.16, with the same coefficients of

the polynomial terms, but a different constant term.

A similar procedure can be applied to limit the maximum value of the semi-major axis, resulting in a condition superimposed on the one defined in Eq. 2.16.

iv. **Eccentricity**: energy is also related to eccentricity and angular momentum by:

$$\mathcal{E} = -\frac{\mu^2}{2\,||\mathbf{h}||^2}\,(1-e^2) \tag{2.23}$$

From this formulation, it is possible to define a constraint on the maximum eccentricity of the observed object, to increase the compactness of the admissible region with a strong geometrical condition. From the elaboration of Eq. 2.23, the following relation can be obtained:

$$e = \sqrt{1 + \frac{2\mathcal{E}\,||\mathbf{h}||^2}{\mu^2}} \leq e_{max} \tag{2.24}$$

To analytically develop the inequality, it is necessary to express the specific energy $\mathcal{E}$ and the angular momentum $\mathbf{h}$ as a function of the range ρ and range rate $\dot{\rho}$. For the energy, it is possible to use the dependency in Eq. 2.16, while the formulae for angular momentum are needed:

$$\mathbf{h}(\rho,\dot{\rho}) = \mathbf{r} \times \dot{\mathbf{r}} = \mathbf{D}\dot{\rho} + \mathbf{E}\rho^2 + \mathbf{F}\rho + \mathbf{G} \tag{2.25}$$

where

$$\begin{aligned} \mathbf{D} &= \mathbf{q}\times\hat{\boldsymbol{\rho}}\,, \qquad \mathbf{E} = \hat{\boldsymbol{\rho}}\times(\dot{\alpha}\,\hat{\boldsymbol{\rho}}_\alpha + \dot{\delta}\,\hat{\boldsymbol{\rho}}_\delta), \\ \mathbf{F} &= \mathbf{q}\times(\dot{\alpha}\,\hat{\boldsymbol{\rho}}_\alpha + \dot{\delta}\,\hat{\boldsymbol{\rho}}_\delta) + \hat{\boldsymbol{\rho}}\times\dot{\mathbf{q}}, \qquad \mathbf{G} = \mathbf{q}\times\dot{\mathbf{q}} \end{aligned} \tag{2.26}$$

Substituting Eq. 2.16 and Eq. 2.25 into Eq. 2.24, one obtains:

$$a_4\,\dot{\rho}^4 + a_3\,\dot{\rho}^3 + a_2\,\dot{\rho}^2 + a_1\,\dot{\rho} + a_0 \leq 0 \tag{2.27}$$

Before defining the dependency of the functions a_i with respect to the range ρ, it is preparatory to introduce other range-dependent quantities, in order to maintain a

compact notation:

$$\begin{aligned} P(\rho) &= 2\,\mathbf{D}\cdot\mathbf{E}\,\rho^2 + 2\,\mathbf{D}\cdot\mathbf{F}\,\rho + 2\,\mathbf{D}\cdot\mathbf{G} \\ U(\rho) &= ||\mathbf{E}||^2\,\rho^4 + 2\,\mathbf{E}\cdot\mathbf{F}\,\rho^3 + (2\,\mathbf{E}\cdot\mathbf{G} + ||\mathbf{F}||^2)\,\rho^2 + 2\,\mathbf{F}\cdot\mathbf{G}\,\rho + ||\mathbf{G}|| \end{aligned} \tag{2.28}$$

and

$$F(\rho) = w_2\,\rho^2 + w_3\,\rho + w_4 - \frac{2\mu}{\sqrt{\rho^2 + w_5\,\rho + w_0}} \tag{2.29}$$

Now, it is possible to describe the a_i $(i = 0, ..., 4)$ functions, exploiting the elements previously defined:

$$\begin{aligned} a_0 &= F(\rho)\,U(\rho) + \mu^2\,(1 - e^2) \\ a_1 &= F(\rho)\,P(\rho) + w_1\,U(\rho) \\ a_2 &= U(\rho) + ||\mathbf{D}||^2\,F(\rho) + w_1\,P(\rho) \\ a_3 &= P(\rho) + ||\mathbf{D}||^2\,w_1 \\ a_4 &= ||\mathbf{D}||^2 \end{aligned} \tag{2.30}$$

A final example of the optical admissible region is illustrated in Fig. 2.7, where the energy and semi-major axis constraints are represented, as well as the one on the maximum eccentricity and the minimum range.

This example is the result of an optical observation, taken from a virtual ground station, whose position in standard coordinates is $\Theta = \pi/3$ rad in polar angle (measured as polar angle from the north pole) and $\Phi = 0$ rad in azimuthal angle (measured from the inertial x axis), and the measured optical attributable is $\mathcal{A}_{opt}$ = (0 rad, $\pi/6$ rad, 0.1 rad/h, 0.03 rad/h), taken from [25] to validate the code used in this thesis.

Radar admissible region

Given a radar attributable $\mathcal{A}_{rad}$, as defined in Eq. 2.12, the radar admissible region is found on the $(\dot{\alpha}, \dot{\delta})$-plane with a procedure similar to that illustrated in the optical case, imposing constraints on physical quantities to delimit the region as done in [39]:

i. **Geocentric specific energy**: once again, the object must be an Earth satellite, so its geocentric energy must be less than zero. After some mathematical elaborations,

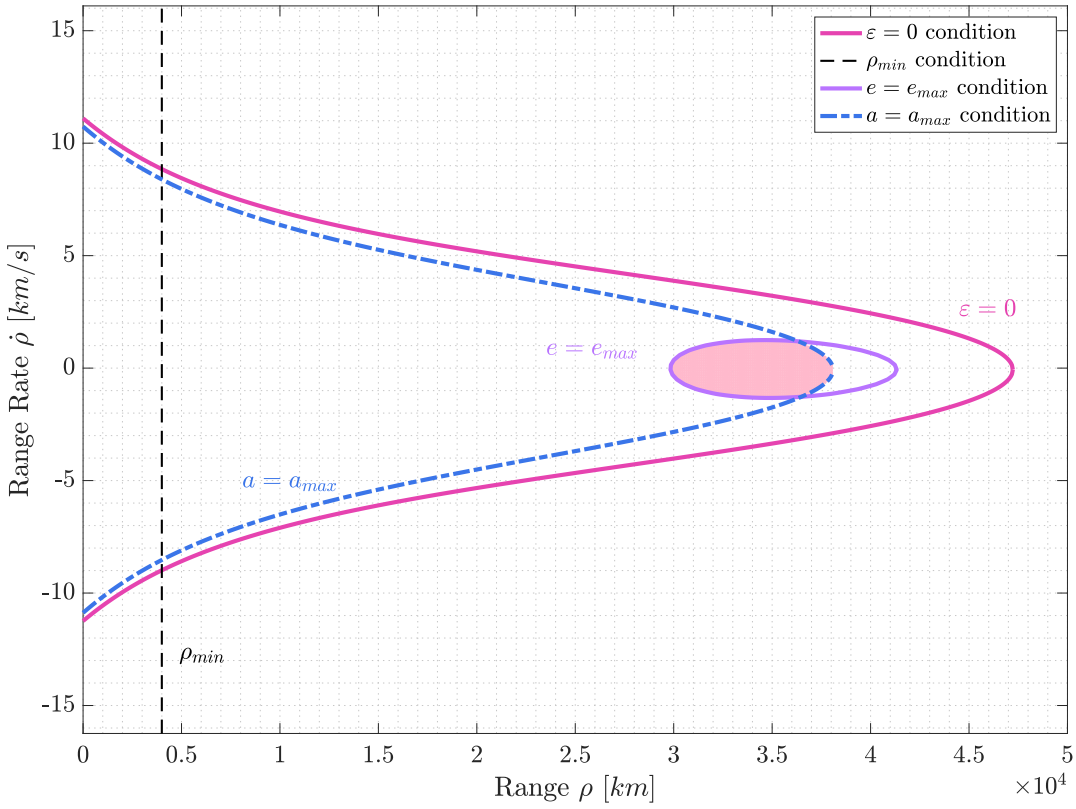

Figure 2.7: Optical admissible region, painted in *pink*.

the following condition is reached:

$$2\,\mathcal{E}(\alpha,\delta) \;=\; z_{11}\,\dot{\alpha}^2 + z_{22}\,\dot{\delta}^2 + 2z_{13}\dot{\alpha} + 2z_{23}\,\dot{\delta} + z_{33} \;\leq\; 0 \tag{2.31}$$

where z_{ij} depend on the attributable [44]:

$$\begin{aligned} z_{11} &= \rho^2\,\cos^2\delta, \qquad & z_{22} &= \rho^2, \qquad & z_{13} &= \rho\,\dot{\mathbf{q}}\cdot\hat{\boldsymbol{\rho}}_\alpha \\ z_{23} &= \rho\,\dot{\mathbf{q}}\cdot\hat{\boldsymbol{\rho}}_\delta, \qquad & z_{33} &= \dot{\rho}^2 + w_1\,\dot{\rho} + w_4 - \frac{2\mu}{\sqrt{S(\rho)}} \end{aligned} \tag{2.32}$$

The region is constrained by the negative geocentric energy circle, individuating a compact set on the $(\dot{\alpha},\dot{\delta})$-plane. It is also possible to derive a condition on the maximum semi-major axis a_{max}, defining $\mathcal{E}_{min}$ as in Eq. 2.5, and resulting in a concentric inner circle.

ii. **Perigee radius**: in order to exclude ballistic motions of the observed objects, it is possible to avoid trajectories impacting the Earth in less than one revolution with the inequality on the perigee radius presented in Eq. 2.33:

$$r_p = a(1-e) \geq r_{min} \tag{2.33}$$

Once again, before reaching the final form of this constraint, it is necessary to define the angular momentum formulation as function of the angle rates $(\dot{\alpha}, \dot{\delta})$:

$$\begin{gathered} \mathbf{c}(\dot{\alpha}, \dot{\delta}) = \mathbf{r} \times \dot{\mathbf{r}} = \mathbf{A}\dot{\alpha} + \mathbf{B}\dot{\delta} + \mathbf{C}, \\ \mathbf{A} = \rho\, \mathbf{r} \times \hat{\boldsymbol{\rho}}_{\alpha}, \qquad \mathbf{B} = \rho\, \mathbf{r} \times \hat{\boldsymbol{\rho}}_{\delta}, \qquad \mathbf{C} = \mathbf{r} \times \dot{\mathbf{q}} + \dot{\rho}\, \mathbf{q} \times \hat{\boldsymbol{\rho}} \end{gathered} \tag{2.34}$$

Then, by substituting Eq. 2.23, Eq. 2.31, and Eq. 2.34 into Eq. 2.33, the following second degree polynomial inequality can express the condition on the perigee:

$$l_{11}\,\dot{\alpha}^2 + 2\,l_{12}\,\dot{\alpha}\,\dot{\delta} + l_{22}\,\dot{\delta}^2 + 2\,l_{13}\,\dot{\alpha} + 2\,l_{23}\,\dot{\delta} + l_{33} \geq 0 \tag{2.35}$$

where

$$\begin{aligned} l_{11} &= ||\mathbf{A}||^2 - r_{min}^2\, z_{11}, \qquad l_{12} = \mathbf{A} \cdot \mathbf{B}, \\ l_{22} &= ||\mathbf{B}||^2 - r_{min}^2\, z_{22}, \qquad l_{23} = \mathbf{B} \cdot \mathbf{C} - r_{min}^2\, z_{23}, \\ l_{33} &= ||\mathbf{C}||^2 - r_{min}\,(r_{min}\, z_{33} + 2\mu), \qquad l_{13} = \mathbf{A} \cdot \mathbf{C} - r_{min}^2\, z_{13} \end{aligned} \tag{2.36}$$

This final polynomial condition can represent either an ellipse or a hyperbola, depending on the sign of $(l_{11}\,l_{22} - l_{23}^2)$.

To illustrate a theoretic example of the radar admissible region, the simulation of a LEO object was performed, and the radar attributable $\mathcal{A}_{rad}$ = (30 deg, 40 deg, 1870 km, 0.2 km/s) was obtained. Imposing constraints on the energy, semi-major axis, and perigee radius the region represented in Fig. 2.8 is obtained.

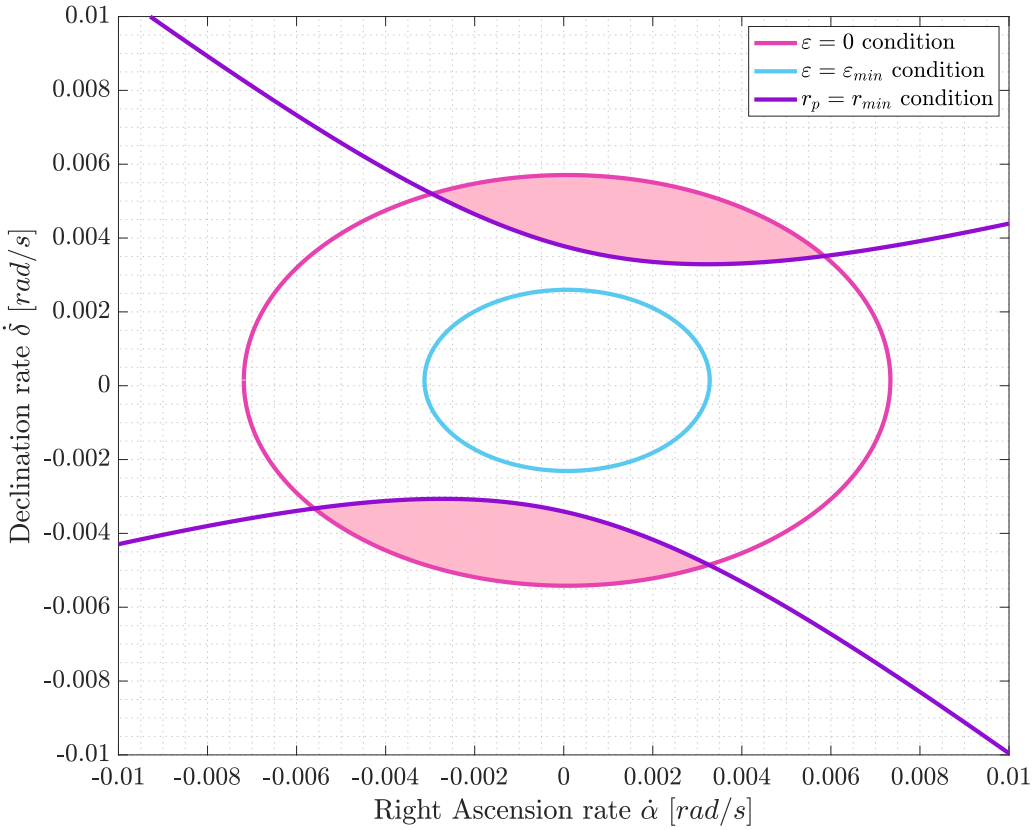

Figure 2.8: Radar admissible region, painted in *pink*.

2.2.4. Sampling and conversion to measurements space

The admissible region tool allows, sampling the area with a finite number of points, to find couples of meaningful values with which completing the initial optical or radar attributable $\mathcal{A}$ in the 6-dimensional measurements space composed by $[\alpha, \delta, \dot{\alpha}, \dot{\delta}, \rho, \dot{\rho}]$. In this way, exploiting the formulae presented in Sec. 2.2.1, the Cartesian position $\mathbf{r}$ and velocity $\dot{\mathbf{r}}$ can be easily retrieved, if the observer geocentric position $\mathbf{q}$ is available. Through N_i samplings of the admissible region, it is possible to obtain a set of admissible Cartesian states $\mathbf{x}_i$ to be propagated, starting from a single observation and without carrying out any process of orbit determination. This tool is totally deterministic, as it exploits physical constraints, and these characteristics give it great potential in the world of space engineering.

However, the reverse conversion from Cartesian to measurements space is not straight-

forward. Starting from a Cartesian state $\mathbf{x}_i$ in the inertial frame, with the observer geocentric position $\mathbf{q}$ and velocity $\dot{\mathbf{q}}$, the process begins retrieving the range vector $\boldsymbol{\rho}$ and measurement ρ, as well as the versor $\hat{\boldsymbol{\rho}}$, through the simple formulae in Eq. 2.37.

$$\boldsymbol{\rho} = \mathbf{r} - \mathbf{q}, \qquad \rho = ||\boldsymbol{\rho}||, \qquad \hat{\boldsymbol{\rho}} = \frac{\boldsymbol{\rho}}{\rho} \tag{2.37}$$

From Sec. 2.2.1 it is possible to recall that $\hat{\boldsymbol{\rho}} = (\cos\alpha\cos\delta, \sin\alpha\cos\delta, \sin\delta)$, and computing the ratio between the first two components of the vector allows to derive the right ascension α tangent, while the declination δ can be obtained from the third component:

$$\alpha = \arctan\left(\frac{\hat{\boldsymbol{\rho}}(2)}{\hat{\boldsymbol{\rho}}(1)}\right), \qquad \delta = \arcsin\hat{\boldsymbol{\rho}}(3) \tag{2.38}$$

with particular regard to the sign of the $\hat{\boldsymbol{\rho}}$ components for the arctangent computation. Furthermore, also $\hat{\boldsymbol{\rho}}_\alpha$ and $\hat{\boldsymbol{\rho}}_\delta$ are retrieved, being angles dependent only.
Then, from the mathematical elaboration of the formulae presented in Sec. 2.2.1, the range rate $\dot{\rho}$ is found, employing Eq. 2.39.

$$\dot{\rho} = \frac{1}{\rho}(\dot{\mathbf{r}} - \dot{\mathbf{q}}) \cdot (\mathbf{r} - \mathbf{q}) \tag{2.39}$$

Reversing Eq. 2.13, it is immediate to find $\dfrac{d\hat{\boldsymbol{\rho}}}{dt}$, which is the basis from which to derive the angular rates:

$$\frac{d\hat{\boldsymbol{\rho}}}{dt} = \frac{1}{\rho}(\dot{\mathbf{r}} - \dot{\mathbf{q}} - \dot{\rho}\,\hat{\boldsymbol{\rho}}) \tag{2.40}$$

Knowing that the third component of $\hat{\boldsymbol{\rho}}_\alpha$ is null, the third component relation of Eq. 2.13 is exploited to compute the declination rate $\dot{\delta}$:

$$\frac{d\hat{\boldsymbol{\rho}}}{dt}(3) = \dot{\delta}\,\hat{\boldsymbol{\rho}}_\delta(3) \longleftrightarrow \dot{\delta} = \frac{\dfrac{d\hat{\boldsymbol{\rho}}}{dt}(3)}{\hat{\boldsymbol{\rho}}_\delta(3)} \tag{2.41}$$

Finally, also $\dot{\alpha}$ is computed through the first (or the second) component of the same relation, in which it represents the only unknown:

$$\frac{d\hat{\boldsymbol{\rho}}}{dt}(1) = \dot{\alpha}\,\hat{\boldsymbol{\rho}}_\alpha(1) + \dot{\delta}\,\hat{\boldsymbol{\rho}}_\delta(1) \longleftrightarrow \dot{\alpha} = \frac{1}{\hat{\boldsymbol{\rho}}_\alpha(1)}\left(\frac{d\hat{\boldsymbol{\rho}}}{dt}(1) - \dot{\delta}\,\hat{\boldsymbol{\rho}}_\delta(1)\right) \tag{2.42}$$

2.3. Statistical Background

Some of the main statistical concepts are employed in this thesis and are here introduced to provide the basic tools necessary for understanding the work implemented.
Statistics plays a fundamental role in scientific research, allowing to quantify uncertainty, test hypotheses, and draw valid inferences. Descriptive statistics are used to summarize and present data in a meaningful manner, and the key concepts are illustrated:

- **Mean** ($\boldsymbol{\mu}_x$): or expected value, is a measure of central tendency representing the average value of a large set of numbers. It is found by computing the arithmetic mean, summing up all the values in the set, and dividing by the number of elements [45].
- **Probability Density Function** (PDF): is a function that describes the probability of a continuous random variable falling within a given range. The probability value is obtained by integrating the PDF in that range. It represents the distribution of the random variables around the mean, and different distribution families exist, such as the Gaussian (or normal) or the uniform.
- **Standard deviation** (σ_{xx}): is a measure of the amount of variation or dispersion in a set of values. It is a quantification of the spreading around the mean of the data points in the data set and it is usually the representation of the uncertainty of a certain variable.
- **Covariance** (σ_{xy}): is a measure of how much two random variables vary together. It is a key concept in multivariate statistics and is used to understand the joint variability of two random variables.
- **Covariance matrix** ($\boldsymbol{\Gamma}_x$): is a squared, symmetric, and positive semi-definite table,

that contains the covariances between all pairs of variables in the extra-diagonal positions, while it has the variances (squared value of the standard deviation) on the main diagonal, i.e. the covariance of each element with itself. It is used in multivariate analysis to understand the correlations between different variables [46].

- **Confidence region** (CR): is the multi-variate generalization of the uni-variate confidence interval, delimiting a space around the best-fit point that has a certain probability of containing the true value, assuming the model is correct. Confidence regions can measure the degree of uncertainty in a sampling method, and, defining α as the *confidence level*, it is possible to define the 100(1-α)% confidence region as the random volume with the (1-α) probability of containing the true value [47]. The most common are 95% and 99% confidence regions.

- **Mahalanobis distance** (MD): is the statistical measure of the distance between one point $\mathbf{x}$ and a distribution, characterized by mean $\boldsymbol{\mu}_x$ and covariance $\boldsymbol{\Gamma}_x$, in the multivariate space. It is defined as follows:

$$D(\mathbf{x}, \boldsymbol{\mu}) = \sqrt{(\mathbf{x} - \boldsymbol{\mu})^T \boldsymbol{\Gamma}_x^{-1} (\mathbf{x} - \boldsymbol{\mu})} \tag{2.43}$$

  The Mahalanobis distance finds wide applications in the field of multivariate statistics, especially with Gaussian distributions, and it differs from Euclidean distance in the way it takes into account the correlations between variables [48].

- **χ^2-test**: is a non-parametric statistical test to determine if the two or more classifications of the samples are independent or not [49]. There are two types of χ^2-tests:

  i. The χ^2 goodness of fit test is used to test whether the frequency distribution of a categorical variable is different from your expectations.

  ii. The χ^2 test of independence is used to test whether two categorical variables are related to each other.

  The χ^2 critical value in the context of the χ^2-test refers to the value of the test statistic that separates the rejection region from the acceptance region, and combining it with the Mahalanobis distance can be used to understand if a point can

belong to a Gaussian distribution.

2.4. Computational Background

In this section, the computational support tools for the development of the thesis work are briefly presented.

- **MATLAB** (MATrix LABoratory): is a multi-paradigm numerical computing environment and fourth-generation programming language. MATLAB allows matrix manipulations, plotting of functions and data, implementation of algorithms, creation of user interfaces, and interfacing with programs written in other languages, including C, C++, Java, Fortran, and Python [50].
  MATLAB is employed as the fundamental environment in which the thesis algorithms are developed, analyzed, and tested.

- **SPICE**: is an information system developed by the Navigation and Ancillary Information Facility (NAIF) to support NASA scientists in planning and interpreting scientific observations from space-borne instruments, and to assist NASA engineers involved in modeling, planning, and executing activities needed to conduct planetary exploration missions [51]. The SPICE system includes the SPICE Toolkit, a large collection of allied software, where the principal component is a library of application program interfaces needed to read the kernel files and calculate observation geometry parameters of interest.
  SPICE is here used to read TLEs, retrieve ground station positions, convert date format, and change reference frames.

The platform used for implementations and simulations runs an Intel Core i5 CPU @ 1.7 GHz processor.

3 | Method

This chapter delves into the core methodologies employed in the development and implementation of two algorithms, tailored to correlate fragments optical tracks to their respective fragmentation events. The paramount objective of this research endeavor is to enhance the precision and efficiency of space debris tracking and characterization, thereby bolstering the understanding of a certain fragmentation event. An accurate screening of the fragments allows to improve the debris cloud monitoring and modeling, planning new observations, and providing important contributions to the services provided by a SST system.

Both algorithms are based on the admissible region concept, and, although their function is the same, they both need to be explained and in-depth analyzed to highlight their differences and strengths.

3.1. TITA analysis

In the space engineering framework, TITA represents a correlation approach based on the admissible region tool, which consists in linking two observations through an intersection of their admissible surfaces in the topocentric measurements space.

The idea under this linkage methodology was proposed by Maruskin et al. [25] as a future development of their work in the track-to-track correlation for orbit determination, but it has never been implemented. Hence, the proposed algorithm focuses on developing this analysis for the first time, adapting it to the track-to-fragmentation problem, to assess if a certain observation is linked to a fragmentation event.

The concept of this methodology is based on the admissible region tool, which allows to perform propagation of admissible values starting from a single observation and without

any orbit determination result. This introduces a key feature of this algorithm, which can handle too-short arcs where the classical methods fail.
This algorithm is studied, tested, and presented on the results of optical surveys. However, its application to the radar case is possible and represents an interesting approach to expand the horizons of this method.

TITA algorithm

Let's consider the fragmentation of a space object orbiting around the Earth, whose blast-point position $\mathbf{p}^{blast}$ and epoch t_{blast} have already been characterized, as described in Sec. 1.6. From the propagation of the last parent object available ephemeris $\{\mathbf{x}^{eph}, t_{eph}\}$, it is possible to retrieve the final velocity of the object $\mathbf{v}^{blast}$, to find the complete Cartesian state of the parent at the fragmentation epoch $\mathbf{x}^{blast}$ in the Earth-Centered Inertial (ECI) reference frame.
Some hours later (at t_{obs}), one object is detected by an optical ground station, whose position $\mathbf{q}^{obs}$ and velocity $\dot{\mathbf{q}}^{obs}$ are provided in the ECI reference frame, recording a Tracking Data Message with pairs of angular measurements and related observation epochs. The final objective is to assess whether the object is correlated to the detected fragmentation event.
It is of fundamental importance to note that, before this algorithm is executed, some parameters must be initially set. These are the number of points for the density of the sampling grind N_{grid} and the filtering thresholds (ε_{cart}, ε_{α}, ε_{δ}, and ε_{ρ}), whose value depends on the orbital region in which this analysis is conducted. For this reason, an initial tuning phase of these parameters was performed for the main regions under analysis (LEO and GEO).
TITA algorithm is structured as follows, generating the flowchart represented in Fig. 3.4:

1. TDM information is extracted and the optical track is processed. The observation compression method, illustrated in Sec. 2.2.2, is employed to obtain the optical attributable $\mathcal{A}_{opt}^{obs} = (\alpha, \delta, \dot{\alpha}, \dot{\delta})$ of the observed object, retrieving one single value for the right ascension, the declination and their rates, defined in the inertial reference frame centered in the ground station position. In this way, it is possible to define a

single set of data ($\mathcal{A}_{opt}^{obs}$) at a specific time (t_{obs}).

2. Once the optical attributable is obtained, it is possible to define the admissible region in the measurements $(\rho, \dot{\rho})$-plane, given the ground station position $\mathbf{q}^{obs}$ and velocity $\dot{\mathbf{q}}^{obs}$. The orbital constraints, introduced to limit the region, are general conditions of membership to certain orbital zones, already known when the object is observed.

3. The admissible region found is sampled with a rectangular grid of N_{grid} points per side, where N_{grid} is a setting parameter. In this way, N_i couples of admissible $(\rho, \dot{\rho})$ values are find, as well as N_i full admissible attributable ($\mathcal{A}_i^{obs} = (\alpha, \delta, \dot{\alpha}, \dot{\delta}, \rho_i, \dot{\rho}_i)$) in the 6-dimension measurements space, as presented in Fig. 3.1.

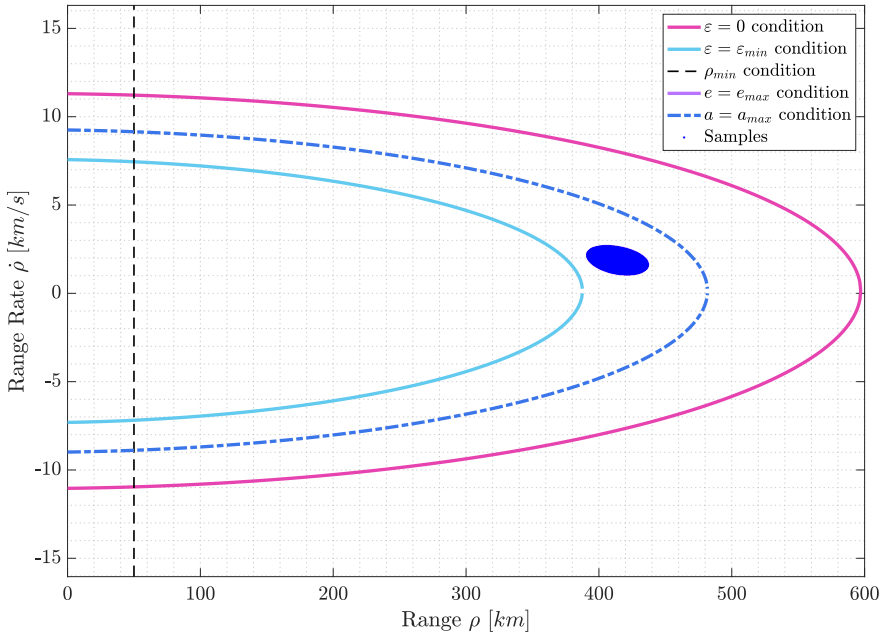

Figure 3.1: Sampled optical admissible region at t_{obs}.

4. Admissible attributable found at t_{obs} are converted from the measurements to the Cartesian space through the equations defined in Sec. 2.2.1, obtaining virtual debris in the ECI reference frame. N_i admissible states $\mathbf{x}_i^{obs}$ are found.

5. Admissible states are propagated backward in time to reach the known fragmentation epoch t_{blast}, defining the $\mathbf{x}_i^{blast} = [\mathbf{p}_i^{blast}, \mathbf{v}_i^{blast}]$ states of the VD at the moment

of the fragmentation.

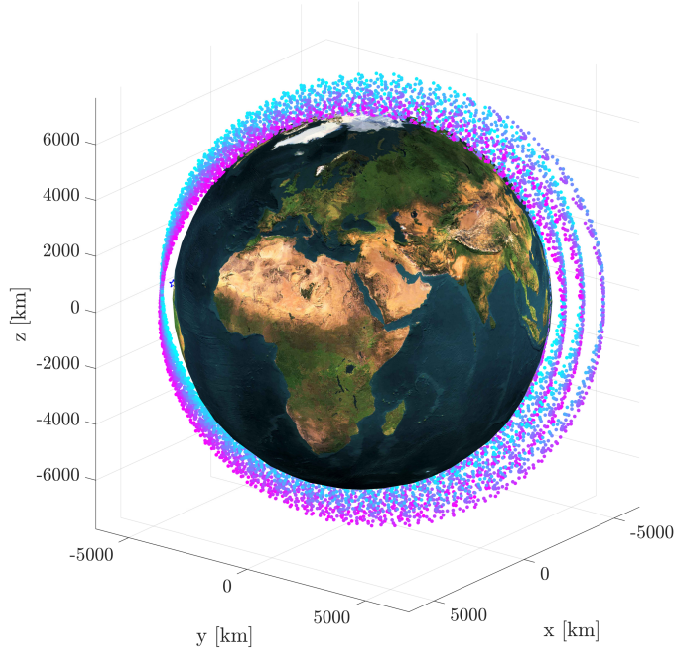

Figure 3.2: Propagated virtual debris at t_{blast} in the ECI reference frame.

6. To characterize the measurements space at t_{blast}, a virtual ground station is projected on the Earth's surface from the real position of the fragmentation $\mathbf{p}^{blast}$, to simulate a near-Zenith observation of the event. In particular, the latitude ϕ and longitude λ of the fragmentation projection are modified adding one degree to avoid an observation completely at the Zenith, and the geographical coordinates of the station are found as:

$$\begin{aligned} \phi_{station} &= \phi_{frag} + 1\,\text{deg} \\ \lambda_{station} &= \lambda_{frag} + 1\,\text{deg} \end{aligned} \tag{3.1}$$

   By this way, knowing the fragmentation epoch t_{blast}, it is straightforward computing the virtual ground station position $\mathbf{q}^{blast}$ and velocity $\dot{\mathbf{q}}^{blast}$.

7. The filtering phase consists in a reachability analysis that correlates the observed object only if, at t_{blast}, any VD approaches the fragmentation position both in the

Cartesian and measurements space. Note that the compatibility conditions regard only position-dependent quantities since parent object and fragments had different velocities at t_{blast}.

i. The first pruning filter is based on the Cartesian distance between the positions of VD $\mathbf{p}_i^{blast}$ and parent object $\mathbf{p}^{blast}$ at t_{blast}.
The condition to pass the filter is shown in Eq. 3.2:

$$\sqrt{(\mathbf{p}(1)-\mathbf{p}_i(1))^2+(\mathbf{p}(2)-\mathbf{p}_i(2))^2+(\mathbf{p}(3)-\mathbf{p}_i(4))^2}\frac{1}{R_E} \leq \varepsilon_{cart} \tag{3.2}$$

where ε_{cart} is a setting threshold, while R_E is the Earth's radius introduced for the normalization. Only the VD that satisfy this condition will have access to the next steps.

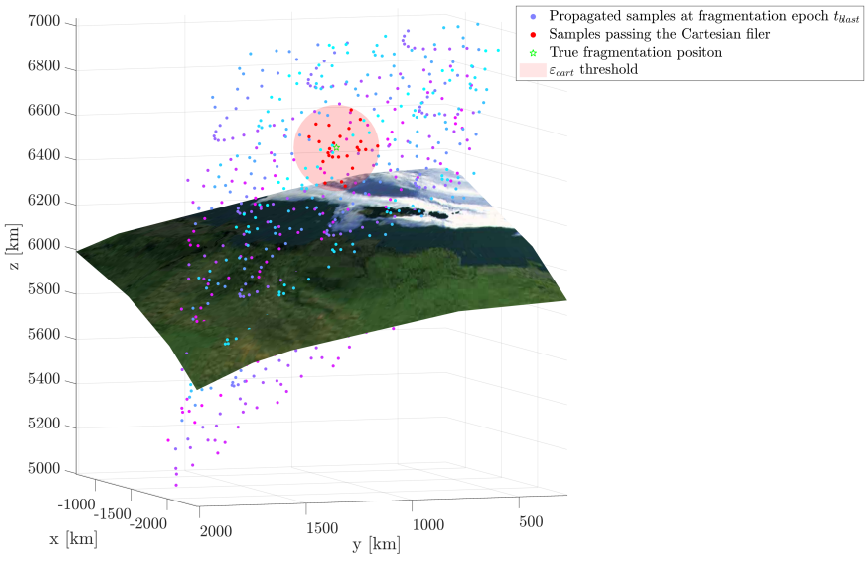

Figure 3.3: Cartesian filter results at t_{blast} in the ECI reference frame.

Once Cartesian samples have been filtered, the states $\mathbf{x}_i^{blast}$ of the surviving VD are transformed into the measurements space, defined by the virtual observer $\mathbf{q}^{blast}$ and $\dot{\mathbf{q}}^{blast}$, through the passages illustrated in Sec. 2.2.4. The same happens with the parent fragmentation state $\mathbf{x}^{blast}$.

The outcome of this process will be a set of pruned attributable $\mathcal{A}_i^{blast} = (\alpha_i, \delta_i, \dot{\alpha}_i, \dot{\delta}_i, \rho_i, \dot{\rho}_i)$, conversion of the surviving VD states, and the single attributable of the parent at the fragmentation epoch $\mathcal{A}^{blast} = (\alpha, \delta, \dot{\alpha}, \dot{\delta}, \rho, \dot{\rho})$.

ii. Next, samples enter the second pruning filter. This is implemented in the measurements space and is characterized by a triple-level waterfall structure, in which three pruning conditions are placed in series:

- Condition on the right ascension α: $|\alpha - \alpha_i| \leq \varepsilon_\alpha$
- Condition on the declination δ: $|\delta - \delta_i| \leq \varepsilon_\delta$
- Condition on the range ρ: $|\rho - \rho_i| \dfrac{1}{R_E} \leq \varepsilon_\rho$

where ε_α, ε_δ, and ε_ρ are setting thresholds. Note that the measurements involved in the filtering procedure are position-dependent only.
One VD can have access to subsequent levels of the filter only if satisfies the previous conditions, and it is not pruned only if all conditions are met at the same time.

8. The final stage concerns the velocity compatibility between positive VD, if there are any left, and the parent object at the fragmentation epoch. Even if parent object and fragments have different velocities at t_{blast}, due to the dynamics of the fragmentation event, the difference cannot be arbitrarily big and should be checked before confirming the correlation.
The norm of the difference between the Cartesian velocities is computed and, once again, compared to a maximum value of Δv, that can occur in a fragmentation event:

$$\Delta v = ||\mathbf{v}^{blast} - \mathbf{v}_i^{blast}|| \leq \Delta v_{max} \tag{3.3}$$

where the Δv_{max} threshold is set equal to 500 m/s.
If this test is also positive for at least one of the propagated VD, the observed object, related to the initial optical track, is considered *correlated* to the fragmentation event. If none of the VD passes all tests, then the object is considered *uncorrelated*.

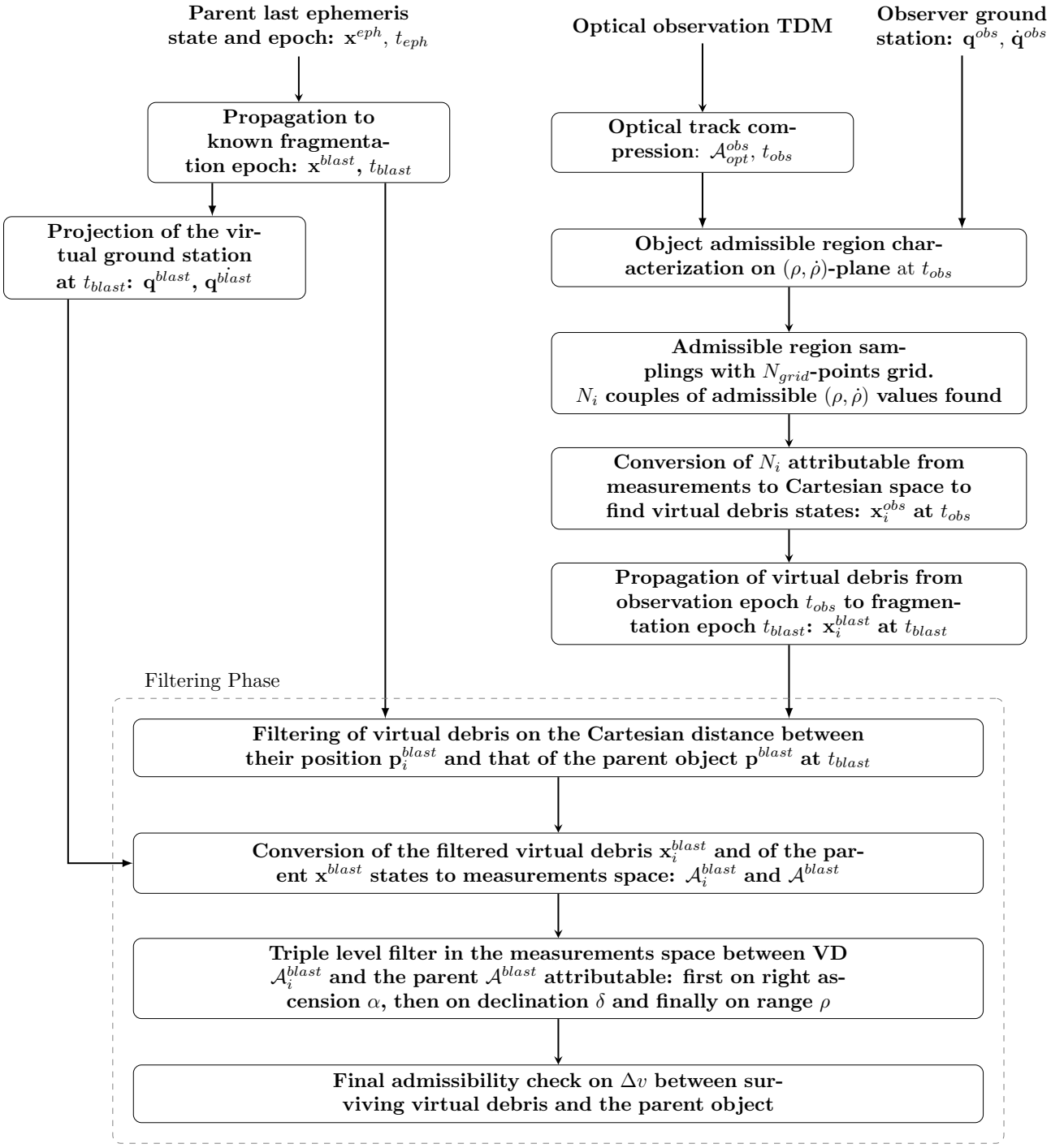

Figure 3.4: TITA algorithm flowchart.

3.2. OPIA analysis

The second method developed for the correlation of observations to a fragmentation event is called OPIA and it is based on the admissible region concept as well as TITA, but exploiting a more statistical-focused approach for the correlation process.
The algorithm preserves the key features of the admissible region tool, handling too-short arcs without orbit determination results, but the intersection analysis is performed in the orbital elements space, with particular focus on the inclination i and on the right ascension of the ascending node RAAN.
These parameters describing the orbital plane exhibit very slow variations due to orbital perturbations, and even during a fragmentation event many fragments preserve inclination and RAAN similar to those of the parent object. For this reason, it is possible to compare these quantities without performing propagation, i.e. comparing the parent and the fragment inclination and RAAN even if characterized at different times. In the process, the propagation step is therefore inserted only to guarantee a coherent comparison of the orbital parameters, but it is then removed to exploit the advantages linked to a code without propagation.
In the algorithm, the NASA Standard Breakup Model [52] is employed to simulate fragments distribution after the fragmentation, taking advantage of its modeling features to gain an initial comprehension of the fragmentation event. This satellite breakup model describes the outcome of a satellite breakup (explosion or collision) in terms of fragments size, area-to-mass ratio (A/M), and Δv distributions.
Furthermore, it is also worth pointing out that this method does not require threshold parameters to be set, except in the number of elements N_{grid} of the grid, making the algorithm extremely automated.

OPIA algorithm

Let's consider an Earth-orbiting object that is suspected of having caused a fragmentation event at t_{blast}. The only information about the parent object is the last recorded ephemeris, in which the parent state $\mathbf{x}^{eph}$ is characterized at the ephemeris epoch t_{eph} (where t_{eph}

$< t_{blast}$). Propagating this state to the fragmentation epoch it is possible to retrieve the parent state $\mathbf{x}^{blast}$ at t_{blast} in the ECI reference frame.

Hereafter, an uncatalogued RSO is detected by an optical survey some hours later (at t_{obs}) and the outcome of the optical observation is saved, once again, in a TDM. The observer ground station position $\mathbf{q}^{obs}$ and velocity $\dot{\mathbf{q}}^{obs}$ are provided.

Once again, the algorithm final goal is to understand if this object can be a fragment correlated to the fragmentation event of the parent object under analysis.

Here the main steps of the OPIA algorithm are presented, while the flowchart is illustrated in Fig. 3.8. The initial part of the process is shared with TITA, so its description will be summarized to avoid repetitions:

1. The TDM information is extracted and compressed in the same way described for TITA, obtaining the optical attributable $\mathcal{A}_{opt}^{obs} = (\alpha, \delta, \dot{\alpha}, \dot{\delta})$ of the observed object at t_{obs}.

2. The admissible region is characterized on the $(\rho, \dot{\rho})$-plane, introducing orbital constraints as described in Sec. 3.1.

3. The admissible region is sampled with a rectangular grid of N_{grid} points per side, to find N_i couples of admissible $(\rho, \dot{\rho})$ values. In this way, N_i full attributable $\mathcal{A}_i^{obs}$ are obtained at t_{obs}.

4. The admissible attributable are converted from measurements space to ECI reference frame, retrieving N_i admissible states $\mathbf{x}_i^{obs}$ at t_{obs}, corresponding to N_i VD.

5. The admissible states $\mathbf{x}_i^{obs}$ found at t_{obs} are propagated backward in time to reach the known fragmentation epoch t_{blast}, defining the $\mathbf{x}_i^{blast} = [\mathbf{p}_i^{blast}, \mathbf{v}_i^{blast}]$ states of the VD. As explained later, this step can be skipped to obtain an algorithm free from the propagation process, taking advantage of the low sensitivity of inclination and RAAN to orbital perturbations to develop the same analysis described below at t_{obs}.

   Here ends the part of the algorithm shared with TITA, starting an exclusive processing explained in detail below.

6. From the admissible states $\mathbf{x}_i^{blast}$ it is possible to compute the Keplerian parameters

of the VD at t_{blast}, reaching N_i set of six orbital parameters $\mathrm{X}_i^{blast} = (a_i, e_i, i_i, \Omega_i, \omega_i, \theta_i)$. As described in Sec. 2.1.2, some orbital parameters are less sensitive than others to orbital perturbation, especially in the short-term analysis. In particular, inclination and RAAN are quantities that are slightly affected in the short-period propagation, and this is exploited to correlate (or un-correlate) the observation to the parent object.

7. The analysis moves into the (i, Ω)-plane, where N_i couples of values are found at t_{blast}, corresponding to the VD inclination and RAAN, projection of the admissible region in this space. The shape of the distribution is described through the Gaussian (or normal) assumption, so that the samples mean $\boldsymbol{\mu}_{\mathrm{VD}}$ and covariance $\boldsymbol{\Gamma}_{\mathrm{VD}}$ can be computed, as represented in Fig. 3.5. The confidence interval of the covariance ellipse is set to 99.8% and this will be valid for all the covariance ellipses plotted from now on.

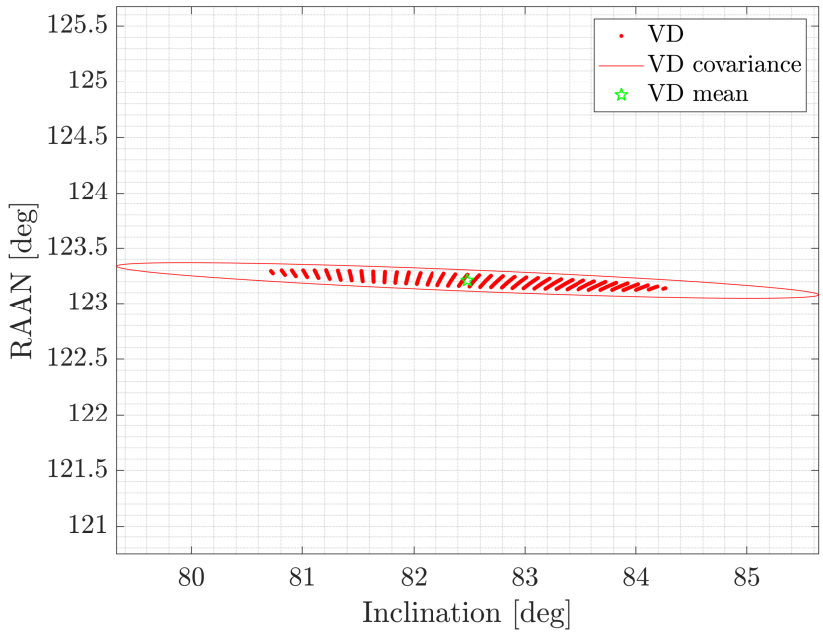

Figure 3.5: Mean and covariance on (i, Ω)-plane of the virtual debris generated from the admissible region and propagated to t_{blast}.

8. Focusing now on the parent object state $\mathbf{x}^{blast}$ at the fragmentation epoch t_{blast}, it is possible to apply the NASA Standard Breakup Model to find the virtual distribution

of fragments after the event. In this way, N_k fragments states $\mathbf{x}_k^{blast}$ are retrieved in the ECI reference frame at t_{blast}.

9. Virtual Fragments (VFs) states are converted into the Keplerian space, obtaining N_k set of orbital parameters $\mathrm{X}_k^{blast} = (a_k, e_k, i_k, \Omega_k, \omega_k, \theta_k)$.

10. Also in this case, the distribution of VFs inclinations and RAAN on the (i, Ω)-plane is described as Gaussian. Thus, the sample mean $\boldsymbol{\mu}_{\mathrm{VF}}$ and covariance $\boldsymbol{\Gamma}_{\mathrm{VF}}$ at t_{blast} are computed.

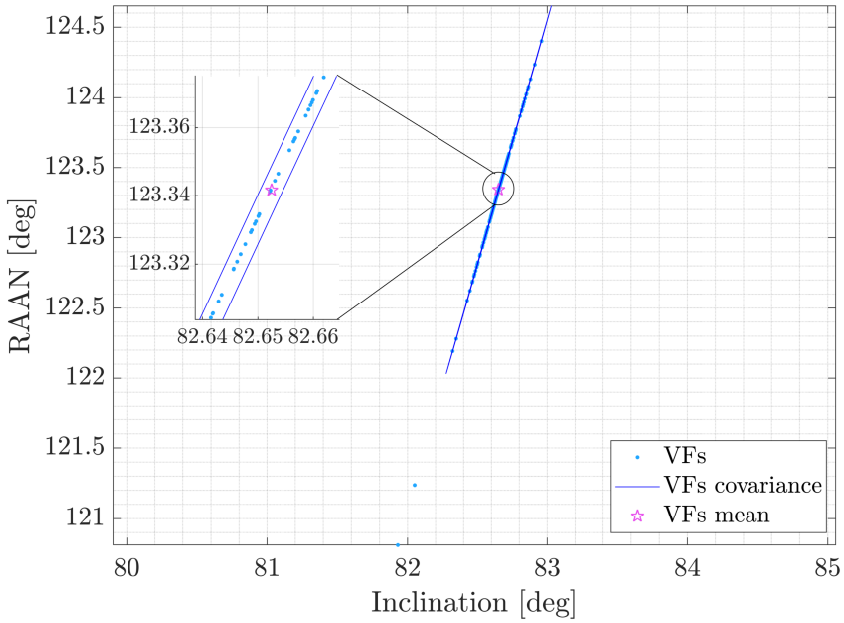

Figure 3.6: Mean and covariance on (i, Ω)-plane of the virtual fragments generated by applying the NASA Standard Breakup Model to the parent state at t_{blast}.

11. The correlating phase consists in evaluating the statistical distance between the two distributions found at the previous points. This is done employing the Mahalanobis distance metric, illustrated in Sec. 2.3, and the main steps are:

    - Computation of the squared Mahalanobis distance $D^2(\boldsymbol{\mu}_{\mathrm{VD}}, \boldsymbol{\mu}_{\mathrm{VF}})$ between the distributions:

$$D^2(\boldsymbol{\mu}_{\mathrm{VD}}, \boldsymbol{\mu}_{\mathrm{VF}}) = (\boldsymbol{\mu}_{\mathrm{VD}} - \boldsymbol{\mu}_{\mathrm{VF}})^T (\boldsymbol{\Gamma}_{\mathrm{VD}} + \boldsymbol{\Gamma}_{\mathrm{VF}})^{-1} (\boldsymbol{\mu}_{\mathrm{VD}} - \boldsymbol{\mu}_{\mathrm{VF}}) \tag{3.4}$$

- Characterization of the χ^2 critical value for the interval of confidence set (99.8%), through the MATLAB ® function `chi2inv`;
- Finally, finding the correlation index R (or coefficient) as:

$$R = \left| \frac{D^2}{\chi^2} \right| \tag{3.5}$$

Eventually, if the computed correlation index R is below a certain threshold $R_{max} = 1$ the object is *correlated* to the fragmentation event, otherwise the object is considered *uncorrelated*. This is not absolutely true since, from the statistical point of view, this test tells that there is a 0.02% (1-99.8%) of probability to find a true correlation characterized by a coefficient above the R_{min} threshold. However, these cases do not deteriorate the code performance and the same analysis will be performed without variations. An example of a positive correlation is depicted in Fig. 3.7, which combines the means and covariances plots illustrated in Fig. 3.5 and Fig. 3.6.

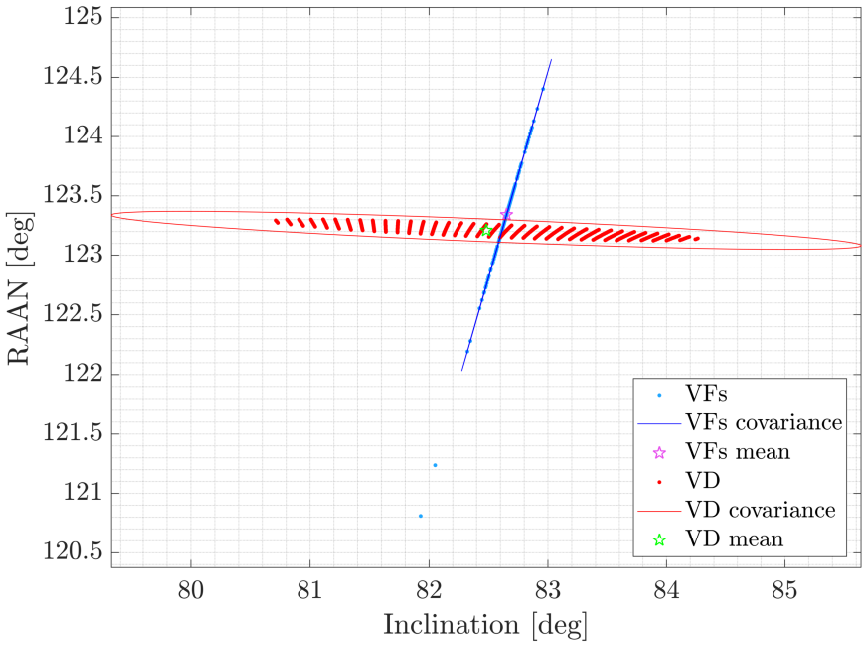

Figure 3.7: Means and covariances on (i, Ω)-plane of the virtual debris and virtual fragments distributions found at t_{blast}.

As introduced previously, the algorithm works in the same way even if VD propagation is avoided and $\boldsymbol{\mu}_{\text{VD}}$ and $\boldsymbol{\Gamma}_{\text{VD}}$ are found at t_{obs}, as the variations in inclination and RAAN are negligible in the time horizon considered in this analysis. For this reason, the results shown for OPIA will not include the propagation step since this reduces the computational cost without causing a degradation in accuracy.

An important final remark is that it is possible to perform the implemented analysis even if the fragmentation event is not characterized yet. Starting from the last parent ephemeris $\{\mathbf{x}^{eph}, t_{eph}\}$, it is possible to apply the NASA Standard Breakup Model here, without performing any propagation to the unknown fragmentation epoch. The VFs distribution in the (i, Ω)-plane can be considered accurate enough, even if not performed at t_{blast}, due to the low sensitivity of these orbital parameters, and low performance degradation is experienced.

This allows to link the fragment and the parent before the characterization of the event itself, improving and speeding up the cloud monitoring process.

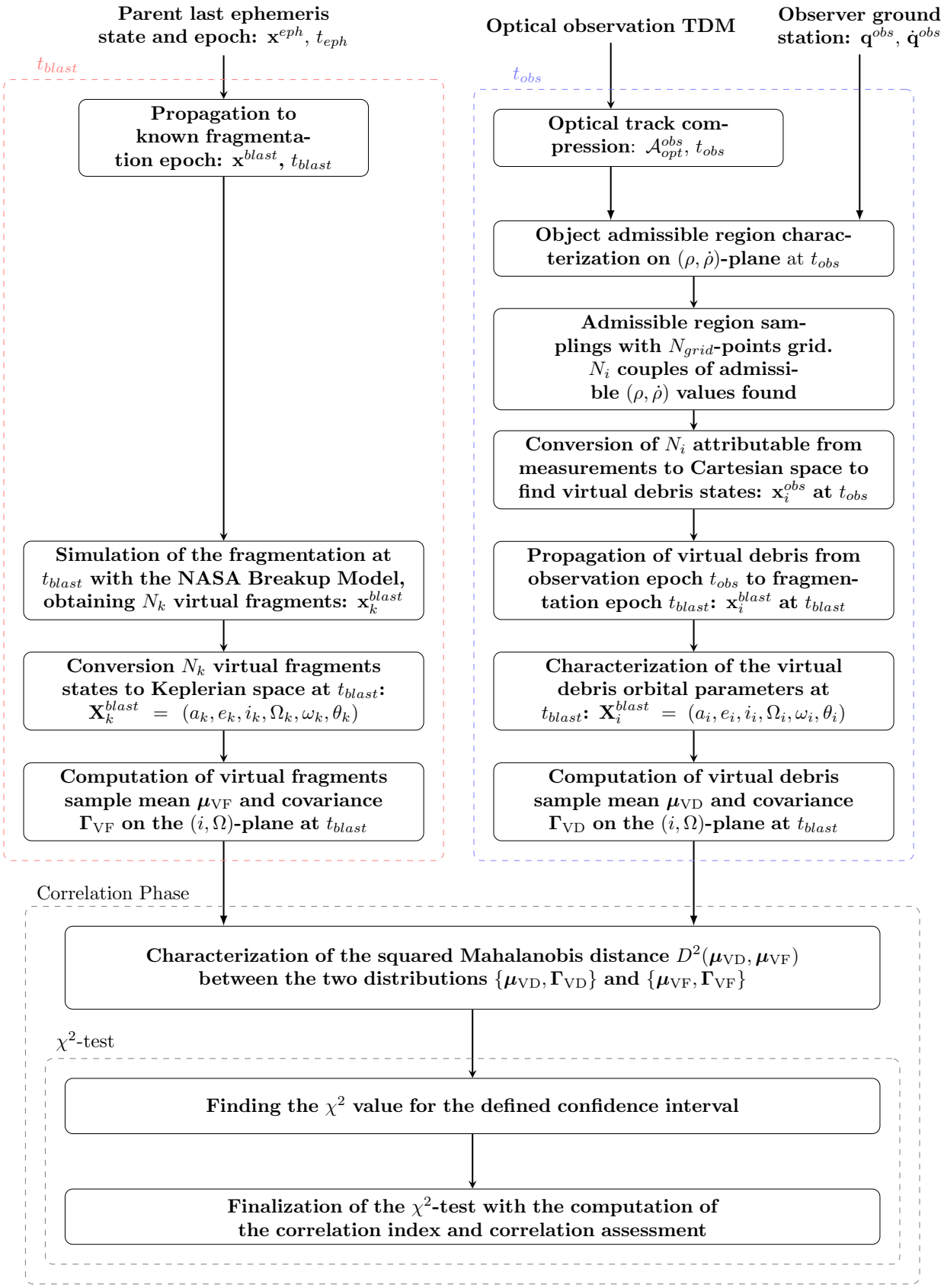

Figure 3.8: OPIA algorithm flowchart.

4 | Simulations and Results

The primary objective of this chapter is to evaluate the effectiveness and accuracy of the algorithms developed through numerical simulations implemented in the MATLAB ® environment.

The first Sec. 4.1 is devoted to the description of how testing data sets are generated, with simulated fragmentation events used to generate observations of correlated objects. However, also uncorrelated objects need to be simulated, to analyze the algorithm ability to avoid fake correlations.

Then, the basic performance of the codes is assessed in Sec. 4.2, excluding all the possible measurements noise or errors in an unperturbed scenario. The actual sensitivity analysis is performed in Sec. 4.3, where the performance degradation of the algorithms is analyzed, introducing measurements noise, error in the parent state, error in the fragmentation epoch, and propagation mismatching.

4.1. Data set generation

The final aim of the implemented algorithms is to correlate observations of fragments generated by the fragmentation event, excluding objects that are not involved.

To test the performance and the accuracy of the methods described in Ch. 3, a fragmentation event needs to be simulated, to provide virtual observations of correlated fragments. This is done employing the NASA Standard Breakup Model [52], which allows to retrieve a representative set of fragments just after the event, available for the propagation and observation simulation.

It is worth to point out that space objects not related to the event need to be generated to test the ability of the algorithm in avoiding wrong associations, and, for this purpose, the

Space-Track site [53] is exploited. This is a web platform operated by the United States Space Command (USSPACECOM) that provides access to a wide range of unclassified information related to space activities, such as satellite catalogue, TLEs, and orbital decay predictions. In particular, the site is exploited to obtain TLEs of generic satellites. By this way, a space object catalogue is defined, including both simulated fragments and satellites not related to the breakup. The numerical simulation processes this catalogue to investigate for possible correlations to an alerted fragmentation event.
The performance analysis is conducted both with LEO and GEO scenarios, to verify the sensitivity of the algorithms to the orbital region. For this reason, two different data sets are generated.

4.1.1. Data set in LEO

The fragmentation scenario investigated in LEO is related to the explosion of the Soviet electronic intelligence (ELINT) satellite COSMOS 1408 (1982-092A) [54], induced by a kinetic anti-satellite test which occurred around 02:47 UTC of November 15$^{\text{th}}$, 2021 [55]. The abandoned spacecraft, belonging to the Tselina-D class, generated a debris cloud comprising more than 1700 trackable pieces, about 1300 of which larger than 10 cm, as well as about 60,000 fragments greater than 1 cm. The event is considered to have already been characterized and the orbital parameters of the satellite at the fragmentation epoch are gathered in Tab. 4.1.

a [km]	e [-]	i [deg]	Ω [deg]	ω [deg]	θ [deg]
6862.2	2.851e-03	82.67	123.40	91.92	341.85

Table 4.1: Orbital parameters of COSMOS 1408 at the fragmentation epoch.

From here, it is necessary to illustrate in detail how fragments are simulated, distinguishing the two cases described above:

- **Correlated objects**: starting from the last COSMOS 1408 available TLE on the Space-Track platform $\{\mathbf{x}^{eph}, t_{eph}\}$, the satellite state is propagated to the known fragmentation epoch t_{blast} to characterize spacecraft position $\mathbf{p}^{blast}$ and velocity $\mathbf{v}^{blast}$ at the impact.

Here, the NASA Standard Breakup Model is applied to shape the physical and orbital characteristics of the resulting fragments. A set of Δv impulses is retrieved, to define 237 fragments generated by the fragmentation event. The evolution of the fragments cloud is displayed in Fig. 4.1.

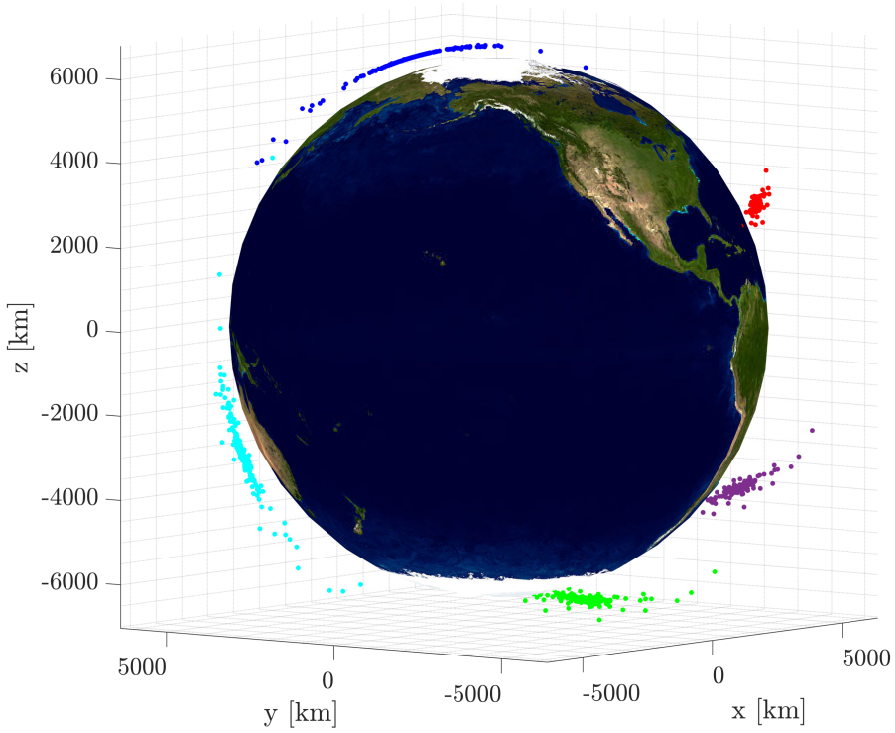

Figure 4.1: Evolution of the simulated fragments cloud from COSMOS 1408 fragmentation in the ECI reference frame. The time evolution can be followed through the colored clouds starting from the red one, after only a quarter of the period from the fragmentation, to then proceed with the purple one, the green one, the cyan one, and the blue one, after a complete period from the fragmentation.

Then, fragments states $\mathbf{x}_{fg}^{blast}$ are propagated to the observation epoch t_{obs}, assumed to be 1 day after the event (around 02:47 UTC of November 16$^{\text{th}}$). Here, a virtual ground station, retrieved in the same way described in Sec. 3.1, simulates an optical survey and obtains the complete data set to initiate the algorithms.

- **Uncorrelated objects**: the satellite catalogue is downloaded from the Space-Track site, to get the TLEs of the orbiting objects tracked around the Earth. The states of the objects $\mathbf{x}_i^{TLE}$ are extracted and each of them is characterized at the time of the

corresponding TLE t_i^{TLE}.

Before simulating the observations, objects orbital parameters X_i^{TLE} are found, converting their Cartesian state into the Keplerian space. Constraints are imposed on the semi-major axis a and eccentricity e, in order to filter out elements outside the LEO region. The resulting set of objects is represented in Fig. 4.2, with 2919 elements obtained from this procedure.

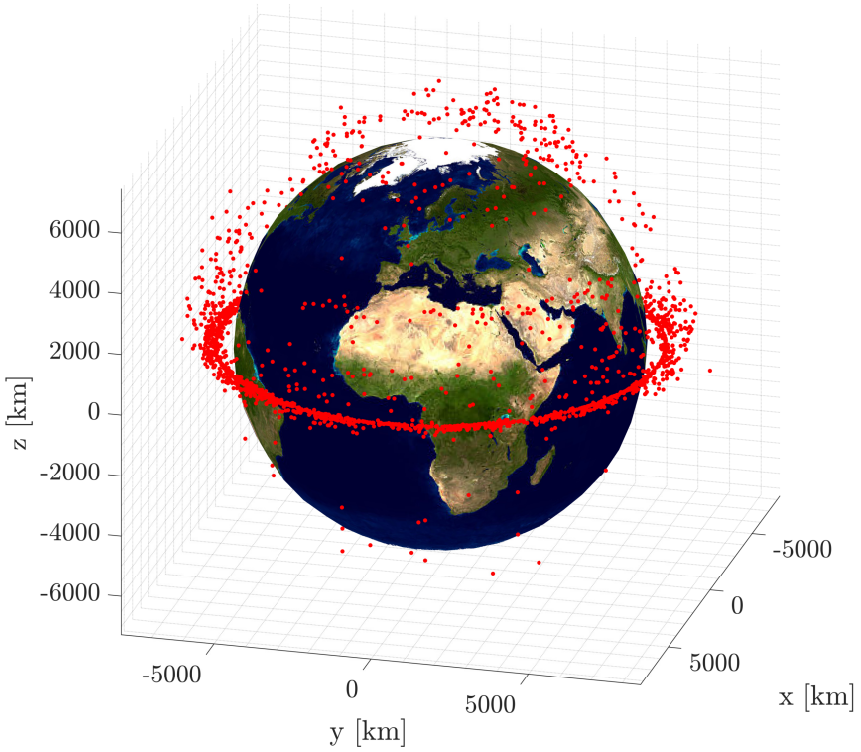

Figure 4.2: LEO satellites tracked on the Space-Track platform in the ECI reference frame, employed as uncorrelated objects to test the algorithm performance.

In this case, no propagation is performed and the observation is simulated at the corresponding TLE time ($t_i^{obs} = t_i^{TLE}$), which, contrary to the correlated case, is not unique. For this reason, the time window under analysis is ranging between one and two days after the fragmentation epoch.

Hence, the virtual observatory is projected and the optical observation is obtained, and the procedures are ready to start.

4.1.2. Data set in GEO

The modeling of a fragmentation event within the confines of GEO is here outlined. In this case, however, the scenario under analysis does not reproduce a real fragmentation event but simulates it on the base of a still active GEO satellite.
The spacecraft involved in this virtual fragmentation is EUTELSAT 7C, a high-power broadcast satellite for markets in Africa, Europe, and Middle East [56], whose virtual fragmentation epoch was set at 05:31 UTC of July 9$^{\text{th}}$, 2023. The satellite manufactured by Maxar Technologies ® was launched on 20$^{\text{th}}$ June 2019 and, at the fictitious fragmentation epoch, its orbit is characterized by the Keplerian elements represented in Tab. 4.2.

a [km]	e [-]	i [deg]	Ω [deg]	ω [deg]	θ [deg]
42166.02	3.092e-04	0.098	112.01	340.72	282.34

Table 4.2: Orbital parameters of EUTELSAT 7C at the virtual fragmentation epoch.

Once again, two different data sets are generated, to test positive and negative correlations:

- **Correlated objects**: similarly to the process performed in the LEO region, the state is extracted from the last available TLE on Space-Track and propagated to the epoch of the event. Then, the NASA Standard Breakup Model is applied, resulting again in 237 fragments that compose a debris cloud to be propagated up to the observation epoch. This time, t_{obs} is assumed to be at 10:19 UTC of July 10$^{\text{th}}$, around 1.2 days after the fragmentation.
  The evolution of the debris cloud is characterized in Fig. 4.3. Therefore, optical surveys are simulated, and all the input data are finally computed.

- **Uncorrelated objects**: uncorrelated elements are derived from the Space-Track catalogue, downloaded the day after the simulated fragmentation epoch. The resulting set of objects is filtered based on their semi-major axis a and eccentricity e, isolating 798 elements in the GEO region as illustrated in Fig. 4.4. The time window from the fragmentation event ranges between one and two days.

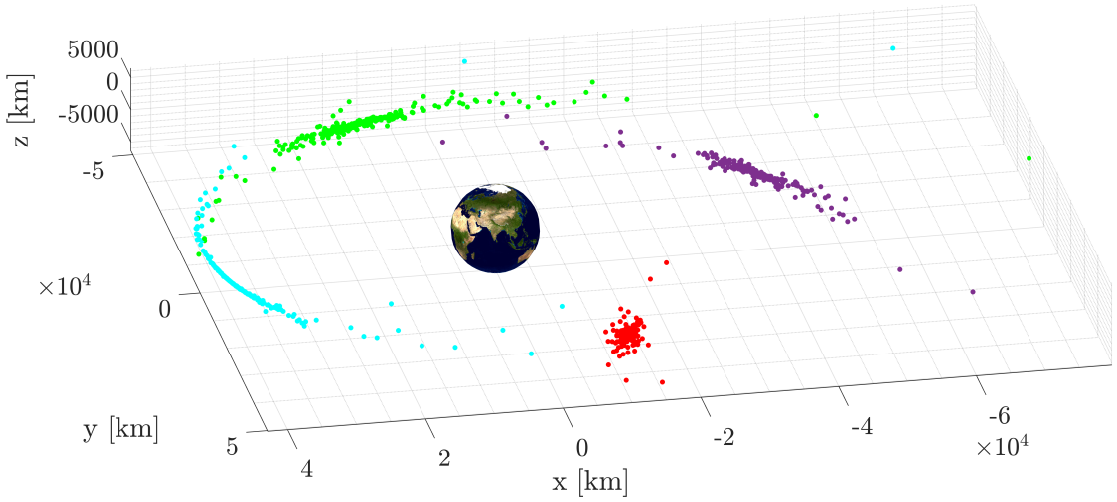

Figure 4.3: Evolution of the simulated fragments cloud from EUTELSAT 7C fragmentation in the ECI reference frame. The time evolution can be followed through the colored clouds starting from the red one, after only a quarter of the period from the fragmentation, to then proceed with the purple one, the green one, the cyan one, after a complete period from the fragmentation.

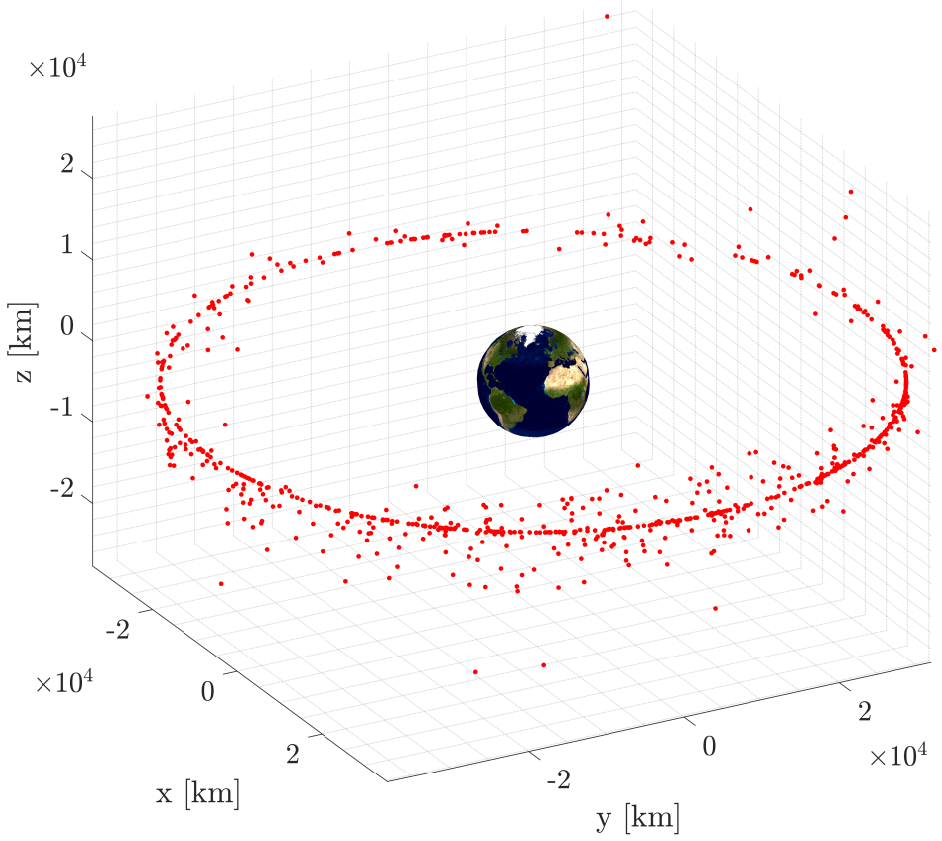

Figure 4.4: GEO satellites tracked on the Space-Track platform in the ECI reference frame, employed as uncorrelated objects to test the algorithm performance.

4.2. Nominal Performance Analysis

In this section, the nominal performance of the algorithms is investigated, testing their effectiveness and accuracy in an unperturbed scenario, without introducing errors on the parent state, on the fragmentation epoch or other disturbances that may affect the nominal code capability .

In this case, the analysis is conducted in LEO and GEO for both algorithms and the data sets used to test their functioning are the ones illustrated in the previous Sec. 4.1.

Moreover, to ensure a comprehensive and exhaustive survey of the results, some performance figures of merits are introduced for TITA and OPIA, and among the most important ones there is the percentage of fragments correctly correlate, as well as the percentage of uncorrelated objects excluded.

The primary objective of this section is to study the basic features of each code, explaining the outcomes and highlighting the principal source of failures. The comprehension of the process dynamics is fundamental to understand its behavior and predict its responses.

4.2.1. TITA Nominal Performance

Starting from the reference fragmentation scenarios described in Sec. 4.1, the algorithm is tested with the observations of both correlated and uncorrelated objects.

An important remark is that, before the test is performed, the values of the filtering thresholds are set through an initial tuning phase, performed for the main orbital regions under analysis (LEO and GEO), and resulting in the values shown in Tab. 4.3.

The results in LEO and GEO are reported separately for the sake of clarity, for an initial N_{grid} set to 1300 points.

LEO case

The standard performance of the TITA analysis is represented by the percentage of real fragments correlated, that will be classified as true positives, as well as the percentage of catalogued objects excluded, classified as true negatives. The closer these values are to 100% the better the results are, and the outcomes are illustrated in Tab. 4.4.

	LEO	GEO
ε_{cart} on position	191 km	637 km
ε_{α} on right ascension	8.31 deg	0.43 deg
ε_{δ} on declination	8.31 deg	0.0115 deg
ε_{ρ} on range	159 km	191 km
Δv_{max} on velocity	500 m/s	500 m/s

Table 4.3: TITA filtering thresholds derived from the tuning process in LEO and GEO.

True Positives	False Negatives	True Negatives	False Positives
89.03%	10.97%	100.00%	0.00%

Table 4.4: TITA nominal correlation performance in LEO.

Results show that 211 out of the 237 fragments generated by the simulation are correctly correlated to the event, while none of the nearly three thousand objects in the catalogue are associated. This demonstrates the excellent ability of the algorithm in excluding false correlations, while the linkage of some real fragments is inhibited by different factors to be investigated.

A first observation is that the performance of this algorithm is closely related to the geometric proximity of the propagated samples with the parent object at t_{blast}. To pass filters, samples must be close to the parent in both the Cartesian and the measurements spaces. This implies that the results are not only related to the Δv magnitude that each fragment experiences during the event but especially to the direction that this assumes, as this greatly affects the new orbit of the fragment and its geometric position in time. This can be noticed by looking at Fig. 4.5, where the correlation output, one if positive and zero if negative, is plotted as a function of the norm of the velocity change between the parent and the fragment under analysis. It is possible to observe that there is only a faint relationship between Δv magnitude and correlation since only a few fragments characterized by high velocity change are not associated.

Moreover, another important remark is that the number of samples that pass the filter is

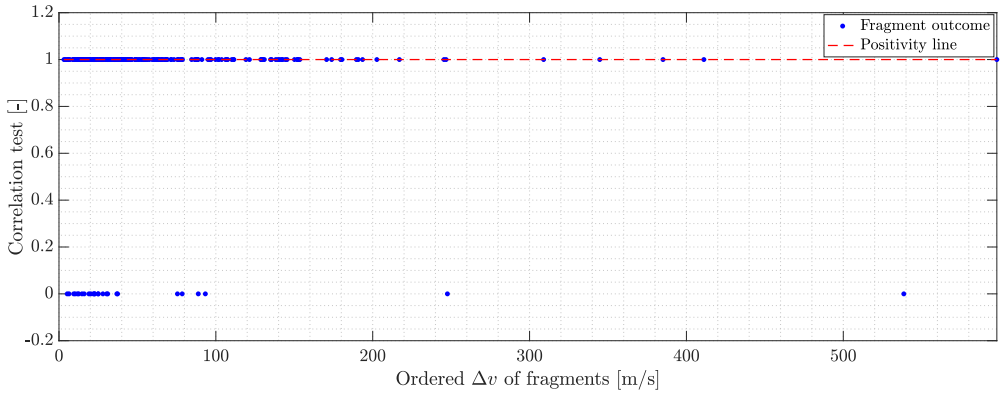

Figure 4.5: Correlation outcomes of real fragments in LEO, ordered with respect to Δv.

not a reliable indicator of filter accuracy, since not all samples of the admissible region are representative of the real state of the object. This makes more difficult to find a figure of merit that allows to clearly understand which elements affect the final result, as it will be investigated in the GEO case.

GEO case

The capability of the TITA analysis in the GEO region is presented in Tab. 4.5, where the results of the correlation process are collected in percent terms.

True Positives	False Negatives	True Negatives	False Positives
89.87%	10.13%	96.21%	3.79%

Table 4.5: TITA nominal correlation performance in GEO.

The correlation performance on true fragments is very similar to the LEO one, while some of the uncorrelated catalogued objects are associated to the fragmentation event. However, this was predictable by looking at the distribution of objects in GEO in Fig. 4.4. It can be seen that most of the catalogued elements have similar orbital characteristics in terms of inclination and eccentricity. This makes it more likely that, by propagating backward in time to the fragmentation epoch, the samples end up in a region of Cartesian space close to the location of the event.

Furthermore, in Fig. 4.6 it is possible to find confirmation of what was said previously

regarding the quality of the association and the number of samples that pass the filters. From the distribution of the fragments with respect to the semi-major axis and eccentricity it is immediately noticed that the ones having orbital parameters similar to the parent object are also the ones characterized by an almost uniform and limited number of samples passing the filters, without peaks or anomalies. This demonstrates that orbit similarity is fundamental to favor positive correlations, but a high number of samples does not necessarily represent an index of quality in the association process.

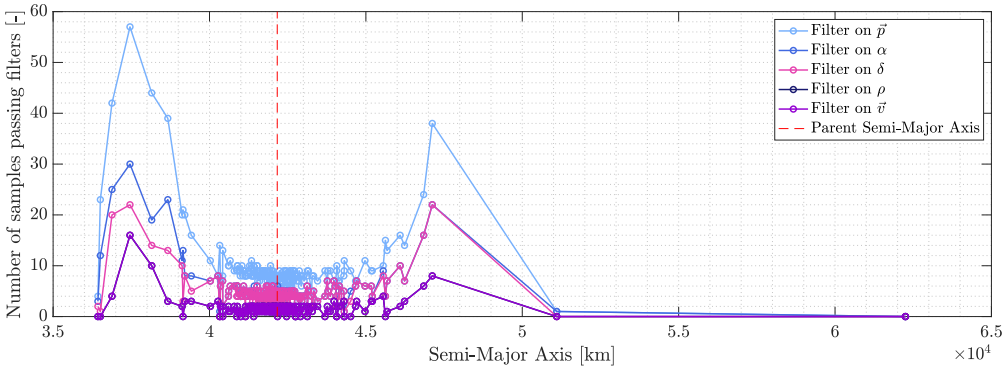

(a) Distribution with respect to the semi-major axis a.

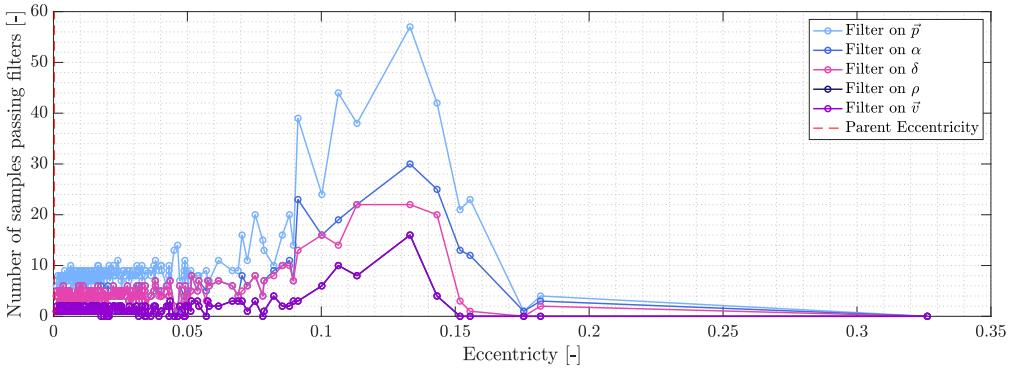

(b) Distribution with respect to the eccentricity e.

Figure 4.6: Number of samplings passing the filters for each of the true fragments in GEO.

However, in GEO it is easier to connect the magnitude of the velocity change to the expected outcomes. In fact, Fig. 4.7 shows that the fragments wrongly excluded from the correlation are generally those characterized by a higher velocity change, regardless of its direction. For this reason, the TITA algorithm performance is more predictable in GEO rather than in LEO, as here a high magnitude Δv can clearly represent the largest source of errors.

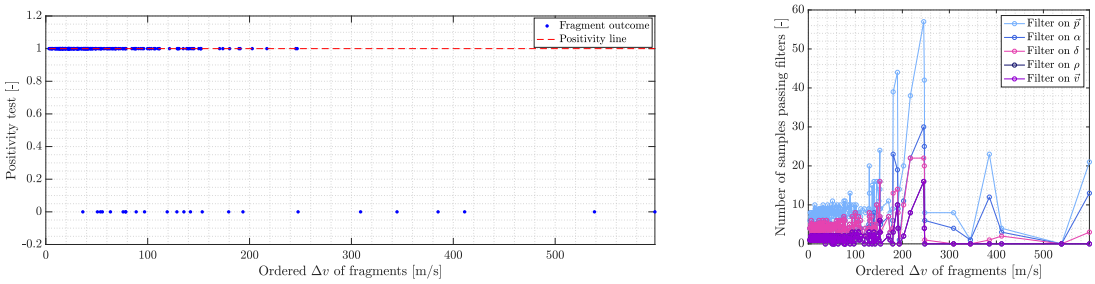

(a) Correlation outcomes.

(b) Distribution with respect to the velocity change Δv.

Figure 4.7: Correlation results dependency on velocity change Δv in GEO.

Finally, analyzing the few false correlations among the 798 catalogued elements, it is possible to observe that associations occur when the objects and the parent have very similar orbital parameters. In particular, the semi-major axis, represented in Fig. 4.8, has a notable influence on the correlation outcome.

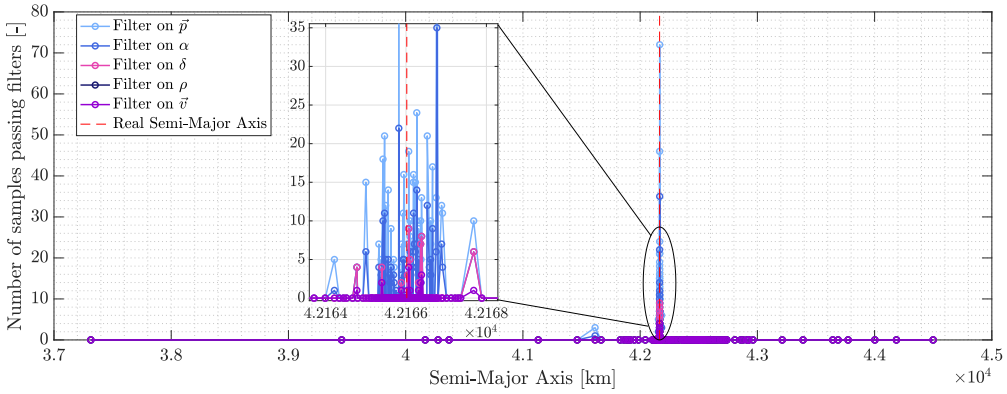

Figure 4.8: Number of sampling passing the filters for each of the catalogued objects in GEO, ordered with respect to the semi-major axis.

4.2.2. OPIA Nominal Performance

To ensure a fair comparison, OPIA is also tested in both LEO and GEO on the same fragmentation scenarios on which TITA was tested.

Here, no initial tuning phase is necessary and the presentation of the results can begin immediately. In this case, outcomes are obtained with a $N_{grid} = 500$ points, far less than the 1300 points used for TITA.

LEO case

OPIA immediately shows great accuracy and effectiveness in correlating objects in the LEO environment, as can be appreciated from Tab. 4.6.

True Positives	False Negatives	True Negatives	False Positives
99.16%	0.84%	100.00%	0.00%

Table 4.6: OPIA nominal correlation performance in LEO.

Now 235 out of 237 simulated fragments are correctly identified as involved in the event, while all the uncorrelated catalogued objects are filtered out. This allows to immediately understand the quality and superiority of the OPIA performance in this orbital region.
This algorithm is not influenced by the geometric proximity between samples and parent at the fragmentation epoch, while it is affected by the orbital similarity between fragments and parent, with particular regard on inclination and RAAN.
In this case, the correlation index introduced in Sec. 3.2 represents a satisfying performance metric, since the linkage process is founded on its value.
Starting from the distribution in Fig. 4.9 of the correlation coefficient with respect to the two orbital parameters mentioned earlier, it can be noticed that real fragments characterize a parabola shape, reproducing the quadratic behavior imposed by the χ^2-test and expressed in Eq. 4.1. Fragments with inclination and RAAN closer to the parent ones present a smaller correlation index, favoring the association process.

$$R = \left|\frac{D^2}{\chi^2}\right| = \frac{1}{\chi^2}(\boldsymbol{\mu}_{\mathrm{VD}} - \boldsymbol{\mu}_{\mathrm{VF}})^T \left(\boldsymbol{\Gamma}_{\mathrm{VD}} + \boldsymbol{\Gamma}_{\mathrm{VF}}\right)^{-1} (\boldsymbol{\mu}_{\mathrm{VD}} - \boldsymbol{\mu}_{\mathrm{VF}})$$
$$\boldsymbol{\mu}_{\mathrm{VD}} = \begin{Bmatrix} \mu_i \\ \mu_\Omega \end{Bmatrix}_{\mathrm{VD}} \qquad \boldsymbol{\mu}_{\mathrm{VF}} = \begin{Bmatrix} \mu_i \\ \mu_\Omega \end{Bmatrix}_{\mathrm{VF}} \tag{4.1}$$

In the previous section, it was shown that having an orbit close to the parent one helped the correlation with TITA, as it was more likely to get geometrically closer to the fragmentation event. Here, the orbital orientation similarity is even more important since the performance degrades quadratically when moving away from the inclination and RAAN of the parent object.

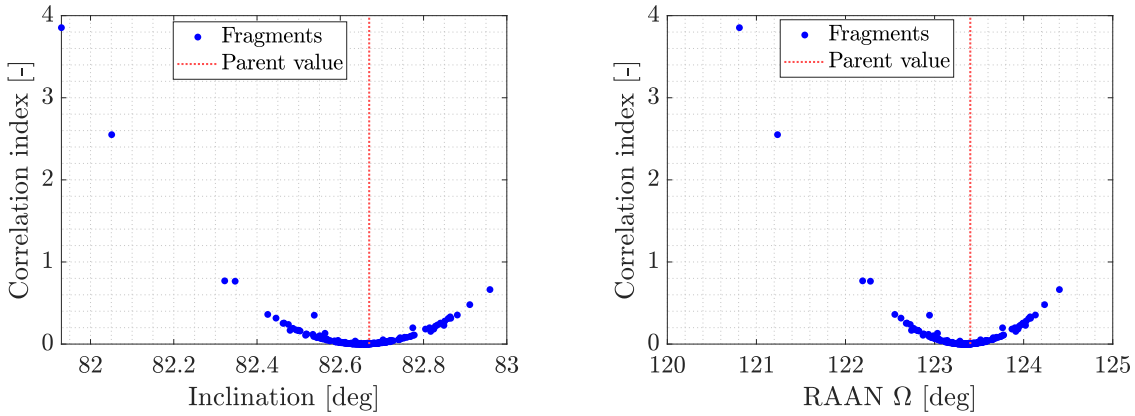

(a) Distribution with respect to the inclination i. (b) Distribution with respect to the RAAN Ω.

Figure 4.9: Correlation index distribution as a function of the real fragments orbital parameters.

Moreover, the relationship with the velocity change is also more immediate and legible: an increase in the Δv corresponds to a greater variation in the orbital parameters, making the association more difficult, as depicted in Fig. 4.10. In particular, as will be discussed later, a strong component in the normal direction of the Radial-Transversal-Normal (RTN) reference frame generates a relevant impact on the inclination of the orbit, deteriorating the correlation index.

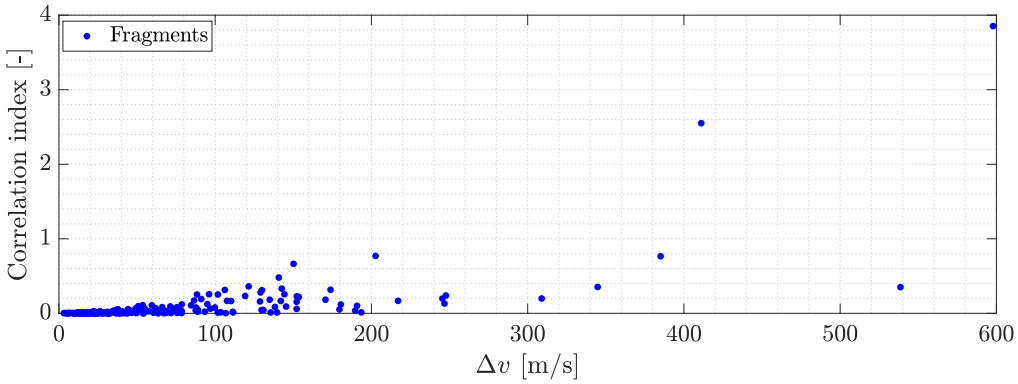

Figure 4.10: Correlation index distribution as a function of the velocity change between real fragments and parent object.

Finally, it is also possible to analyze the results obtained with the uncorrelated catalogued objects, where the parabola shape of the correlation coefficients distribution is still observable, shown in Fig. 4.11 for the RAAN. Some of these values follow the quadratic

profile, while others are scattered due to closeness in terms of RAAN, but not in terms of inclination.

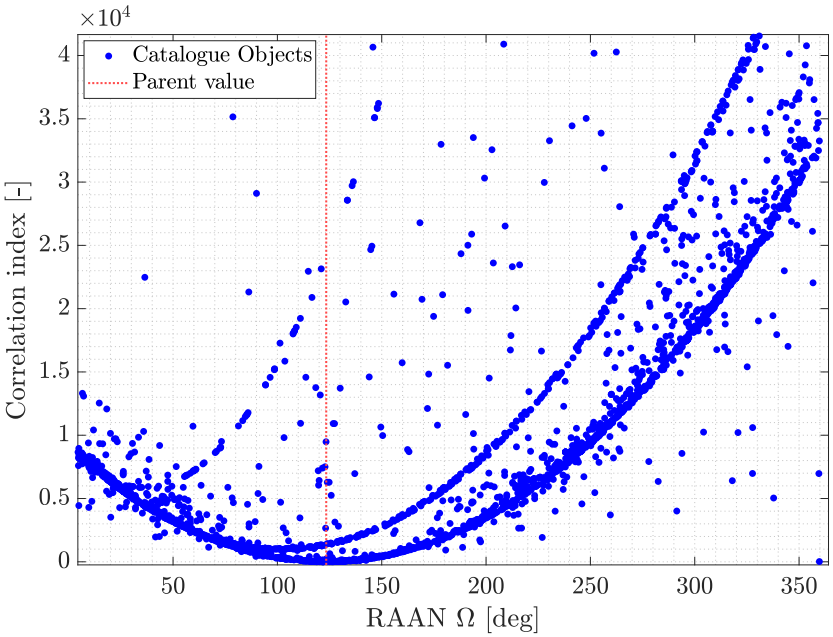

Figure 4.11: Correlation index distribution as a function of the RAAN of the uncorrelated catalogued objects in LEO.

From this, it is clear that OPIA is characterized by a regular and predictable behavior, with efficient performance metrics to be studied in order to understand the dynamics of the code.

GEO case

From the OPIA performance reported in Tab. 4.7 it is clear that in GEO the code loses its ability to exclude false positives.

The tendency to correlate is increased, but this leads not only to an increase in the association of real fragments but also of uncorrelated objects, losing the algorithm usefulness by associating a large number of elements not involved in the fragmentation.

True Positives	False Negatives	True Negatives	False Positives
99.58%	0.42%	42.35%	57.65%

Table 4.7: OPIA nominal correlation performance in GEO.

This is mainly devoted to the orbital similarity of objects in the GEO region: many of the RSOs represented in Fig. 4.4 are characterized by similar inclination, sharing the orbital plane. This makes it particularly difficult to avoid false associations due to the sensitivity of the code to orbital parameters, with a focus on inclination and RAAN.
Furthermore, another remark is that in GEO the hypothesis of Gaussian (or normal) distribution of the fragments on the (i, Ω)-plane is not entirely valid, as there are values that modify the shape of the distribution compared to the LEO case showed in Sec. 3.2. In Fig. 4.12 it is possible to observe that some fragments present a rapid increase in inclination: this is mainly due to an intense component of Δv in the direction normal to the orbital plane, which is proportionally more effective with respect to the LEO case, given the lower velocities in GEO. This phenomenon prevents the covariance that describes the uncertainty of the distribution from being correctly modeled, making the correlation process less accurate.

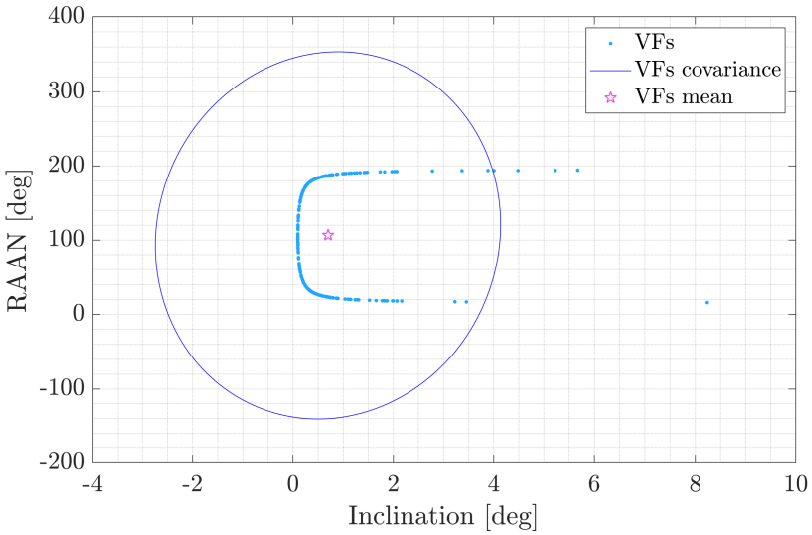

Figure 4.12: Real fragments distribution on (i, Ω)-plane in the GEO region.

Moreover, the strict connection between the normal component of the Δv in the RTN reference frame and the correlation performance is presented in Fig. 4.13. This results in an unreliable behavior of OPIA in GEO, as can be appreciated from the graph in Fig. 4.14: the distribution of true fragments correlation indices with respect to the RAAN loses its parabolic shape, indicating that the covariances involved in the χ^2-test have partly lost

their accuracy and effectiveness in describing uncertainty.

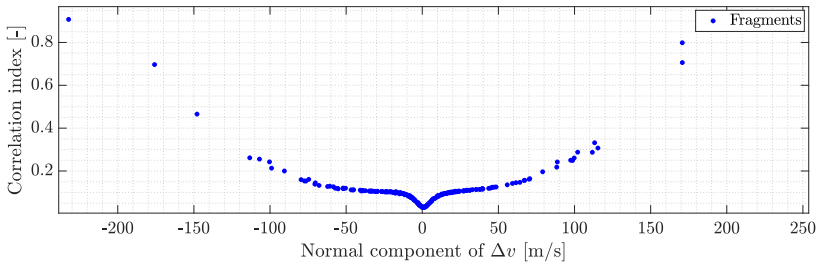

Figure 4.13: Correlation index distribution as a function of the normal component of the Δv in the RTN reference frame.

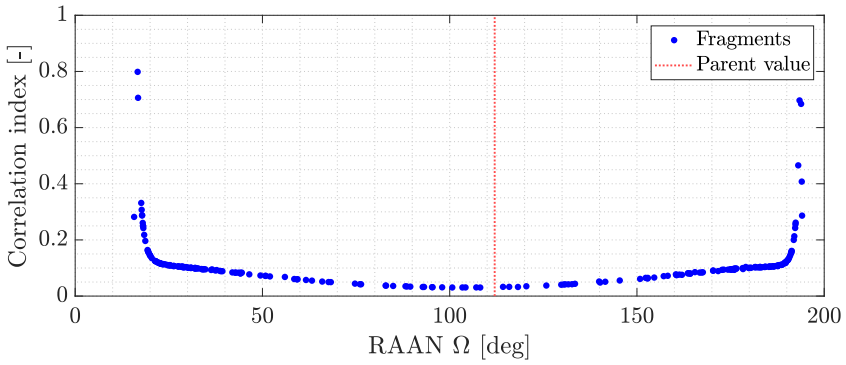

Figure 4.14: Correlation index distribution as a function of the RAAN of the real fragments in GEO.

4.3. Sensitivity Analysis

This section is dedicated to the comprehensive examination of the robustness of the developed algorithms through a rigorous sensitivity analysis, entailing a systematic evaluation of their performance under various perturbations and environmental conditions.
The tests presented herein are designed to emulate the real-world challenges that these processes may encounter, with the final aim of highlighting which elements negatively affect the results. The TITA and OPIA ability to adapt and maintain accuracy is analyzed, with the methodical exploration of these factors:

- **Measurements noise**: noises on optical measurements can introduce a modeling fallacy in the optical admissible region.

- **Error on parent position**: a wrong evaluation of the parent position at the fragmentation epoch can represent an additional source of mismatching between observed fragments and the parent object.
- **Error on fragmentation epoch**: an error on the time of fragmentation can negatively affect the correlation process, especially for algorithms that perform propagation from or to that date.
- **Number of points in the sampling grid**: the smaller the number of samples used, the shorter the computational time is, but also the less accurate the admissible region representation is.
- **Orbital perturbations**: a non-Keplerian propagation introduces short and long terms effects on objects orbital parameters.

The sensitivity analysis to these factors will serve as a validation step to study the algorithm ability to deliver precise and reliable results in a real context.
Given the results obtained in the previous section, this analysis will only be performed in LEO for OPIA and in GEO for TITA, i.e. where they respectively demonstrate a promising performance. This is also done to avoid an unnecessarily long and complex discussion, avoiding analyzing the robustness of the code where it is not performing.

4.3.1. Sensitivity to measurements noise

Optical measurements play a fundamental role in both algorithms, as the construction of the admissible region is based on the optical attributable $\mathcal{A}_{opt} = (\alpha, \delta, \dot{\alpha}, \dot{\delta})$, found as discussed in Sec. 2.2.
No factor relating to measurements quality was introduced in the study of standard performance. Therefore, the objective is to simulate the degradation of the measurements, modeling the errors as Gaussian distributions whose standard deviations are presented in Tab. 4.8, taken from typical accuracy values of optical surveys.

In this way, the noise covariance matrix R is obtained, and a random Gaussian error with zero mean and R covariance is added to the attributable to emulate the observation

Standard deviation on angles σ_{ang}	Standard deviation on angle rates $\sigma_{ang-rate}$
4 arcsec	5 arcsec/h

Table 4.8: Standard deviations introduced on angles and angle rates. Credits [57]

deterioration, as done in Eq. 4.2.

$$\mathcal{A}_{opt}^{noise} = \mathcal{A}_{opt} + \text{mvnrnd}(0, R), \quad \text{where} \quad R = \begin{bmatrix} \sigma_{ang}^2 & 0 & 0 & 0 \\ 0 & \sigma_{ang}^2 & 0 & 0 \\ 0 & 0 & \sigma_{ang-rate}^2 & 0 \\ 0 & 0 & 0 & \sigma_{ang-rate}^2 \end{bmatrix} \tag{4.2}$$

OPIA results in LEO

The OPIA performance under conditions of disturbed optical measurements is presented in Tab. 4.9 together with the nominal performance obtained in LEO, in order to have an effective feedback by comparing the results and verifying the eventual extent of degradation.

	True Positives	False Negatives	True Negatives	False Positives
Nominal	99.16%	0.84%	100.00%	0.00%
Perturbed	99.16%	0.84%	100.00%	0.00%

Table 4.9: OPIA correlation performance affected by measurements noise.

In this case, OPIA shows great robustness concerning optical measurements noise. The admissible region characterization is influenced by this error, but the effect on the samples orbital parameters, in particular inclination and RAAN, is too low to be sensed on the algorithm output.

No performance deterioration can be appreciated and this demonstrates a very low sensitivity of the code to measurement inaccuracies.

TITA results in GEO

The application of the measurements noise in the GEO region leads to the TITA performance reported in Tab. 4.10, accompanied also in this case by the nominal performance to ensure a yardstick.

	True Positives	False Negatives	True Negatives	False Positives
Nominal	89.87%	10.13%	96.21%	3.79%
Perturbed	88.19%	11.81%	96.21%	3.79%

Table 4.10: TITA correlation performance affected by measurements noise.

The comparison between outcomes shows a slight deterioration of the code performance in the correlation of real fragments, while the association of uncorrelated objects from the catalogue remains unchanged. The original correlation result is good, although not excellent, and remains good even after introducing measurements inaccuracies.
However, the code demonstrates a slight sensitivity to this noise because the samples of the admissible region, affected by the measurement error, are used for the propagation up to the fragmentation epoch. This makes this factor slightly more impactful for TITA than it was for OPIA.

4.3.2. Sensitivity to error on parent position

To replicate the complexity and difficulty of the correlation process in a real-world context, an error is added to the final state of the parent object at the fragmentation epoch. The covariance, which can be associated with the last available ephemeris, grows during propagation in the absence of observations up to the time of the event. For this reason, in a real condition, the state must be characterized by a factor of uncertainty at the moment of the fragmentation.
In particular, noise is added on the parent position in the RTN reference frame, found from the parent ECI Cartesian state $\mathbf{x}^{blast} = \{\mathbf{p}^{blast}, \mathbf{v}^{blast}\}$ as in Eq. 4.3. The RTN reference frame, with the origin at the center of mass of the chief, is ideal for this kind of analysis as it is characterized by a clearer and more direct relationship between the error in a specific direction and the resulting orbital modification [58].

$$\hat{\mathbf{e}}_r^{RTN} = \frac{\mathbf{p}^{blast}}{||\mathbf{p}^{blast}||}, \qquad \hat{\mathbf{e}}_n^{RTN} = \frac{\mathbf{p}^{blast} \times \mathbf{v}^{blast}}{||\mathbf{p}^{blast} \times \mathbf{v}^{blast}||}, \qquad \hat{\mathbf{e}}_t^{RTN} = \hat{\mathbf{e}}_n^{RTN} \times \hat{\mathbf{e}}_r^{RTN} \tag{4.3}$$

From this, it is straightforward to characterize the rotation matrix from the ECI reference frame and vice-versa:

$$R_{ECI2RTN} = \begin{bmatrix} | & | & | \\ \hat{\mathbf{e}}_r^{RTN} & \hat{\mathbf{e}}_t^{RTN} & \hat{\mathbf{e}}_n^{RTN} \\ | & | & | \end{bmatrix} \qquad R_{RTN2ECI} = R_{ECI2RTN}^T \tag{4.4}$$

Once again, errors are modeled as Gaussian distribution whose standard deviation values are reported in Tab. 4.11, with reference to the cases analyzed in [59].

$\sigma_{r,n}$ **on radial and normal direction**	σ_t **on transversal direction**
0.08 km	40.0 km

Table 4.11: Standard deviations introduced in the radial, transversal, and normal direction of the RTN reference frame. Credits [59]

Finally, as done in Sec. 4.3.1, the covariance matrix R is constructed, and a random Gaussian error with zero mean is introduced on the parent position at the fragmentation epoch, exploiting the rotation matrix $R_{RTN2ECI}$ to convert the error from RTN to ECI reference frames. The position of the parent therefore changes from fragment to fragment, adding a different noise in each case.

$$\mathbf{p}_{noise}^{blast} = \mathbf{p}^{blast} + R_{RTN2ECI} \cdot \text{mvnrnd}(0, R), \quad \text{where} \quad R = \begin{bmatrix} \sigma_r^2 & 0 & 0 \\ 0 & \sigma_t^2 & 0 \\ 0 & 0 & \sigma_n^2 \end{bmatrix} \tag{4.5}$$

OPIA results in LEO

By introducing position inaccuracy on the parent state at the fragmentation epoch, OPIA generates the results collected in Tab. 4.12.

	True Positives	False Negatives	True Negatives	False Positives
Nominal	99.16%	0.84%	100.00%	0.00%
Perturbed	97.47%	2.53%	100.00%	0.00%

Table 4.12: OPIA correlation performance affected by error on parent position.

The noise, added as described in the previous section, affects the outcomes with a slight decrease in the performance. This time, 6 out of 237 real fragments are erroneously excluded from the correlation, demonstrating minimal, but not irrelevant, sensitivity to this disturbance.

Changing the parent position means changing the initial base on which simulating the fragmentation scenario with the NASA Standard Breakup Model, thus impacting the distribution of fragments on the (i, Ω)-plane. This can slightly decrease the VFs mean $\boldsymbol{\mu}_{VF}$ and covariance $\boldsymbol{\Gamma}_{VF}$ accuracy, resulting in a less effective correlation process.

The normal component of Δv still represents the main source of error for OPIA, which shows a quite robust behavior concerning this noise: Fig. 4.15 demonstrates that the distribution of correlation coefficients preserves the parabolic shape imposed by the χ^2-test, even if characterized by more outliers values if compared with Fig. 4.9.

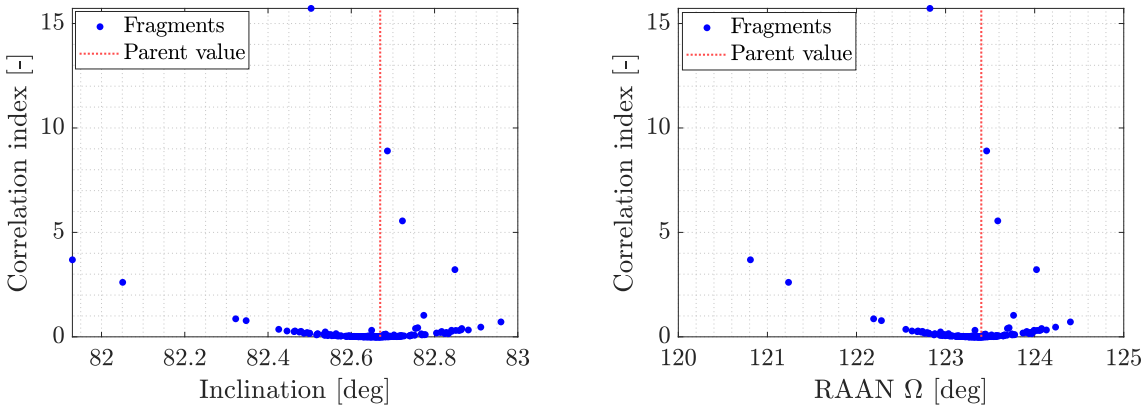

(a) Distribution with respect to the inclination i. (b) Distribution with respect to the RAAN Ω.

Figure 4.15: Correlation index distribution as a function of the real fragments orbital parameters, adding an error on the parent position.

TITA results in GEO

The influence of the error on the parent position on TITA is expressed in Tab. 4.13, where the actual code performance is compared to the nominal one.

	True Positives	False Negatives	True Negatives	False Positives
Nominal	89.87%	10.13%	96.21%	3.79%
Perturbed	88.19%	11.81%	96.21%	3.79%

Table 4.13: TITA correlation performance affected by error on the parent position.

TITA bases its correlation analysis on filtering out samples that are not geometrically close to the position of the parent object, so it is natural to assume that such an error would greatly affect the results. However, this noise can still be absorbed with an appropriate setting of the filters, avoiding too stringent values.
From Tab. 4.13, a limited degradation in the quality of the results can be appreciated, with a slight decrease in the percentage of true positives. Both perturbed and nominal conditions offer good, even if not excellent, results that overall prove TITA robust to this noise. Moreover, the ability of the code to exclude false positives remains unchanged.

4.3.3. Sensitivity to error on fragmentation epoch

Another important element to be considered when modeling the real-world challenges is the uncertainty on the fragmentation epoch. As introduced in Sec. 1.6, different procedures exist to characterize the fragmentation, requiring the availability of different quantities, and some of them are more accurate than others.
However, a certain degree of error is always expected, and it is interesting to study what happens to the performance of the code when introducing the delays presented in Tab. 4.14.

	Time delay value	Units
First delay	2.5	min
Second delay	5	min

Table 4.14: Delay values introduced in the sensitivity tests.

It is important to note that this delay regards only the fragmentation epoch on which performing the correlation analysis, while the fragments simulated to characterize the performance are generated at the true fragmentation date.

OPIA results in LEO

When the fragmentation epoch is characterized by a time delay, OPIA propagates the parent state up to a date that does not correspond to that of the event. The NASA Standard Breakup Model, as in the case of the error on the parent position, is applied in the wrong place, making the distribution of the fragments on the (i, Ω)-plane less accurate. Here, the error is even larger, as the delayed propagation of the parent leads to a much larger error on the final position than the one introduced in Sec. 4.3.2.
The influence on the OPIA performance of the time delays presented in Tab. 4.14 is here illustrated:

	True Positives	False Negatives	True Negatives	False Positives
Nominal	99.16%	0.84%	100.00%	0.00%
2.5 min delay	97.05%	2.95%	100.00%	0.00%
5 min delay	95.36%	4.64%	100.00%	0.00%

Table 4.15: OPIA correlation performance affected by delays on the fragmentation epoch.

It is possible to notice a gradual degradation in the quality of the results, up to 11 out of 237 real fragments excluded from the correlation in the worst-case scenario. The imprecision on the fragmentation point is significant, but even in this case the algorithm demonstrates satisfactory robustness to noises and errors.
Although the position of the parent is characterized by a large inaccuracy, OPIA is not based on the Cartesian proximity of the parent with the observed fragments, but rather on proximity in terms of orbital parameters, which are less sensitive to time delays in the propagation.
A strong Δv remains the principal source of errors, with particular focus on its normal component in the RTN reference system. However, it is interesting to analyze how this dependence changes compared to the unperturbed case. In Fig. 4.16 it is shown that, in the no-delay case, the relationship between the correlation index and velocity change in

the normal direction reproduces the quadratic shape of the χ^2-test, while many outliers values appears when introducing a delay.

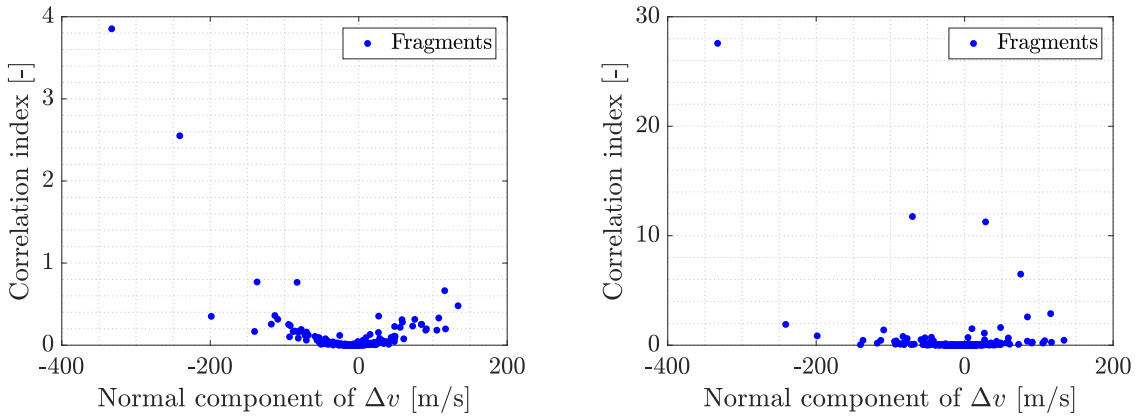

(a) Case without delay.

(b) Case with 5 min delay.

Figure 4.16: Correlation index as a function of the normal component of Δv in the RTN reference frame.

TITA results in GEO

Introducing a delay in the estimated fragmentation epoch means introducing an error in the orbital position at which the fragmentation is identified. This can lead to a great impact on the performance of TITA, whose correlation process is based on proximity between parents and fragments in the Cartesian and measurements spaces.
The impact on TITA results is displayed in Tab 4.16, where the outcomes are gathered and subdivided with respect to the time delays modeled.

	True Positives	False Negatives	True Negatives	False Positives
Nominal	89.87%	10.13%	96.21%	3.79%
2.5 min delay	78.90%	21.10%	97.35%	2.65%
5 min delay	55.69%	44.31%	96.21%	3.79%

Table 4.16: TITA correlation performance affected by delays on the fragmentation epoch.

As expected, the algorithm sensitivity to this factor is strong, resulting in a rapid loss of performance even introducing only 2.5 minutes of delay. The reasons lie in the inconsistency in terms of positions between parent and fragments at the biased fragmentation

epoch.

In particular, by analyzing the behavior of the filtered samples for the tested fragments, it is possible to notice a strong reduction in the effectiveness of the filter on the declination δ, which excludes an important quantity of real fragments associated with the event. Even if the number of samples passing the filter does not represent a quality metric for the algorithm, from Fig. 4.17 it is possible to spot the visible reduction of samples in the 5 minute delay case, increasing the correlation false negatives. Here, the distribution of filtered samples is plotted as a function of the known velocity change between the real fragments and the parent object.

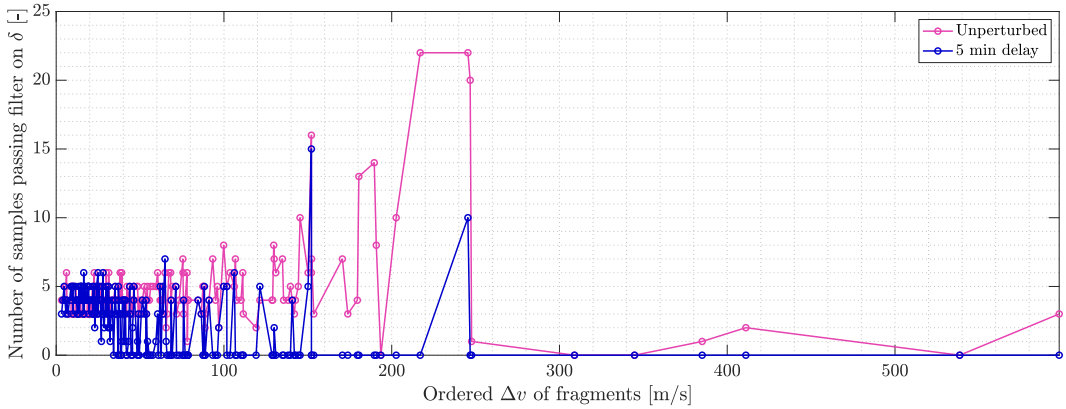

Figure 4.17: Distribution of samples filtered on declination δ as a function of the Δv.

A final remark can be made on the excluding performance of uncorrelated catalogued objects. Also in this case, introducing a delay does not cause any effect on the number of false positives, since in the time window investigated with the time delays only a few new objects come within the vicinity of the parent satellite.

4.3.4. Sensitivity to number of points in the sampling grid

The number of points N_{grid} is defined as the number of non-equally spaced elements for each side of the sampling grid, generating N_{grid}^2 samples that make N_{grid} an indicator of the density of the specimen. It is a fundamental element for both OPIA and TITA algorithms because it influences the sampling time of the admissible region, which occupies a significant part of the total Central Processing Unit (CPU) time.

Focusing on TITA, N_{grid} determines the number of samples to be propagated and tested,

impacting even more the total computational cost. Furthermore, the outcomes of the TITA analysis are also influenced by the number of samples that find themselves in proximity to the fragmentation event.
For these reasons, it is extremely interesting to study how OPIA and TITA performances are influenced by the different N_{grid} presented in Tab. 4.17.

	N_{grid1}	N_{grid2}	N_{grid3}
Number of points [-]	200	500	1300

Table 4.17: N_{grid} values on which sensitivity analysis is performed.

Recalling what was said in Sec. 4.2, the nominal performance was obtained with $N_{grid} = 500$ for OPIA, while $N_{grid} = 1300$ was chosen for TITA after the tuning phase.

OPIA results in LEO

The sensitivity of the OPIA algorithm to N_{grid} is represented by the performance metrics collected in the following Tab. 4.18, highlighting the N_{grid} used for the nominal condition. The total computational time taken to test the correlation of a single optical observation is also reported in each of the cases investigated, to introduce a performance analysis of the code from the CPU efficiency viewpoint.

N_{grid}	True Positives	False Negatives	True Negatives	False Positives	CPU time
200	99.16%	0.84%	100.00%	0.00%	$\sim$ 4.5 s
500	99.16%	0.84%	100.00%	0.00%	$\sim$ 10.5 s
1300	99.16%	0.84%	100.00%	0.00%	$\sim$ 53.5 s

Table 4.18: OPIA correlation performance with different N_{grid} values. The technical specifics of the CPU processor are illustrated in Sec. 2.4.

From Tab. 4.18, it is immediately clear that OPIA is not influenced by N_{grid}, as the results do not change when its value changes. The reason is connected to the fact that here the samples are used only to dictate the shape of the admissible region in the (i, Ω)-plane. To do this, a sufficient number of points is needed to define the covariance of the distribution with good accuracy, but this is the only requirement that can be imposed on N_{grid}.
Therefore, the code is characterized by great robustness concerning this factor, which

allows for a significant reduction in the computational time without sacrificing accuracy and effectiveness. To understand the great computational efficiency, testing 237 real fragments with $N_{grid} = 200$ requires a CPU time of approximately 18 minutes, while for $N_{grid} = 1300$ it takes up to 4 hours.

TITA results in GEO

In TITA, samples do not only define the shape of the admissible region projected into the (i, Ω)-plane, but their number and their density are fundamental to get close to the actual value of the fragment range and range rate among all the admissible values in the region, with the objective of matching the parent object position after the propagation. Samples are filtered based on their proximity in the Cartesian and the measurements spaces, but their propagation tends to disperse them, especially over long periods.
Given these premises, the results of TITA when N_{grid} varies are shown in Tab. 4.19, with the value used for the nominal performance highlighted once again.

N_{grid}	True Positives	False Negatives	True Negatives	False Positives	CPU time
200	2.53%	97.47%	99.62%	0.38%	$\sim$ 11 s
500	18.57%	81.43%	99.24%	0.76%	$\sim$ 16.5 s
1300	89.87%	10.13%	96.21%	3.79%	$\sim$ 55 s

Table 4.19: TITA correlation performance with different N_{grid} values. The technical specifics of the CPU processor are illustrated in Sec. 2.4.

As anticipated, the impact of N_{grid} is strong in TITA, which shows great sensitivity to the density of the sampling grid. With a lower value of N_{grid}, the code loses its correlation capacity, especially if the interval between event and observation is large.
This results in a drastic deterioration in performance, already starting from $N_{grid} = 500$, which can also be traced from the graph of the distribution of filtered samples as a function of semi-major axis and eccentricity in Fig. 4.18, comparable with the equivalent Fig. 4.6 in the nominal case.

For this reason, N_{grid} must be kept high to maintain the accuracy and effectiveness of the algorithm, at the expense of a significantly higher computational cost.

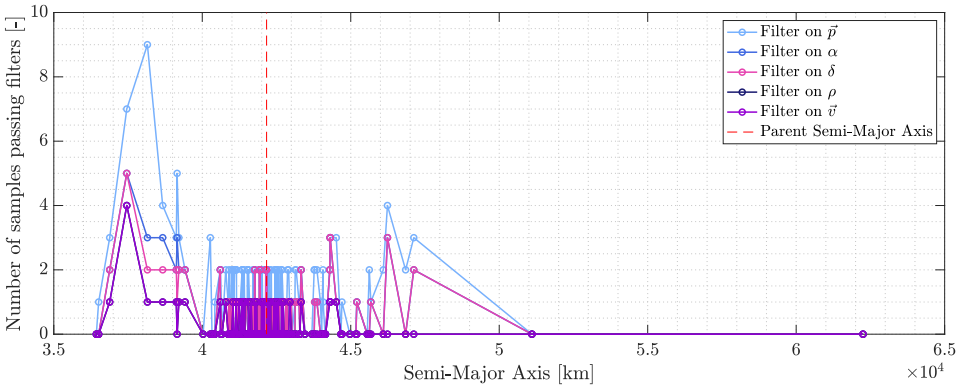

(a) Distribution with respect to the semi-major axis a.

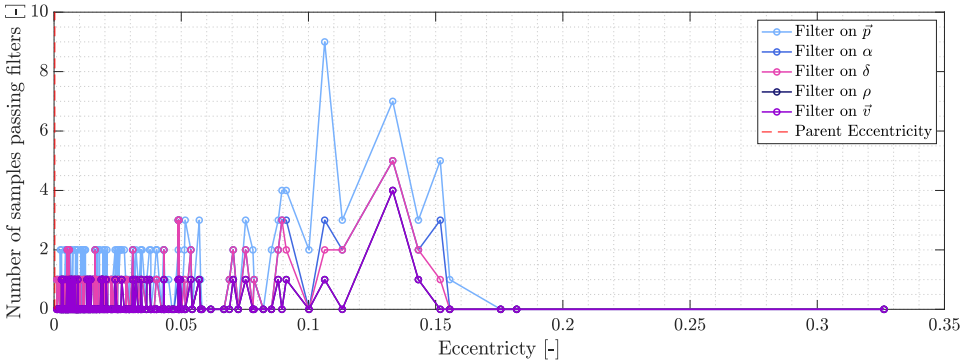

(b) Distribution with respect to the eccentricity e.

Figure 4.18: Number of samplings passing the filters for each of the true fragments in GEO, setting $N_{grid} = 500$.

4.3.5. Sensitivity to orbital perturbations

The final sensitivity analysis regards the introduction of orbital perturbations in the propagation process: SGP4 is employed both to compute the testing fragments trajectory (the ground-truth) and to propagate samples in the algorithm process. Some of the perturbing acceleration contributions described in Sec. 2.1.2 are now modeled to derive a more realistic motion in the Near-Earth environment.

However, only the TITA algorithm performs samples orbital computation, while OPIA can compare quantities at different times without propagating. For this reason, only the sensitivity of TITA is tested, since it is already assessed that OPIA cannot be influenced by this factor.

Furthermore, the computational impact of introducing the SGP4 analytical propagator is investigated, compared to the one related to the nominal Keplerian propagation.

TITA results in GEO

In the nominal case, Keplerian propagation was used both to generate the ground-truth of the fragments trajectory and for the samples within the process. Changing the type of propagator does not imply a real gain or loss of accuracy, as represented in Tab. 4.20.

Prop.	True Positives	False Negatives	True Negatives	False Positives	CPU time
Kepl.	89.87%	10.13%	96.21%	3.79%	$\sim$ 55 s
SGP4	89.03%	10.97%	96.97%	3.03%	$\sim$ 260 s

Table 4.20: TITA correlation performance under the influence of orbital perturbations.

The time increment is strong and would seem unjustified since it does not correspond to greater accuracy. However, this is due to the synthetic working environment in which the simulations are operated, thanks to which the consistency between propagators is maintained. In reality, fragments are subjected to a series of orbital perturbations which continuously modify their orbits. These contributions need to be modeled by a non-Keplerian propagator, such as SGP4, to increase the accuracy of the reconstruction.
To reproduce the effect of an inaccurate propagator, the orbit propagation of test fragments and samples is decoupled, using SGP4 for the former and an analytical Keplerian propagator for the latter. The results are shown in Tab. 4.21:

Prop.	True Positives	False Negatives
Mixed	88.61%	11.39%

Table 4.21: TITA correlation performance under the influence of orbital perturbations using mixed propagators: SGP4 for the data set generation and Keplerian for the algorithm process.

The analysis is carried out only on correlated simulated fragments and not on catalogued objects. As expected, results show a slight decrease in performance in terms of association compared to the original case, where Keplerian propagation was used both to compute the ground-truth and inside the algorithm. This loss will amplify for longer propagation arcs, as the effect of propagator inaccuracy will be more relevant, thus imposing a trade-off between precision and computational cost.

5 | Conclusions and future developments

The admissible region tool represents one of the most promising concepts for handling very short observational arcs, where the classical methods for initial orbit determination fail. This allows to introduce innovative key features in algorithms dedicated to the correlation of observations to a certain fragmentation event, thus improving the precision and efficiency of space debris tracking and characterization, even when very little information is available. The most innovative aspect lies precisely in the association process, where the correlation can be verified without having to determine the orbit of the fragment.

In this thesis, two correlation algorithms were developed, resulting in two codes that together ensure satisfactory performance both in LEO and GEO. TITA and OPIA base their track-to-fragmentation process on the admissible region formulation, as described in Chapter 3, even if two procedures with very different characteristics derive from it.

OPIA, founded on the similarity of orbital parameters, guarantees excellent accuracy in LEO but completely loses its functionality in GEO due to the closeness in inclination and RAAN of the objects populating this region.

On the other hand, TITA is based on the geometrical proximity between the fragment samples and the parent object both in the Cartesian and measurements spaces, offering a good, but not optimal, performance in LEO and GEO. In particular, in LEO region it is less performing than OPIA. On the contrary, TITA is more performing in GEO, and, for this reason, it is considered as a complementary algorithm to OPIA.

It is worth to remark that the TITA approach is made more complicated by the setting of the filters in the tuning phase: this is done once for each orbital region under analysis, taking into consideration simulations of already known fragmentation events and defining

the thresholds so that the algorithm can include correlated fragments, excluding false positives.

The work done in this thesis makes a detailed analysis of the characteristics and innovative aspects of these two algorithms, highlighted more clearly by the direct comparison in Tab. 5.1. Here, it is possible to notice that, where OPIA works, it provides unparalleled performance, robustness, and computational efficiency. However, it suffers the comparison in GEO with TITA, where the latter remains the only code capable of performing.

	OPIA	**TITA**
Operates without performing IOD	✓	✓
Works in LEO	✓	✓
Works in GEO	×	✓
Does not require a tuning phase	✓	×
Shows clear performance metrics	✓	×
Low sensitivity to measurements noise	✓	✓
Low sensitivity to error on parent position	✓	✓
Low sensitivity to error on fragmentation epoch	✓	×
Low sensitivity to N_{grid}	✓	×
High computational efficiency	✓	×
Proven functioning in an operational scenario	✓	✓

Table 5.1: Summary comparison of OPIA and TITA performances and characteristics.

Moreover, as introduced in Sec. 3.2, OPIA has demonstrated encouraging results in LEO even when employed without the knowledge of the fragmentation epoch. It means that it would potentially be possible to associate the observation of a fragment with the parent object without having first characterized the event, allowing streamlined and rapid operations without waiting for the time occupied by all the fragmentation reconstruction procedures. This demonstrates the great effectiveness and reliability of OPIA, together with its truly promising potential in the study of fragmentation phenomena.

Possible future development paths may focus on analyzing the OPIA performance into the GEO region, investigating the possibility to exploit a convenient orbital state representation, such as that of Delaunay [25]. Even a more coherent statistical approach can be characterized, introducing uncertainties related to the measurements into the process as well as a non-Gaussian metric, and implementing a Monte Carlo analysis on both the admissible region and the parent object, to then compare the statistical distance between the two distributions obtained.

Furthermore, the operations of TITA and OPIA can be extended to the radar case, adapting the procedures to the radar admissible region characteristics.

However, the potential of these algorithms could lead to developments far beyond the simple fragment-event association: with a time-variant analysis, it would be interesting to investigate if these tools can prove to be a basis for algorithms dedicated to the characterization of fragmentation events, starting from a single fragment observation and without IOD results.

Finally, after some tests, it is clear that these processes present a propensity to work in the track-to-track correlation field, where they may be employed to associate two or more very short arcs even in presence of maneuvers, determining the orbit of an object and enhancing the cataloguing process.

Bibliography

[1] M. Romano, A. Muciaccia, M. Trisolini, P. Di Lizia, C. Colombo, A. Di Cecco, and L. Salotti. Puzzle software for the characterization of in-orbit fragmentations. *8th European Conference on Space Debris*, 2021.

[2] European Space Agency (ESA). *Space debris by the numbers*. ESA, 2017.

[3] N.L. Johnsin, E. Stansbery, D.O. Withlock, and et al. History of on orbit satellite fragmentation. *Advances in the Astronautical Sciences 14th Edition*, 2008.

[4] C. Pardini and L. Anselmo. Review of past on-orbit collisions among catalogued objects and examination of the catastrophic fragmentation concept. *Acta Astronautica*, 100, 2014. doi:10.1016/j.actaastro.2014.03.013.

[5] Space Debris User Portal, 2023. URL `https://sdup.esoc.esa.int/discosweb/statistics/`.

[6] D.J. Kessler and B.G. Cour-Palais. Collision frequency of artificial satellites: The creation of a debris belt. *Journal of of Geophysical Research*, 38, 1978. doi:10.1029/JA083iA06p02637.

[7] M.F. Montaruli. *Multireciever radar technologies for Space Surveillance and Tracking*. PhD thesis, Politecnico di Milano, Via Privata Giuseppe La Masa, 34/B12, 2023.

[8] ESA Space Debris Office. *ESA's Annual Space Environment Report*. 2023.

[9] Universe Today, 2020. URL `https://www.universetoday.com/148766`.

[10] P. Faucher, R. Peldszus, and A. Gravier. Operational space surveillance and tracking in europe. *Journal of Space Safety Engineering*, 7, 2020. doi:10.1016/j.jsse.2020.07.005.

[11] J.A. Kennewell and B.N. Vo. An overview of space situational awareness. *16th International Conference on Information Fusion*, 2013.

[12] P. Faucher and R. Peldszus. European Union Space Surveillance Tracking (EU SST): State of Play and Perspectives. *Space Policy*, 62, 2022. doi:10.1016/j.spacepol.2022.101503.

[13] EU Space Surveillance and Tracking: About Us, 2023. URL `https://www.eusst.eu/about-us/`.

[14] EU Space Surveillance and Tracking: Services, 2023. URL `https://www.eusst.eu/services/`.

[15] R. Cipollone, M.F. Montaruli, N. Faraco, P. Di Lizia, and M. Massari et al. A reentry analysis software module for space surveillance and tracking operations. *73rd International Astronautical Congress (IAC)*, 2022.

[16] P.Y. Bely. *The Design and Construction of Large Optical Telescopes*. Springer New York, NY, 2003. ISBN 978-0-387-22606-4.

[17] S. Esposito, A. Riccardi, E. Pinna, A. Puglisi, F. Quirós-Pacheco, and et al. Large binocular telescope adaptive optics system: new achievements and perspectives in adaptive optics. *Society of Photo-Optical Instrumentation Engineers (SPIE)*, 2011. doi:10.1117/12.898641.

[18] S.S. Eikenberry, S.N. Raines, R.D. Stelter, A. Garner, and et al. Miradas for the gran telescopio canarias. *Society of Photo-Optical Instrumentation Engineers (SPIE)*, 2016. doi:10.1117/12.2232533.

[19] Gran Telescopio CANARIAS: Observatorio del Roque de los Muchachos La Palma, 2023. URL `https://www.gtc.iac.es/gtc/gtc.php`.

[20] M. Iye. Subaru telescope — history, active/adaptive optics, instruments, and scientific achievements. *Proc. Jpn. Acad., Ser. B 97*, 2021.

[21] A. Pastor, M. Sanjurjo-Rivo, and D. Escobar. Track-to-track association method-

ology for operational surveillance scenarios with radar observations. *CEAS Space Journal*, 15, 2023. doi:10.1007/s12567-022-00441-4.

[22] A. Pastor, M. Sanjurjo-Rivo, and D. Escobar. Initial orbit determination methods for track-to-track association. *Advances in Space Research*, 68, 2021. doi:10.1016/j.asr.2021.06.042.

[23] A. Pastor, M. Sanjurjo-Rivo, and D. Escobar. Track-to-track association methodology for operational surveillance scenarios with radar observations. *Celestial Mechanics and Dynamical Astronomy*, 2022. doi:10.1007/s12567-022-00441-4.

[24] A. Pastor, M. Sanjurjo-Rivo, and D. Escobar. Track-to-track association methodology for operational surveillance scenarios with radar observations. *Celestial Mechanics and Dynamical Astronomy*, 2022. doi:10.1007/s12567-022-00441-4.

[25] J.M. Maruskin, D.J. Scheeres, and K.T. Alfriend. Correlation of optical observations of objects in earth orbit. *Journal of Guidance, Control, and Dynamics*, 2009. doi:10.2514/1.36398.

[26] L. Pirovano, R. Armellin, J. Siminski, and T. Flohrer. Data association for too-short arc scenarios with initial and boundary value formulations. *Celestial Mechanics and Dynamical Astronomy*, 2019.

[27] W.R. Faber, W. Zaidi, and P.W. Schumacher. Early blast point determination for large geo fragmentation events. *AMOS Technologies Conference*, 2018.

[28] L. Dimare, S. Cicalò, A. Rossi, E.M. Alessi, and G.B. Valsecchi. In-orbit fragmentation characterization and parent bodies identification by means of orbital distances. *First International Orbital Debris Conference*, 2019.

[29] R.L. Roehrich F.R. Hoots, L.L. Crawford. An analytic method to determine future close approachhes between satellites. *Celestial Mechanics*, 33:143–158, 1984.

[30] A. Muciaccia, L. Facchini, M.F. Montaruli, and G. Purpura et al. Observation and analysis of Cosmos 1408 fragmentation. *73rd International Astronautical Congress (IAC)*, 2022.

[31] M.F. Montaruli, P. Di Lizia, E. Cordelli, H. Ma, and J. Siminski. A stochastic approach to detect fragmentation epoch from a single fragment orbit determination. *Adavances in Space Research*, 72:3713–3733, 2023. doi:10.1016/j.asr.2023.08.031.

[32] H.D. Curtis. *Orbital Mechanics for Engineering Students*. Elsevier, The Boulevard, Langford Lane, Kidlington, Oxford, OX5 1GB, UK, 3 edition, 2014. ISBN 978-0-08-097747-8.

[33] O. Montenbruck and G. Eberhard. *Satellite Orbits: Model, Methods and Applications*. Springer, 2000.

[34] T.G.R. Reid. *Orbital diversity for global navigation saltellite systems*. PhD thesis, Stanford University, 2017.

[35] A.M. Atallah, R.M. Woollands, T.A. Elgohary, and J.L. Junkins. Accuracy and efficiency comparison of six numerical integrators for propagating perturbed orbits. *The Journal of the Astronautical Sciences*, 2019. doi:10.1007/s40295-019-00167-2.

[36] D.A. Vallado, P. Crawford, R. Hujsak, and T.S. Kelso. Revisiting Spacetrack Report #3. *AIAA Astrodynamics Specialists Conference and Exhibit*, 2006. doi:10.2514/6.2006-6753.

[37] P.J. Cefola, Z. Folcik, R. Di-Costanzo, N. Bernard, S. Setty, and J.F. San Juan. Revisiting the DSST standalone orbit propagator. *Advances in the Astronautical Sciences* ·, 162, 2014. doi:10.1007/s40295-019-00167-2.

[38] M.F. Montaruli, L. Facchini, P. Di Lizia, M. Massari, G. Pupillo, G. Bianchi, and G. Naldi. Adaptive track estimation on a radar array system for space surveillance. *Acta Astronautica*, 198:111–123, 2022. doi:10.1016/j.actaastro.2022.05.051.

[39] D. Farnocchia, G. Tommei, A. Milani, and A. Rossi. Innovative methods of correlation and orbit determination for space debris. *Celestial Mechanics and Dynamical Astronomy*, 107, 2010. doi:10.1007/s10569-010-9274-6.

[40] J. Choi, J.H. Jo, and H.S. Him. Short-arc orbit determination results and space debris test observation of the owl-net. *Advanced Maui Optical and Space Surveillance Technologies Conference (AMOS)*, 2017.

[41] A. Milani, M. Sansaturio, and S. Chesley. The asteroid identification problem IV: Attributions. *Icarus*, 151, 2001. doi:10.1006/icar.2001.6594.

[42] L. Pirovano, D.A. Santeramo, R. Armellin, P. Di Lizia, and A. Wittig. Probabilistic data association: the orbit set. *Advanced Maui Optical and Space Surveillance Technologies Conference (AMOS)*, 132, 2020. doi:10.1007/s10569-020-9951-z.

[43] A. Milani, G.F. Gronchi, M. Dè Michieli, and Z. Knezevic. Orbit determination with very short arcs: I admissible regions. *Celestial Mechanics and Dynamical Astronomy*, 90:59–87, 2004.

[44] G. Tommei, A. Milani, and A. Rossi. Orbit determination of space debris: admissible regions. *Celestial Mechanics and Dynamical Astronomy*, 97:289–304, 2007. doi:10.1007/s10569-007-9065-x.

[45] B. Illowsky and S. Dean. *Introductory Statistics*. OpenStax, Rice University 6100 Main Street MS-375 Houston, Texas 77005, 2013. ISBN 978-1-947172-05-0.

[46] J. Frisbee. Empirical state error covariance matrix for batch estimation. *United Space Alliance, LLC*, 2011.

[47] L. Lebart, A. Morineau, and K.M. Warwick. *Multivariate Descriptive Statistical Analysis: Correspondence Analysis and Related Techniques for Large Matrices*. Wiley, University of California, 1984. ISBN 0471867438, 9780471867432.

[48] H. Ghorbani. Mahalanobis distance and its application for detecting multivariate outliers. *Mathematics and Information*, 34, 2019. doi:110.22190/FUMI1903583G.

[49] M. F. Zibran. *χ-Squared Test of Independence*. University of Calgary, Alberta, Canada, 2007.

[50] A.R. Jalalvanda, M. Roushanib, H.C. Goicoechea, D.N. Rutledged, and H.W. Gu. MATLAB in electrochemistry: A review. *Talanta*, 194:205–225, 2019. doi:10.1016/j.talanta.2018.10.041.

[51] NAIF JPL. The SPICE concept. URL `https://naif.jpl.nasa.gov/naif/spiceconcept.html`.

[52] N.L. Johnson, P.H. Krisko, J.C. Liou, and P.D. Anz-Meador. NASA's new breakup model of evolve 4.0. *Advances in Space Research*, 28:1377–1384, 2001.

[53] USSPACECOM. Space-track site, 2023. URL `https://www.space-track.org/`.

[54] C. Pardini and L. Anselmo. The short-term effects of the Cosmos 1408 fragmentation on neighboring inhabited space stations and large constellations. *Acta Astronautica*, 210:465–473, 2023. doi:10.1016/j.actaastro.2023.02.043.

[55] EUSST. Eusst confirms the fragmentation of space object COSMOS 1408, 2021. URL `https://www.eusst.eu/newsroom/eu-sst-confirms-fragmentation-cosmos-1408/`.

[56] EUTELSAT Group. EUTELSAT 7C, 2023. URL `https://www.eutelsat.com/en/satellites/eutelsat-7-east.html?#eutelsat-7c`.

[57] P. Di Lizia. Lec17 - typical measurements. Spacecraft Guidance and Navigation course, 2022.

[58] A. K. Nicholas. Attitude and Formation Control Design and System Simulation for a Three-Satellite CubeSat Mission. Master's thesis, University of Illinois at Urbana-Champaign, 2007.

[59] J.A. Siminski and T. Flohrer. Comparison-space selection to achieve efficient tracklet-to-object association. *Advances in Space Research*, 64:1423–1431, 2019. doi:10.1016/j.asr.2019.07.002.

Acknowledgements

Il percorso della mia tesi si conclude qui, in questa pagina, che vorrei dedicare a tutte le persone che mi hanno aiutato e supportato in questo viaggio al Politecnico, cominciato più di cinque anni fa. Non basterebbe un capitolo intero per riuscire a nominare tutti quelli che mi sono stati vicini e mi hanno fatto diventare lo studente, ma soprattutto la persona, che sono ora, ma cercherò di fare del mio meglio.

In primis, devo ringraziare enormemente il Prof. Montaruli e il Prof. Di Lizia per aver reso possibile tutto questo. Dal primo incontro nell'ufficio del professore fino all'ultimo meeting siete riusciti ad appoggiarmi con impegno e gentilezza. Quello che di più ho apprezzato, oltre al grande sostegno, è stata la vostra capacità di assicurarmi la serenità necessaria per intraprendere un percorso di ricerca complesso senza ansie o timori, permettendomi di estrarre il massimo da questa esperienza.

Un grande grazie lo devo dedicare alla mia famiglia: a mia mamma Tiziana, a mio papà Mario, a mio fratello Marco, ai nonni Gemma e Luigi, ad Antonio e a tutto il seguito. Grazie per essermi stati vicino: in questi anni mi avete visto crescere e con grande pazienza (ma davvero grande) siete riusciti a sopportarmi e a supportarmi fino alla fine.

Grazie a tutti i miei amici di Brescia, che hanno colorato la mia esperienza rasserenandomi con una risata anche nei momenti più difficili. Particolare menzione per gli amici di sempre Angelo, Tas, Gabriele, Alessio, Noemi, Federico, Tata, Franco e tutti gli Andrea. Senza di voi non sarebbe stato lo stesso, perchè siete la fonte della spensieratezza necessaria per arrivare in fondo.

Ringrazio anche tutti i compagni, prima ancora che colleghi, con cui ho potuto condividere questo intenso percorso a Milano. Siete stati il mio appoggio, riuscendo a farmi sentire a casa anche quando non lo ero. Insieme abbiamo condiviso un sacco di ricordi meravigliosi

che non andranno dimenticati, così come l'ospitalità e la gentilezza di tutte le volte in cui mi avete accolto sotto il vostro tetto.

Infine, un grazie a tutte le persone che non ho menzionato, ma che hanno contribuito anche in piccola parte a farmi stare bene in questi cinque anni. Non posso nominarvi tutti, ma posso dedicarvi l'impegno messo in questo lavoro.